UNIVERSITÄT PADERBORN
Die Universität der Informationsgesellschaft

Fakultät Naturwissenschaften

Department Physik

Inter- and Intraband Carrier Dynamics in Cubic $GaN/Al_xGa_{1-x}N$ Heterostructures Grown by MBE

Dem Department Physik
der Universität Paderborn
zur Erlangung des akademischen Grades eines
Doktor der Naturwissenschaften
vorgelegte

Dissertation

von

Tobias Wecker

Paderborn, 15.09.2017

Erster Gutachter: Prof. Dr. Donat J. As
Zweiter Gutachter: Prof. Dr. Cedrik Meier

„Gott, gib mir die Gelassenheit, Dinge hinzunehmen, die ich nicht ändern kann, den Mut, Dinge zu ändern, die ich ändern kann, und die Weisheit, das eine vom anderen zu unterscheiden.“

Gelassenheitsgebet von Reinhold Niebuhr (1941 oder 1942)

I Kurzfassung

In dieser Arbeit wurde die Ladungsträgerdynamik systematisch erforscht, indem asymmetrische Doppelquantentröge (ADQWs) und mehrfach Quantentröge (MQWs) aus kubischen GaN/$Al_xGa_{1-x}N$ hergestellt und experimentell ausgewertet wurden. Hierbei wurde besonderes Augenmerk auf den Einfluss der Kopplung von Einzel- und Mehrfach-QWs auf die optischen Eigenschaften gelegt. Die gewonnen Erkenntnisse können zu einem erweiterten experimentellen und theoretischen Verständnis für die Forschung an Intersubband Übergängen verwendet werden. Denn diese Übergänge ermöglichen die Erforschung nicht linearer Effekte, sowie die Herstellung von unipolaren Bauelementen im Bereich der 1,55 µm Emissionswellenlänge.

Zu Beginn wurden GaN/$Al_xGa_{1-x}N$ ADQWs mit unterschiedlicher Al Konzentration in den Barrieren auf ihr Kopplungsverhalten analysiert. Dies ergab eine Kopplung bei 7 nm dicken Barrieren für x = 0,26 und bei x = 0,64 startete die Kopplung bereits bei 3 nm. Daraufhin wurde extrapoliert, dass bei x = 1 die Kopplung bei 1-2 nm anfängt. Für diese Berechnungen wurden zeitabhängige Photolumineszenz Messungen (TRPL) verwendet, welche eine klare Korrelation zwischen Barrierendicke und Rekombinationszeit zeigten.

Des Weiteren wurden Si dotierte kubische AlN/GaN MQWs auf ihre IR Absorption untersucht. Die Halbwertsbreite (FWHM) dieser Spektren wurde theoretisch modelliert und es ergaben sich eine Korrelationslänge von $\Lambda = 0.53$ nm sowie eine durchschnittliche Höhe der Rauigkeit von $\Delta = 0.45$ nm. Zudem wurden erste nicht lineare Messungen mit einem Pump Probe Aufbau gemessen. Dies lieferte eine dritte Ordnung Suszeptibilität von $\mathrm{Im}\,\chi^{(3)} \sim 1.1 \cdot 10^{-20}\,\mathrm{m^2/V^2}$. Zudem wurden zusätzliche Intensitäten in den reziproken Raumkarten (RSM) von Messungen mittels hochauflösender Röntgenbeugung (HRXRD) in (002) und (113) Richtung gemessen, welche die Ausbildung eines Übergitters belegen. Die Verspannung der Schichten wurde ermittelt und in Berechnungen für die Übergangsenergien in nextnano³ verwendet. Ferner wurden ω-2θ Messungen mit MadMax modelliert, sie lieferten die realen Schichtdicken sowie Informationen über die Verspannung.

Die Parameter für kubische Nitride wurden schrittweise den experimentellen Daten angepasst und liefern in den theoretischen Überlegungen mittels nextnano³ und MadMax sehr gute Übereinstimmungen mit den experimentellen Messungen.

II Abstract

In this thesis a systematic investigation of the carrier dynamics between QWs is done exploiting asymmetric double quantum wells (ADQWs) and multi quantum wells (MQWs). The focus of interest was the coupling behaviour of single and multi QWs based on cubic GaN/$Al_xGa_{1-x}N$ and the influence on optical properties. This leads to the experimental and theoretical knowledge needed for the analysis of intersubband transitions important for the research of non-linear effects and unipolar devices emitting at a wavelength of 1.55 µm.

The first approach to the coupling was done with cubic GaN/ $Al_xGa_{1-x}N$ ADQWs with different Al content in the barriers. For the series with x = 0.26 the coupling starts at 7 nm barriers, for x = 0.64 the coupling begins at 3 nm barriers. For x = 1 the coupling is estimated to occur at 1-2 nm. In the calculation rate equations, time-resolved photoluminescence (TRPL) and conventional photoluminescence were used. The decay times of the TRPL data show a clear correlation with the barrier thickness. This indicates the tunnelling of carriers from the narrow QW to the wide QW.

Si doped cubic AlN/GaN MQWs have been used for intersubband absorption measurements. The FWHM of this absorption was theoretically fitted leading to a correlation length of $\Lambda = 0.53$ nm and a mean height $\Delta = 0.45\,\mathrm{nm}$ of the roughness. Also first experiments on MQWs concerning the non-linear behaviour have been performed with a pump probe setup revealing a third order susceptibility of $\mathrm{Im}\,\chi^{(3)} \sim 1.1 \cdot 10^{-20}\,\mathrm{m^2/V^2}$. The MQWs were investigated with HRXRD RSM around the (002) and (113) reflections, in order to prove the existence of SL peaks. Besides the strain in the heterostructures has been investigated by high resolution X-Ray diffractometry (HRXRD) reciprocal space maps (RSM) around (113) and are also validated by the theoretical calculations of the transition energies via nextnano³. Furthermore ω-2θ scans have been done and compared to theoretical considerations via MadMax. This revealed a good match with the expected layer thicknesses and the measured strain.

Thus one main point in this thesis is the systematic understanding of GaN/$Al_xGa_{1-x}N$ heterostructures and the validation of the theoretical models needed for energy transitions (nextnano³), layer thicknesses and strain (MadMax). To achieve this, a set of parameters was improved successively to match all the experimental results.

III Content

I Kurzfassung **3**

II Abstract **4**

III Content **5**

IV List of Abbreviations **7**

1 Motivation **8**

2 Theory **9**

2.1 Exciton Binding Energy 10
2.2 Heterostructures, Rate Equations and Selection Rules 12
2.3 MQWs, Waveguide and ISB Absorption 15
2.4 Band Edge of $Al_xGa_{1-x}N$ and Band Offsets 18

3 Experimental Setups **21**

3.1 Molecular Beam Epitaxy (MBE) 21
3.2 Reflection High Energy Electron Diffraction (RHEED) 22
3.3 UV Photoluminescence Spectroscopy Setup CW (PL) 23
3.4 Optical Setup TU Berlin 24
3.4.1 Photoluminescence Spectroscopy (PL) 24
3.4.2 Photoluminescence Excitation Spectroscopy (PLE) 25
3.4.3 Time-resolved Photoluminescence Spectroscopy (TRPL) 25
3.5 High Resolution X-Ray Diffractometry (HRXRD) 26
3.6 IR Absorption Setup TU Dormtund 29
3.7 Spatially-resolved Raman Spectroscopy 30
3.8 Picosecond Acoustics TU Dormtund 31
3.9 Intraband Non-linear Measurements TU Dortmund 32

4 Results and Discussion **33**

4.1 GaN Bulk: Raman and Defect Density 33
4.2 Thick QW: Strain Pulse 39
4.3 Asymmetric Double Quantum Wells (ADQW) 43
4.3.1 General Characterisation 43
4.3.2 Influence of Barrier Thickness to the Coupling 46
4.3.3 Time-resolved Investigation of Carrier Transfer 54
4.3.4 Excited Energy Levels 58
4.3.5 Summary ADQWs 64
4.4 Multi Quantum Wells (MQW) 65

4.4.1 Growth of MQW Samples 66
4.4.2 Investigation of MQWs by HRXRD 68
4.4.3 Calibration of QW Thickness by TEM 70
4.4.4 Photoluminescence Spectroscopy (PL) 72
4.4.5 Measurements of Intersubband Absorption 75
4.4.6 Intersubband Absorption Linewidth and Roughness 79
4.4.7 Non-linear Optical Measurements 85
4.4.8 Summary MQWs 87

5 Simulation 88

5.1 Nextnano³ 88
5.2 MadMax and ω-2θ Profiles 90

6 Summary 94

7 Appendix 96

7.1 Sample List 96
7.2 Literature 100
7.3 Abbildungsverzeichnis 104
7.4 List of Conferences 109
7.5 List of Publications 110
7.6 Parameters 111
7.7 Nextnano³ Source Code 112
7.8 Matlab Source Code 120
7.9 Acknowledgements 122
7.10 Eidesstattliche Erklärung 123

IV List of Abbreviations

ADQW	Asymmetric Double Quantum Well
c-$Al_xGa_{1-x}N$	cubic Aluminium Gallium Nitride
c-AlN	cubic Aluminium Nitride
CBO	Conduction Band Offset
c-GaN	cubic Gallium Nitride
HRXRD	High Resolution X-Ray Diffraction
MBE	Molecular Beam Epitaxy
PL	Photoluminescence
RHEED	Reflection High Energy Electron Diffraction
RSM	Reciprocal Space Map
VBO	Valence Band Offset
MBE	Molecular Beam Epitaxy
PAMBE	Plasma-assisted Molecular Beam Epitaxy
hh	Heavy hole
lh	Light hole
TRPL	Time-resolved Photoluminescence
MQW	Multi Quantum Well
QCL	Quantum Cascade Laser
ISB	Intersubband
nn³	Nextnano³
QW_W	Wide QW
QW_N	Narrow QW
X	Exciton
$X_{e\text{-}hh}$	Exciton (electron and heavy hole)
$X_{e\text{-}lh}$	Exciton (electron and light hole)
ML	Monolayer

1 Motivation

Intersubband transitions (ISBT) of multi quantum well (MQW) structures are in the focus of interest for designing several novel devices like quantum cascade lasers (QCL), IR detectors and more. Moreover, structures based on the material system of the group III-nitrides have numerous advantages, for instance high stability against mechanical, thermal, and chemical stress. Therefore structures containing these materials can be investigated using high excitation power, which is favourable for the optical study of nonlinear effects. Especially the ISBT in MQW structures can be exploited to get an insight into nonlinear effects, due to their high nonlinear response [1-5]. In addition, the inherently large band offset between GaN/AlN is beneficial for devices based on ISBT such as THz devices, fast modulators and fast photo detectors [6]. As a result, the ISBT in these devices can reach the 1.55 µm spectral window (optical C-band) [7], suitable for devices in the telecommunication industry. Consequently, a number of studies have elucidated the dynamical optical nonlinearity of such nitride-based heterostructures [3], [5]. So far, these experiments have focused on the common hexagonal phase. Recently, ISBT in the near infrared have been achieved in n-doped cubic GaN/AlN quantum wells (QWs) fabricated by plasma-assisted molecular beam epitaxy (PA-MBE) [8], [6] [9]. First studies of ultrafast carrier dynamics and nonlinear optical properties of these cubic heterostructures have been reported recently [10],[11].

Also $Al_xGa_{1-x}N$ as a compound material permits another degree of freedom and can be exploited for tailoring the bandgap in future heterostructures. Utilizing $Al_xGa_{1-x}N$ is especially suited for an efficient tuning of the required QW energy levels. A first approach to the topic of quantum cascade lasers is the investigation of asymmetric double quantum wells (ADQW), due to their different QW thicknesses the emission visible in luminescence can be adjusted separately. Thus coupling effects and the carrier transfer as well as the lifetimes of the charge carriers can be investigated in such ADQW structures using photoluminescence (PL) [12], photoluminescence excitation spectroscopy (PLE) [13] and time dependent photoluminescence (TRPL) [14] measurements. These measurements deliver the exact position of each energy level for electrons and holes within the QWs and their dynamic optical behaviour. Furthermore the tuning of the wavelength of the excitation source used in PLE gives direct access to the related absorption but also to charge carrier transfer processes by monitoring the luminescence signal. Therefore, not only the charge carri-

er transfer from e.g. the barrier material into the QWs can be observed but even inter QW coupling processes (or their suppression) can experimentally be witnessed [15].

Common hexagonal group III-nitrides suffer from large internal polarisation fields along the c-axis resulting in a bending of the bands and the quantum confined Stark-effect. Due to both effects the design of modern devices for ISBT in the hexagonal phase is fairly complicated [16]. In order to reduce these effects the growth of hexagonal nitrides in semi-polar directions is intensively investigated [17]. Another approach is the growth of group III nitrides in the cubic phase in the (001) direction on 3C-SiC. Therefore, all above listed unfavourable effects can be significantly reduced [18][19].

2 Theory

In this chapter some of the fundamentals about low dimensional semiconductors are described. The exciton binding energy in quantum wells (QWs) significantly differs from a thick semiconductor layer. This is important for the comparison of the simulations of the band structure (nextnano³) and the energy transitions with the experimental optical results delivered by photoluminescence and photoluminescence excitation spectroscopy. Thus this has to be considered for the optical behaviour in heterostructures for example by comparing the rate equations and selection rules with the experimental data. The third subchapter covers MQWs and their optical properties like IR absorption. For this absorption the light has to approach perpendicular to the QW growth direction, in order to satisfy the selection rules. The last subchapter deals with the theoretical band edges of $Al_xGa_{1-x}N$ for various Al content. This is crucial for the determination of the band offsets between the valence and the conduction band at the $GaN/Al_xGa_{1-x}N$ hetero interface for single and multi QWs.

2.1 Exciton Binding Energy

An exciton is an electron hole pair connected by the Coulomb force. This quasi particle can be described as a single particle with hydrogen like line spectrum. Due to the Coulomb force the energy of the exciton is lowered by the exciton binding energy. This energy can be expressed very similar to the hydrogen model [20].

$$E_{3D} = \frac{\mu^* e^4}{2\,(4\pi\epsilon)^2\hbar^2}\frac{1}{n^2} = \frac{R_x}{n^2} \tag{2.1}$$

With the effective mass $\frac{1}{\mu^*} = \frac{1}{m_e^*} + \frac{1}{m_h^*}$ determined by the effective electron mass m_e^* and the effective hole mass m_h^*. This description is only valid for thick bulk material. For quantum mechanical systems like quantum dots, quantum wires and quantum wells the deviation to this formula increases for smaller dimensions. Thus in this thesis the model presented in [21] is used to calculate the exciton binding energy in the QWs. The following formula can be applied for QWs with $\frac{L_W}{2} < a_{ex}$, where L_W is the thickness of the QW and a_{ex} the Bohr radius of the exciton.

$$E_{ex} = \frac{4}{(\alpha-1)^2}E_{3D} \tag{2.2}$$

The dimension in space α has to be an integer value between 2 and 3. This term is given by:

$$\alpha = 3 - e^{-(2/k_b + L_w)/\,2\,a_{ex}} \tag{2.3}$$

The exciton binding energy for thick c-GaN layers is $E_{3D} = 24\,\mathrm{meV}$ [22] and k_b corresponds to the wave vector in the barriers.

$$k_b = \frac{\sqrt{2m_b(V-E)}}{\hbar} \tag{2.4}$$

Adapting the relating mass m_b and the potentials V and E the parameter k_b for electrons k_{be}, light holes k_{blh} and heavy holes k_{bhh} can be calculated. The value k_{bh} is determined using the light holes (lh) or heavy holes (hh).

$$\frac{1}{k_b} = \frac{1}{k_{be}} + \frac{1}{k_{bh}} \tag{2.5}$$

The Bohr radius in a semiconductor is influenced by the Bohr radius of the hydrogen atom $a_H = 0{,}529 \cdot 10^{-10}\,\mathrm{m}$ and the dielectric constant in the semiconductor ε_s.

$$a_{ex} = \frac{\varepsilon_s}{\mu^*}a_H \tag{2.6}$$

The effective mass $\frac{1}{\mu^*} = \frac{1}{m_e^*} + \frac{1}{m_h^*}$ depends on the penetration length into the barrier, described by the parameter β.

$$\beta = \frac{L_W}{\frac{2}{k_b}+L_W} \tag{2.7}$$

$$m^* = \beta m_w + (1-\beta) m_b \tag{2.8}$$

These theoretical considerations lead to the following formula for the exciton binding energy E_{ex} in a QW:

$$E_{ex} = \frac{E_{3D}}{\left(1-\frac{1}{2}\exp\left(-\frac{\frac{2}{k_b}+L_W}{2a_{ex}}\right)\right)^2} \tag{2.9}$$

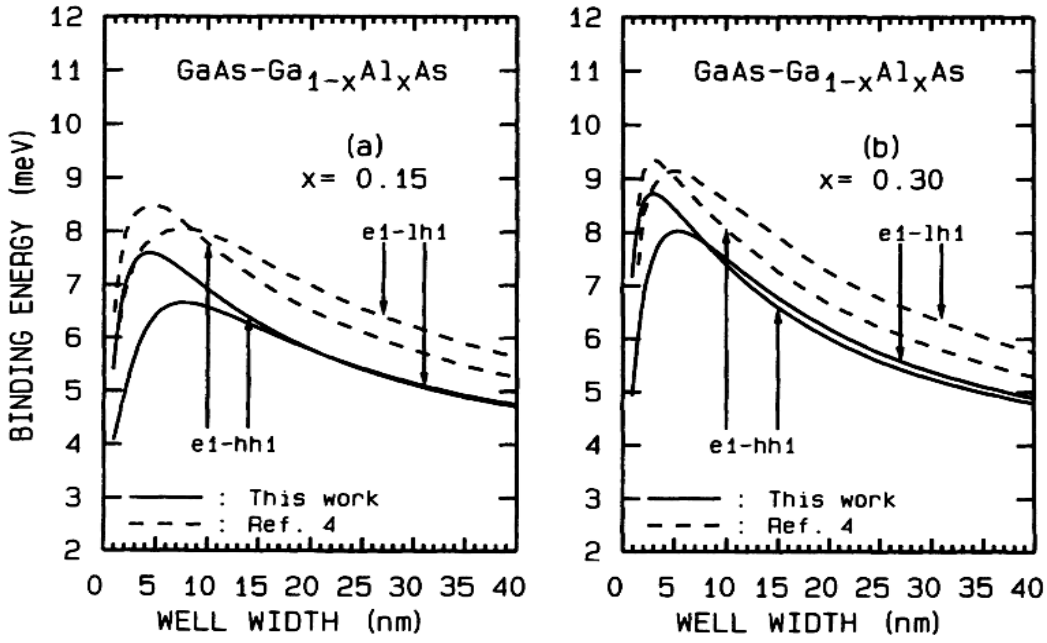

Figure 2.1 Excitonic binding energies for excitons consisting of e-hh and e-lh. The dotted lines correspond to complex simulations and the straight lines are calculated by the fractal dimensional method. In the left side the Al content in the barriers is 15% and on the right 30% [21].

The calculated results of a $Ga_{1-x}Al_xAs$/GaAs QW are shown in Figure 2.1 against the well width. Considering a very thick QW the binding energy approaches the value for the bulk layer of the QW material (GaAs). For real structures with finite barrier heights the binding energy increases to a factor of 1.4-1.6, although the theory for infinite barrier heights predicts a factor of 4. For very thin QWs the exciton radius is much larger than the QW width, leading to a strong penetration into the barriers. This results in a lowering of the exciton binding energy towards the bulk value of the barrier material ($Ga_{1-x}Al_xAs$).

2.2 Heterostructures, Rate Equations and Selection Rules

Optical investigations on a single QW structure reveal an insight into the energy levels of the electrons and holes. Due to selection rules the amount of possible transitions is limited. In case of the excitation light entering the structure parallel to the QW growth direction, only the interband transitions with electrons and holes take part. The dipole matrix element describes all transitions enabling the calculation and identification of allowed transitions and forbidden transitions [23].

$$\left\langle \phi_j^e(z) \middle| \vec{e} \cdot \hat{p} \middle| \phi_i^h(z) \right\rangle \tag{2.10}$$

With the two wave functions $\phi_j^e(z)$ and $\phi_j^h(z)$. These wave functions are oriented along the z direction, which is equal to the growth direction of the QWs. Furthermore $\phi_j^e(z)$ describes an electron wave function and $\phi_j^h(z)$ a hole wave function. Besides the dipole matrix element depends on the polarisation $\vec{e}$ and the momentum operator $\hat{p} = -i\hbar\Delta$. The polarisation $\vec{e}$ contains the geometry information of the incident beam in regard to the QW growth direction and strongly influences the absorption. This leads for our case to the selection rules $\Delta n_{inter} = 0,2,4,6, \ldots$, with the difference of the quantum number of the two participating energy levels Δn. Some of the allowed transitions visible in optical spectra are shown in Figure 2.2. Only the transitions between the first electron level (e1) and the first heavy hole level (hh1) $E_{e1} - E_{h1}$ and the second e and hh level $E_{e2} - E_{h2}$ can be investigated optically. There is a non-zero probability to measure a forbidden transition in real structures, but the allowed transitions are several orders of magnitude stronger. In real structures interface roughness, defects and fluctuation of Al in the $Al_xGa_{1-x}N$ layers lead to a deviation from the above described transition rules. Due to these effects the symmetry of the wave function can differ from that in the ideal case, changing the value of the dipole matrix element.

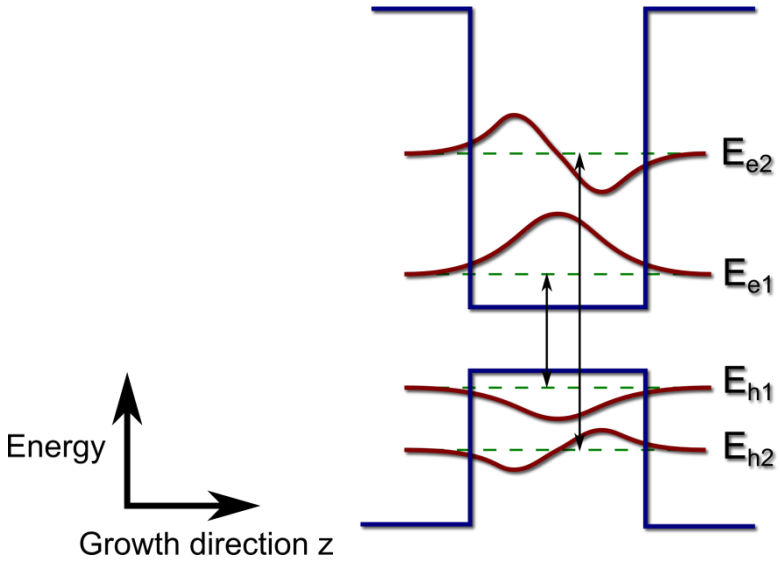

Figure 2.2 For real QWs the wave functions of the carriers penetrate into the barrier. Furthermore the allowed transitions follow the selection rule Δn_{inter} = 0,2,4,6.....

Due to the finite barrier height in real heterostructures, the wave function penetrates into the barrier material. This leads to a non-zero probability to find the carriers in this barrier. This phenomenon is described by the penetration depth λ. For barriers thinner than the penetration depth λ tunnelling through the barrier occurs. The probability for transmission T(d) depends on the barrier thickness d and the barrier height V. In Figure 2.3 a schematic conduction band of an ADQW is shown. Such heterostructures consists of a wide QW (QW_W) and a narrow QW (QW_N). For the calculation the effective barrier height V-E is used, with the energy level of the carriers E [24].

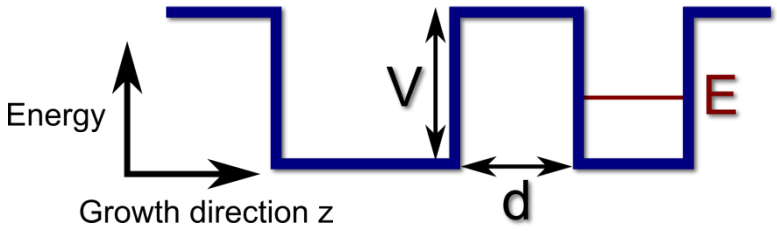

Figure 2.3 Scheme of the conduction band of an ADQW. The important parameters for tunnelling are the barrier height V and the barrier thickness d.

$$T(d) = \frac{T_0 4kE(V-E)}{4kE(V-E)+\left((k-1)E+V^2\right)\sinh^2\left(\frac{d}{\lambda}\right)} \tag{2.11}$$

Where $T_0 = \frac{h}{4m_{well}L_z^2}$ is the classical period of the electron or hole motion in a well of thickness L_z, $k = \frac{m_{barrier}}{m_{well}}$ is the effective mass ratio of the carriers and $\lambda = \frac{\hbar}{\sqrt{2m_{barrier}(V-E)}}$ is the penetration depth of the wave functions into the barriers. The energy levels of the carriers E are provided by nextnano³ simulations.

The non-resonant tunnelling rates for electrons and light holes should be much higher than for heavy holes, due to the lower effective mass. Nevertheless also the barrier potential height V inflicts the non-resonant tunnelling rate, counteracting this effect. The barriers in the valence bands are much lower, leading to higher tunnelling rates. A general estimation of the non-resonant tunnelling rates of electrons and holes provides values of the same order of magnitude for both carriers. Thus Photo induced Space-Charge Build-up effects weren't considered in contrast to other material systems on similar structures like InGaAs/InP QWs [25].

In case of optical investigation of an ADQW we use a simple model to describe the experimental results. Light of the excitation source is absorbed creating electron hole pairs in the two QWs and in the surrounding barrier material. The charge carriers in the barriers diffuse into the wide QW and narrow QW. These processes are considered by generation rates G_W and G_N. But a part of the generated carriers in the narrow well is able to tunnel through the thin barrier into the wide well with the non-resonant tunnelling rate T(d). The remaining carriers recombine radiative with lifetime τ_N. This leads to the following rate equation of carrier densities in the narrow n_N and the wide n_W well [24].

$$\frac{dn_N}{dt} = G_N - \frac{n_N}{\tau_N} - T(d)n_N \tag{2.12}$$

$$\frac{dn_W}{dt} = G_W - \frac{n_W}{\tau_W} + T(d)n_W \tag{2.13}$$

And for holes accordingly. Using the steady state solutions of the above equations, the ratio of the intensities I_N to I_W is given by:

$$\frac{I_N}{I_W} = \frac{\frac{\tau_W}{\tau_N}}{\left(1+\frac{G_W}{G_N}\right)\tau_W\, T(d)+\frac{G_W\,\tau_W}{G_N\,\tau_N}} \tag{2.14}$$

Where τ_W and τ_N are the radiative life times in the two QWs.

2.3 MQWs, Waveguide and ISB Absorption

The possibility to grow complex structures like multi quantum wells (MQWs) enables several areas of investigation. For example for the group III nitrides the IR spectral region can be covered in a wide range around the important telecom wavelength 1.55 µm. Devices consisting MQW structures in this field are quantum cascade lasers (QCL), IR detectors and more.

To investigate these structures in the IR optically, intraband transitions are exploited. For these transitions only one charge carrier type take part in the transition. Here mostly electrons are used, due to their lower effective mass the devices can operate much faster than with holes. For the intraband transition the transition matrix element in equation 2.10 is still valid, but both wave functions in the formula are electron wave functions. For light arriving parallel to the QW growth direction $\vec{e}$ can be written as $\vec{e}_x = (1,0,0)$ (also called TE polarisation) or $\vec{e}_y = (0,1,0)$. Both directions are equal for optical measurements of QWs. Calculating these two geometries lead to $\vec{e}_x \cdot \hat{p} = -i\hbar\frac{\partial}{\partial x}$ and $\vec{e}_y \cdot \hat{p} = -i\hbar\frac{\partial}{\partial y}$. In this case the dipole matrix element in formula (2.10) is zero and no absorption is possible. Thus the intraband transitions can only be excited for light arriving perpendicular to the growth direction of the MQWs. For intraband transitions $\vec{e}_z = (0,0,1)$ (also called TM polarisation) holds true leading to $\vec{e}_z \cdot \hat{p} = -i\hbar\frac{\partial}{\partial z}$ [26]. For this case absorption is possible, because of the z orientation of the wave functions. This leads to a change in the selection rules. The momentum operator $\hat{p} = -i\hbar\Delta$ changes the parity of the wave function $\phi_i(z)$. So the selection rules change to $\Delta n_{intra} = 1,3,5,7,\ldots$.

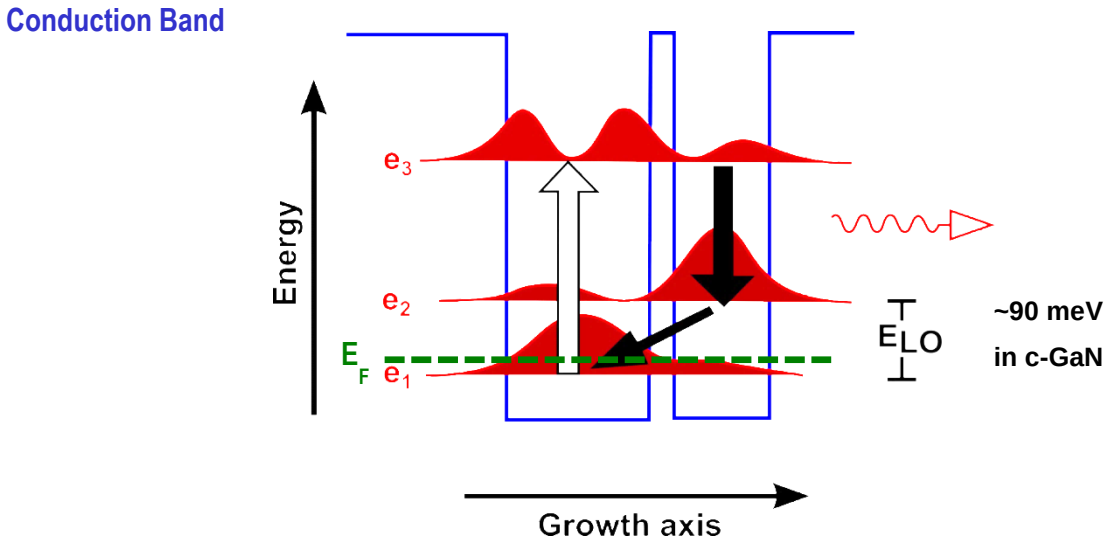

Figure 2.4 Band diagram of an ADQW with a thin barrier. The Fermi energy E_F is slightly above the first electron level caused by doping.

In Figure 2.4 the conduction band of an asymmetric double QW is shown. The barrier is thin enough, to allow for tunnelling. There are three electron levels in this diagram. The e1 and e3 levels originate from the wider QW and the e2 is caused by the narrow QW. The probability distribution $|\Psi|^2$ is plotted in red, to indicate the probability to find an electron in the different QWs. Due to the thin barrier there is a non-zero probability to find electrons for each energy level in both QWs. The changed selection rules for intraband transitions, as described before, enable the transition between e1 and e3 in the wide QW. Furthermore the symmetry is different compared to the previously discussed simple QW, leading to less strict selection rules.

The basic principle of a quantum cascade laser can be explained using Figure 2.4 [27] [28]. Because of high doping the Fermi energy E_F is slightly higher than the first electron level e1, in order to get a high population of e1. The electrons of e1 are excited via absorption to e3 and they tunnel through the thin barrier into the narrow QW. Then they fall down from e3 to e2 by emitting IR photons. The last step is phonon assisted tunnelling through the barrier into e1 of the wide QW. For this step the energy separation of e1 and e2 should be in the range of the energy of an LO-Phonon (in c-GaN 92 meV [29][30]). Lasing can occur in the narrow QW between e3 and e2, because the carrier injection into e3 is done efficiently by the tunnelling process and e2 is also emptied by the phonon assisted tunnelling.

The substrates used for this thesis consist of 500 µm Si (001) with 10 µm 3C-SiC (001) on top. This is followed by the PA-MBE grown c-GaN buffer layer with 100 nm and the MQW structure with around 100 nm. Thus the MQW layers important for our investigation are only 100 nm thick. This is very significant for the absorption measurements, because of the selection rules the incident light has to approach perpendicular to the MQW growth direction. Therefore most of the light enters the Si and 3C-SiC and doesn't take part to our experiment. In order to improve this, a waveguide structure is processed with 30° side facets (Figure 2.5). For this angle total reflection at the top and bottom of the sample piece is achieved. In our case the waveguide samples are 5-8 mm long leading to 10-20 passes through the MQW layers. Unfortunately the waveguide structure changes the angle of the light travel-ing through the MQWs as well, decreasing the coupling of the light and the MQW. The best coupling is achieved for a perpendicular angle of incidence in regard to the growth direction of the MQWs (selection rules). These two processes have to be optimised, to get a good absorption signal. For the waveguide with 30° facets discussed here, the coupling is high enough to measure IR absorption.

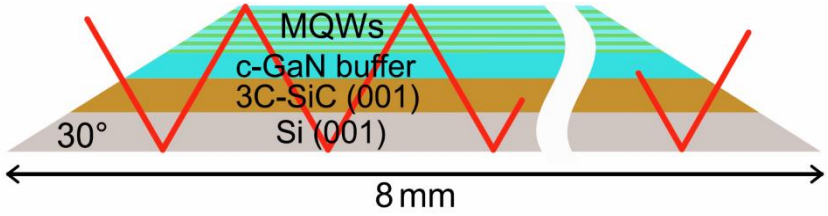

Figure 2.5 Sketch of a waveguide used for absorption measurements. Multiple passes through the MQWs are achieved by total reflection. The layer thicknesses are not to scale.

2.4 Band Edge of $Al_xGa_{1-x}N$ and Band Offsets

For the simulation of the band structure with the semi empirical program nextnano[3] the knowledge of the conduction band and valence band offsets for the $GaN/Al_xGa_{1-x}N$ interface is needed. So an ab-initio calculation was done by Marc Landmann of AG Schmidt in University of Paderborn. The ab-initio determination of (strained) band offsets commonly involves a two-step procedure relying on separate heterostructure and bulk calculation. The super-cell approach is utilized to model the semiconductor interfaces on the microscopic level. In the super-cell approach the semiconductor heterostructure is represented as an infinite superlattice with fixed in-plane lattice parameter. Choosing the substrates' in-plane lattice constant and allowing unit-cell relaxation along the growth direction enables the accurate estimation of band offsets in pseudomorphically strained heterostructures. Using the medial in-plane lattice parameter of the interfacing materials enables an estimation of the natural unstrained band discontinuities.

The change in the macroscopic three-dimensional average of the local electrostatic potential across the interface has been used as an energy reference to align the band energies of the interfacing materials, which are obtained from two separate bulk calculations. In case of strained band-offsets the bulk semiconductors are considered to be bi-axially strained under the constraint of volume conservation. For estimation of natural band offsets the bulk semiconductors are considered at equilibrium lattice constant.

The electronic structure calculations are performed within the framework of plane-wave density functional theory (DFT) as implemented in the Vienna Ab-initio Simulation Package (VASP) code. The DFT inherent under estimation of electronic band gaps, originating from the use of common (semi)local exchange-correlation (XC) functionals, is corrected by using nonlocal, screened Coulomb potential Heyd-Scuseria-Ernzerhof (HSE) type hybrid density functionals with material dependent exact exchange (EXX) fractions. The EXX fractions have been adjusted to mimic electronic structure characteristics obtained via higher level theories as the GW approximation to many-body perturbation theory. Since the relative change in the average of the electrostatic potential across the heterostructure-super cell is barely affected by the use of conventional (semi)local XC functionals and the use of hybrid functionals is computationally expensive, the hybrid functional treatment is restricted to the bulk calculations. For further details on the ab-initio determination of natu-

ral and strained band offsets, including details of the heterostructure unit-cell setup as well as numerical details of the electronic structure calculations, the reader is referred to the references [9],[31]. In Figure 2.6 the general behaviour of the band offsets for $Al_xGa_{1-x}N$ /GaN heterostructures partially strained on a c-GaN buffer layer is shown for different Al content.

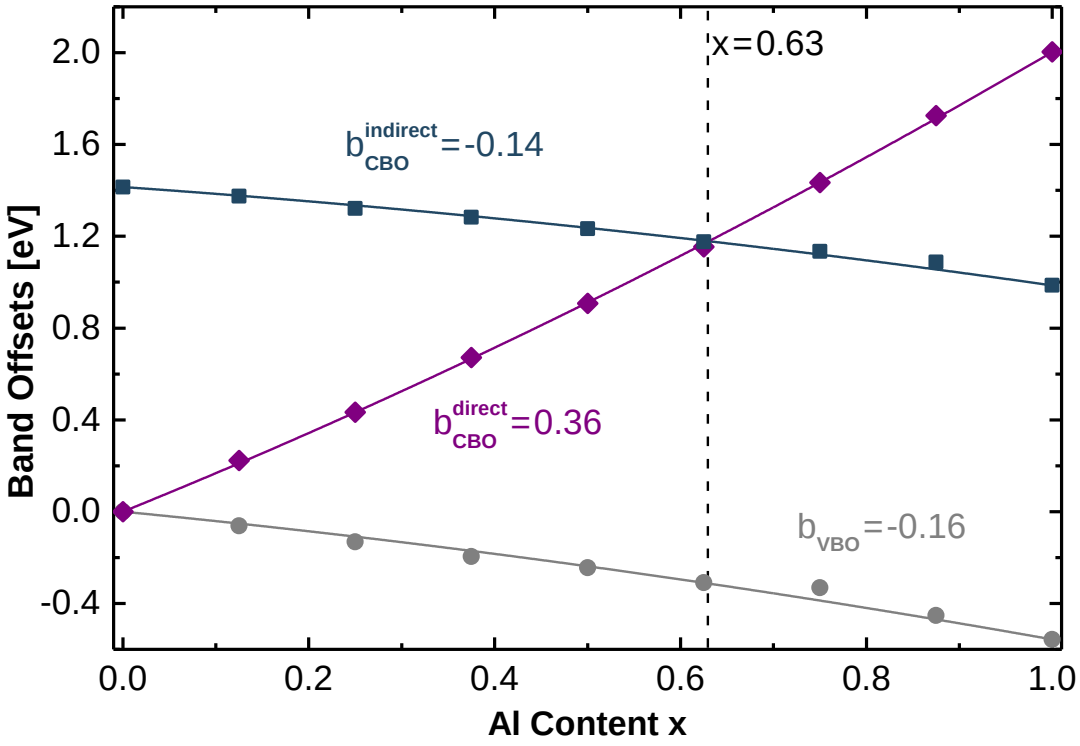

Figure 2.6 Trend of the band offsets for a GaN/$Al_xGa_{1-x}N$ interface partially strained on a c-GaN buffer layer for various Al concentrations in the $Al_xGa_{1-x}N$ barrier layers. (Provided by Marc Landman in University of Paderborn)

In case of the direct $\Gamma_V - \Gamma_C$ conduction band edge CBO^{dir} and the valence band VBO the formulas are:

$$CBO^{dir} = 2.0032x - 0.3637x(1-x) \quad (2.15)$$

$$VBO = -0.5569x + 0.1640x(1-x) \quad (2.16)$$

The indirect $\Gamma_V - X_C$ conduction band edge CBO^{ind} for different Al content x is described by:

$$CBO^{ind} = 0.9860x + 1.4147(1-x) + 0.1339x(1-x) \quad (2.17)$$

The change of $Al_xGa_{1-x}N$ from a direct to an indirect semiconductor starts at x = 0.63. Besides the exact influence of strain on the CBO:VBO values and the correct application into nextnano³ is still under investigation. The direct bandgap

CBO:VBO used in this thesis are 80:20, 79:21 and 78:22 for x = 0.26, x = 0.64 and x = 1, respectively.

Another important parameter is the bandgap for different Al content x, as can be seen in Figure 2.7. Similar to Figure 2.6 there is a change from the direct bandgap ($\Gamma_V - \Gamma_C$) to the indirect bandgap ($\Gamma_V - X_C$) visible at an Al content of around 0.71. The difference in the Al content at which the change occurs is caused by the applied strain, for fully and partly strained layers the value is slightly different. This is still under investigation. The calculated data are represented as dots and squares with a quadratic fit. These fit curves provide the bowing parameter for the direct bandgap $b_{Bowing}^{direct} = 0.85$ and the indirect bandgap $b_{Bowing}^{indirect} = 0.01$ [77].

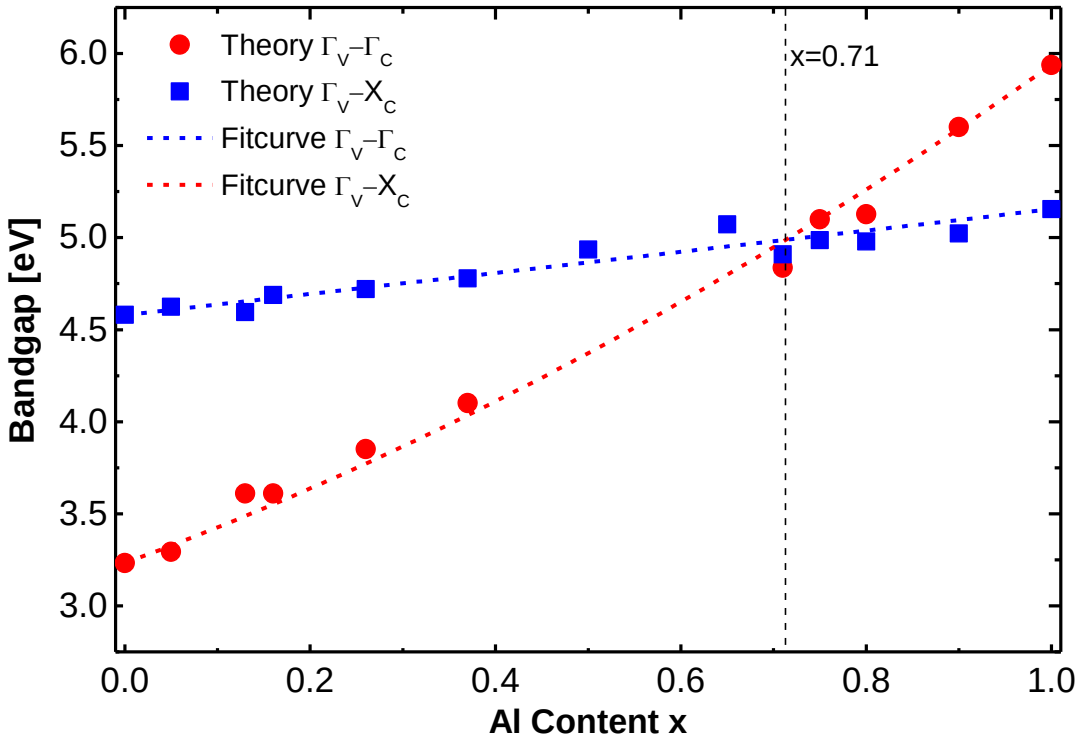

Figure 2.7 Bandgap of relaxed cubic $Al_xGa_{1-x}N$ for different Al content. There is a change from direct $\Gamma_V - \Gamma_C$ (red) to indirect bandgap $\Gamma_V - X_C$ (blue) at $x = 0.71$ [77].

3 Experimental Setups

3.1 Molecular Beam Epitaxy (MBE)

The growth system used in this thesis consists of a Riber 32 plasma assisted Molecular Beam Epitaxy (PA-MBE). The atomic nitrogen is provided by an Oxford plasma cell splitting the N_2 exploiting radio frequency waves. Conventional effusion cells are used for Al, Ga and Si evaporation (see Figure 3.1). All cells are calibrated with a Bayard-Alpert gauge before the start if a growth series, connecting the temperatures of the cells to the flux at the position of the sample. For growth monitoring and adjustment RHEED was used as in-situ measurement.

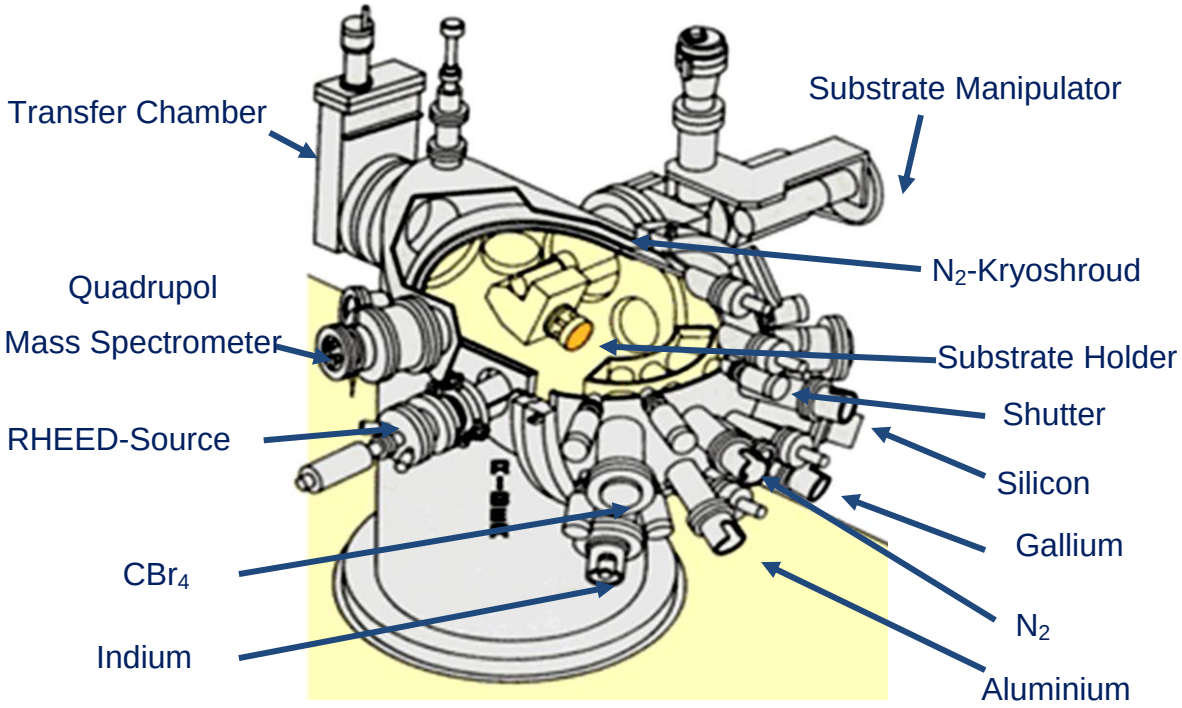

Figure 3.1 Schematic picture of the used Riber 32 PA-MBE [32]

All effusion cells are cooled with water and have a shutter to control the evaporation time with a computer. There is additional liquid nitrogen cooling (LN_2) at the chamber walls, so the residual atoms will stick to the walls improving the vacuum further. Two turbo pumps supply the ultra-high vacuum in the range up to $5 \cdot 10^{-9}$ mbar.

3.2 Reflection High Energy Electron Diffraction (RHEED)

Reflection High Energy Electron Diffraction (RHEED) can be used to monitor the growth parameters during growth. An electron gun accelerates the electrons with $V = 16\,kV$ and $I = 1.6\,A$ towards the sample. Due to the small angle of incidence the electrons only penetrate few monolayers into the sample. The electrons are diffracted at the sample surface and measured at a fluorescence screen. This screen is surveyed by a digital camera connected to a computer. The basic principle and the geometries of the RHEED measurements can be seen in Figure 3.2. A part of the electron beam is transmitted (dotted red line) and visible as a single point (red) on the screen. Another part of the beam is reflected (orange).

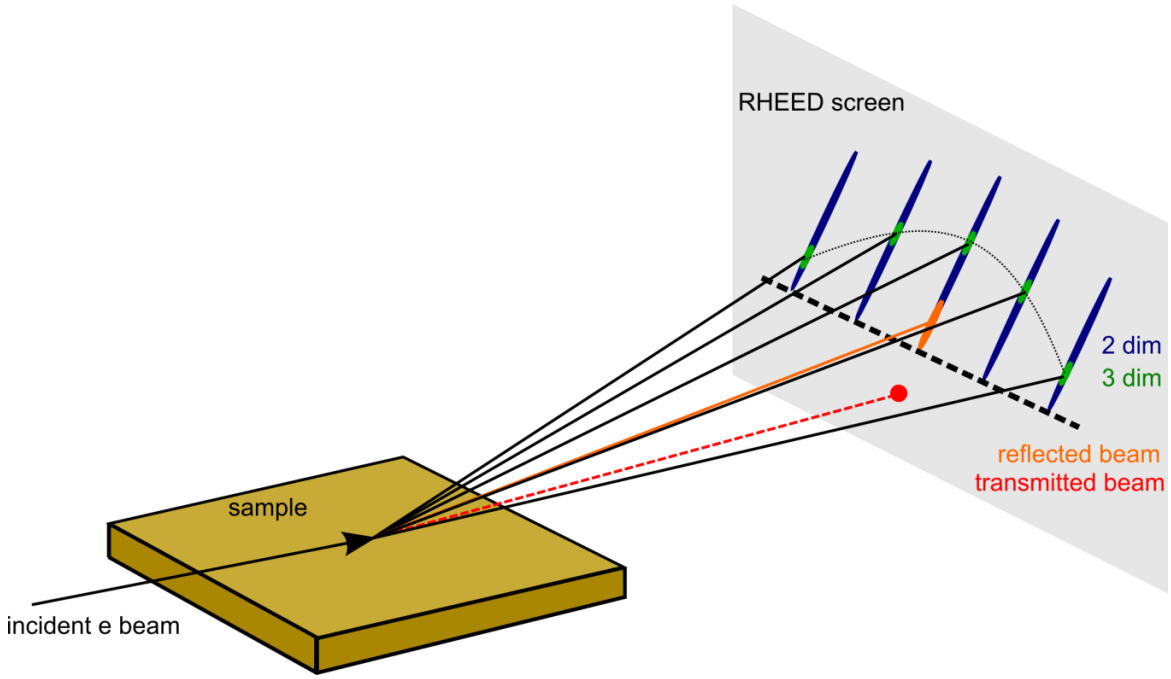

Figure 3.2 Representation of the basic principle of the RHEED measurement. Also the geometries of the different beams in regard to the sample can be seen.

2 dimensional (flat) surfaces appear as lines on the RHEED pattern. On the other hand 3 dimensional (rough) surfaces cause spots. In realistic RHEED patterns both components are visible. In Figure 3.2 a simplified RHEED pattern is shown with 2 dim lines (blue) and 3 dim spots (green).

3.3 UV Photoluminescence Spectroscopy Setup CW (PL)

The photoluminescence setup contains a Nd:YAG Laser, a closed cycle cryostat and a Spex270M monochromator suitable for optical investigation in the UV spectral range. A sketch of the setup is shown in Figure 3.3. The Nd:YAG CW laser with two frequency doubling steps emits at 266 nm. Furthermore a HeCd CW Laser of Kimmon emitting at 325 nm can be used by switching a movable mirror (Figure 3.3 in red). In this thesis only the Nd:YAG laser was used at a power of 5 mW. For low temperature and temperature dependent PL measurements the sample is positioned in a cryostat, connected to a closed cycle cooler reaching 13 K. The detection is done by a Spex270M monochromator with an Hamamatsu type 943-02 GaAs photomultiplier or an Andor CCD (iDus 420). There are two monochromator grids with a blaze wavelength of $500\,\mathrm{nm}$ and $1200\,\mathrm{g/mm}$ available. In order to eliminate the laser lines in the PL spectra there is an edge filter for each laser available, positioned in front of the monochromator. The beam diameter for the two lasers are in the order of $\mathrm{d_{HeCd}} = (150 \pm 30)\,\mu\mathrm{m}$ and $\mathrm{d_{Nd:YAG}} = (140 \pm 10)\,\mu\mathrm{m}$.

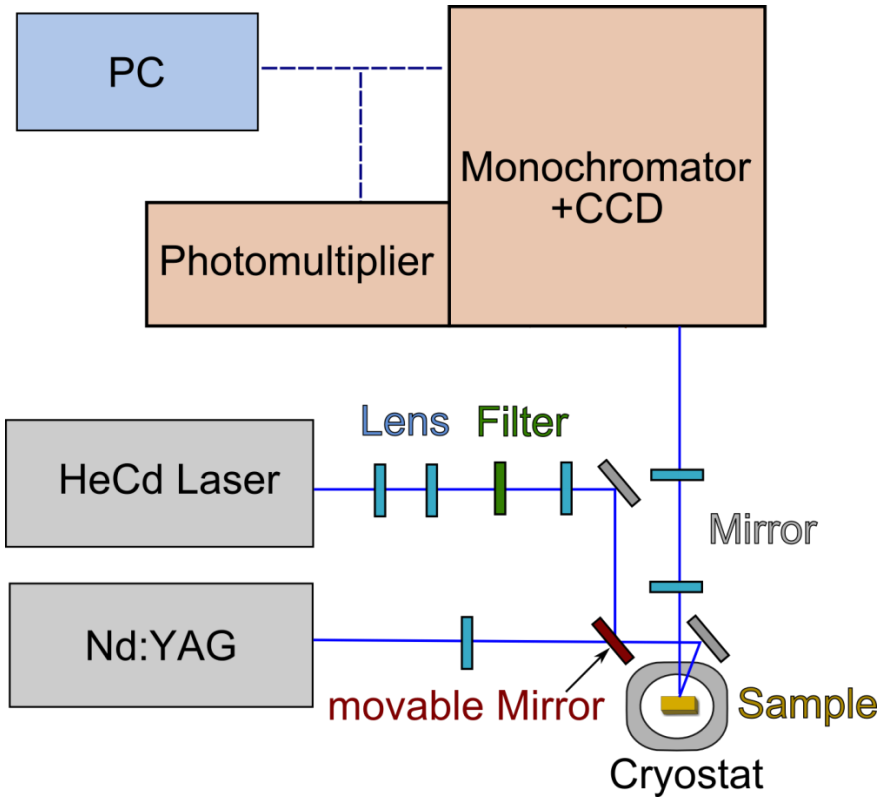

Figure 3.3 Sketch of the UV PL setup. The excitation light is focused on the sample placed in a cryostat reaching 13 K. The detection is done by a monochromator with photomultiplier and CCD attached.

3.4 Optical Setup TU Berlin

The optical setup used in the workgroup of Axel Hoffman at Institute of Solid State Physics in TU Berlin enables photoluminescence, photoluminescence excitation and time-resolved photoluminescence measurements. The complex setup is depicted in Figure 3.4. Generally, the samples were placed in a He-flow cryostat (Janis ST-500) at a temperature of 7 K. The details are explained in the following subchapters.

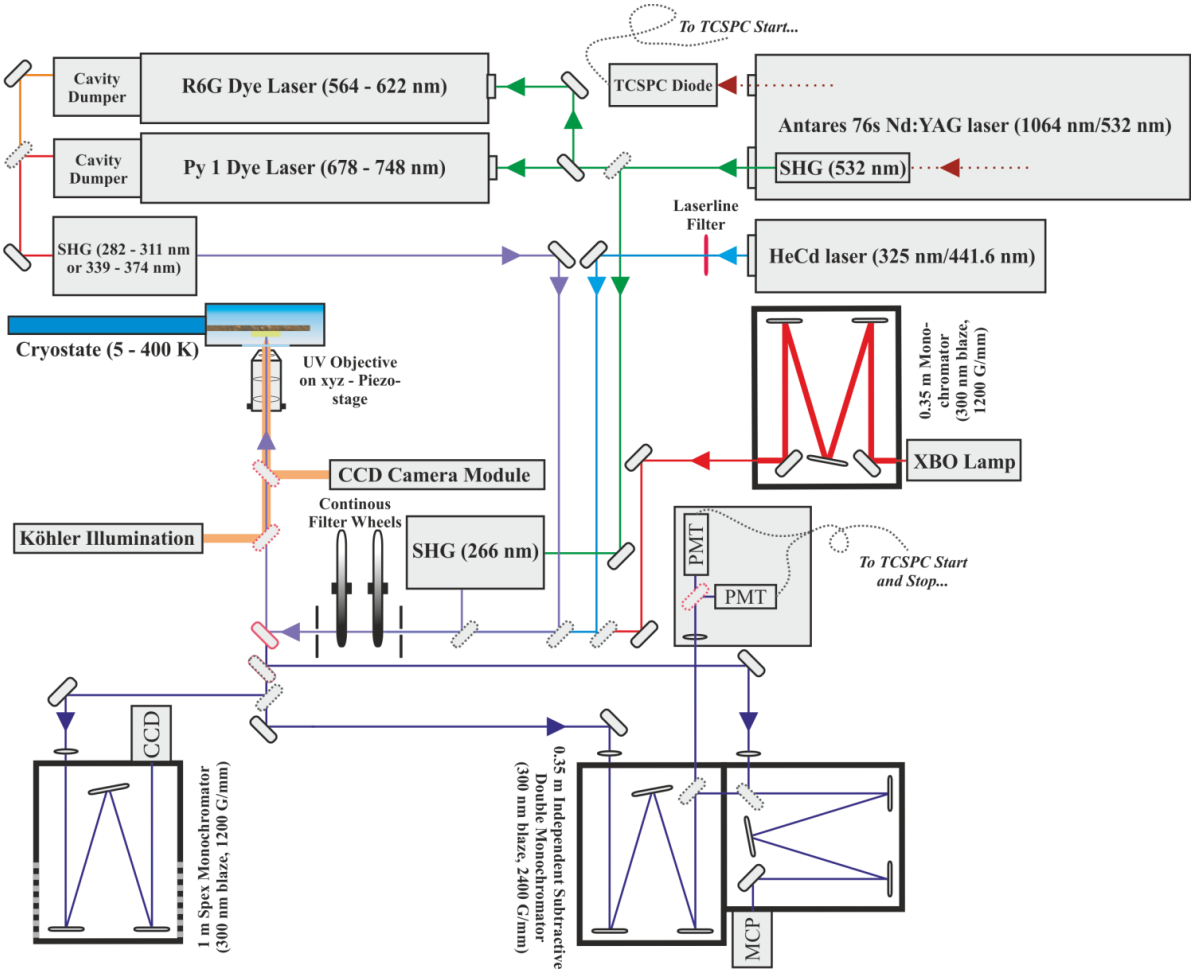

Figure 3.4 Illustration of the complex optical setup. With this setup PL, PLE and TRPL measurements can be done. (AG Hoffmann TU Berlin)

3.4.1 Photoluminescence Spectroscopy (PL)

Photoluminescence (PL) measurements were conducted time integrated with a frequency-quadrupled, picosecond Nd:YAG laser (266 nm, 76 MHz repetition rate). For recording the PL spectra, the luminescence signal was dispersed by a single monochromator (Spex 1702, 1 m focal length, 1200 g/mm, 300 nm blaze) and detected by a CCD.

3.4.2 Photoluminescence Excitation Spectroscopy (PLE)

The photoluminescence excitation (PLE) measurements were done using a 500 W Xenon short-arc lamp (XBO) for the optical excitation of the samples. In addition, for the PLE experiments the XBO lamp was guided through an additive double mono-chromator (SpectraPro) yielding a spectral resolution of about 3.2 nm.

3.4.3 Time-resolved Photoluminescence Spectroscopy (TRPL)

For the time-resolved photoluminescence (TRPL) measurements, the luminescence signal was analysed with a subtractive double monochromator (McPherson 2035 - 0.35 m focal length, 2400 g/mm, and 300 nm blaze) and a single photon-detection can be achieved with a multichannel-plate (MCP) photomultiplier tube (Hamamatsu R3809U-52). Here, the overall time-resolution of the setup is limited by the laser pulse width of ≈ 55 ps. Standard photon counting electronics were applied in order to derive the final histograms. Finally, a common, convoluted fitting approach was applied to the data, to extract all decay times unaffected by the particular temporal response function of the entire setup.

3.5 High Resolution X-Ray Diffractometry (HRXRD)

Structural information about the samples like lattice constants, strain and composition of ternary alloys can be gained exploiting high resolution X-Ray diffractometry (HRXRD). The setup used is a Panalytical X'Pert diffractometer containing a hybrid monochromator with a mirror and a germanium (220) crystal monochromator. The beam divergence is $\Delta\theta = 47\,\mathrm{arcsec}$. For excitation the $K_{\alpha 1}$ line of a copper X-Ray source having $\lambda = 1{,}54056\,\text{Å}$ is used. The sample can be adjusted mechanically via an Euler-Cradle along 6 axes. The detection is done by an X'Celerator, based on a CCD-Array. This can be seen in Figure 3.5.

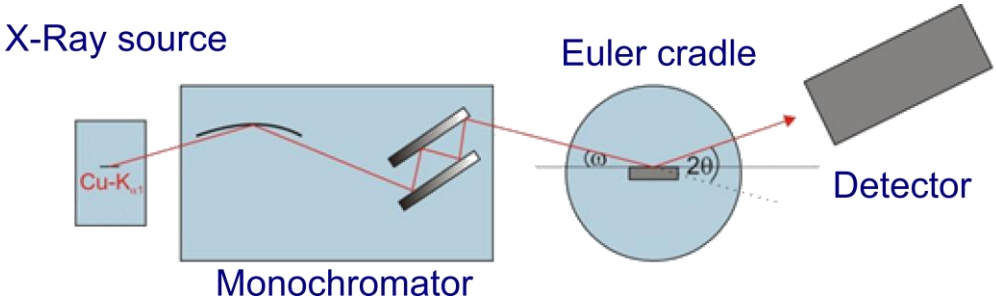

Figure 3.5 The important optical components in the HRXRD setup are the Cu source and a four crystal monochromator which filters the $K_{\alpha 1}$ line. The detection is accomplished with a CCD array.

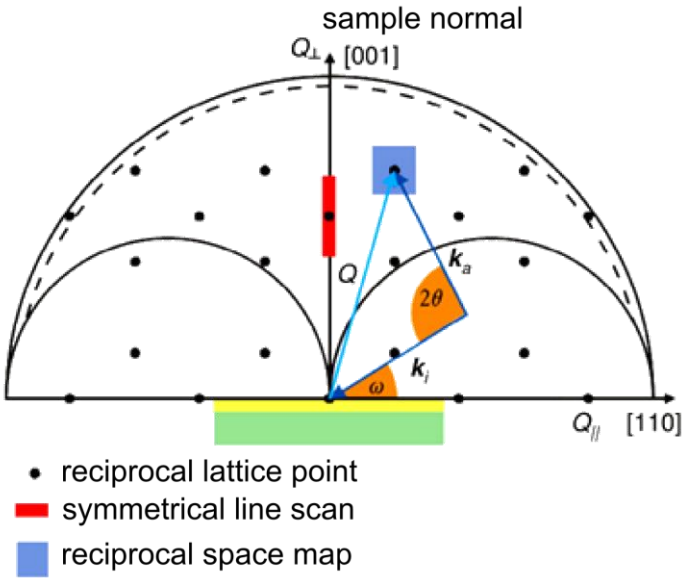

Figure 3.6 Schematic overview of the diffraction spots in reciprocal space. The excitation is done with an angle of ω and the detection angle is 2θ [37].

Figure 3.6 depicts the sample geometry and the reciprocal space. The Reciprocal Space Map (RSM) in (113) direction leads to different reciprocal lattice constants

caused by the projection of the true lattice constant on the lattice constant parallel and orthogonal to the surface $Q_{||}$ and $Q_{\perp}$. In order to calculate the true lattice constants, the formula for the plane distance d_{hkl} can be used. It depends on the lattice constant a_0 and the Miller indices h, k, l. For a cubic lattice the formula is given by:

$$d_{hkl} = \frac{a_0}{\sqrt{h^2+k^2+l^2}} \tag{3.1}$$

For the (113) direction this formula can be adjusted to:

$$Q_{||} = \frac{2\pi}{a_{xy}/\sqrt{h^2+k^2}} = \frac{2\pi}{a_{xy}/\sqrt{2}} \tag{3.2}$$

$$Q_{\perp} = \frac{2\pi}{a_z/\sqrt{l^2}} = \frac{2\pi}{a_z/3} \tag{3.3}$$

There are several measurements possible, which provide different information about the reciprocal space as described in the following.

3.5.1.1 ω-Scan

At first a “Rocking-curve” (ω-scan) can be performed in order to evaluate the dislocation density D. The defect densities are calculated from the full width at half maximum (FWHM) ΔΘ of an ω-scan of the (002) diffraction peak [33]. The dislocation density D can be determined with the length of the Burgers vector b.

$$D = \frac{\Delta\theta^2}{9b^2} \tag{3.4}$$

The Burgers vector for a dislocation in a cubic zinc-blende crystal, such as c-GaN and c-AlN, can be expressed by $b = a_0/\sqrt{2}$, where a is the lattice parameter [34]. The lattice constant for c-GaN is a_0 = 0.4503 nm [35], [36].

3.5.1.2 ω-2θ-Scan

Another possibility is the ω-2θ-scan, which allows for information about the strain. In this scan the ω angle is always the same as the 2θ angle. This provides a line scan perpendicular to the $Q_{||}$ axis, as can be seen in Figure 3.6 (red line). This will be further described in the chapter 5.2.

3.5.1.3 Reciprocal Space Maps

In Figure 3.6 one reciprocal space map (RSM) is shown by a blue square, in this map a region of the reciprocal space is measured. For different ω an ω-2θ scan is done, to achieve such a RSM. The calculation needed to form a RSM with the ω-2θ measurements are: [38]

$$Q_{||} = \frac{2\pi}{\lambda}(\cos(2\theta - \omega) - \cos\omega) \tag{3.5}$$

$$Q_{\perp} = \frac{2\pi}{\lambda}(\sin(2\theta - \omega) + \sin\omega) \tag{3.6}$$

For strain investigation an asymmetric RSM of the (113) reflex is needed. This plane is visible in Figure 3.7 as a pink triangle.

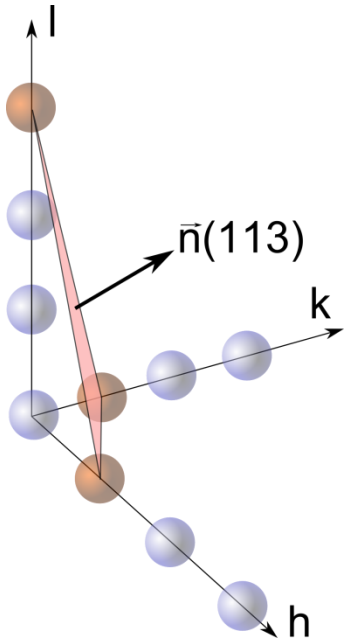

Figure 3.7 Visualization of the (113) plain important for strain measurements.

3.6 IR Absorption Setup TU Dormtund

A general sketch of the absorption setup used in the workgroup of Markus Betz in TU Dortmund Department of Experimental Physics 2 is shown in Figure 3.8. For excitation a IR Thorlabs SLS201 lamp with SLSC1 optic emitting from 360 nm to 2600 nm is used followed by a polarisation filter and a pinhole (d =2 mm). The polarisation filter allows for excitation of TE or TM only. The light is focused on the sample by a lens to a spot diameter of 0.5-0.8 mm. The transmitted light is collected with a 400 µm fibre. A chopper is placed in front of the spectrometer entrance. At the spectrometer an InGaAs-Photodiode is attached and furthermore extended with a Lock-In system (Stanford Research Systems SR830 DSP).

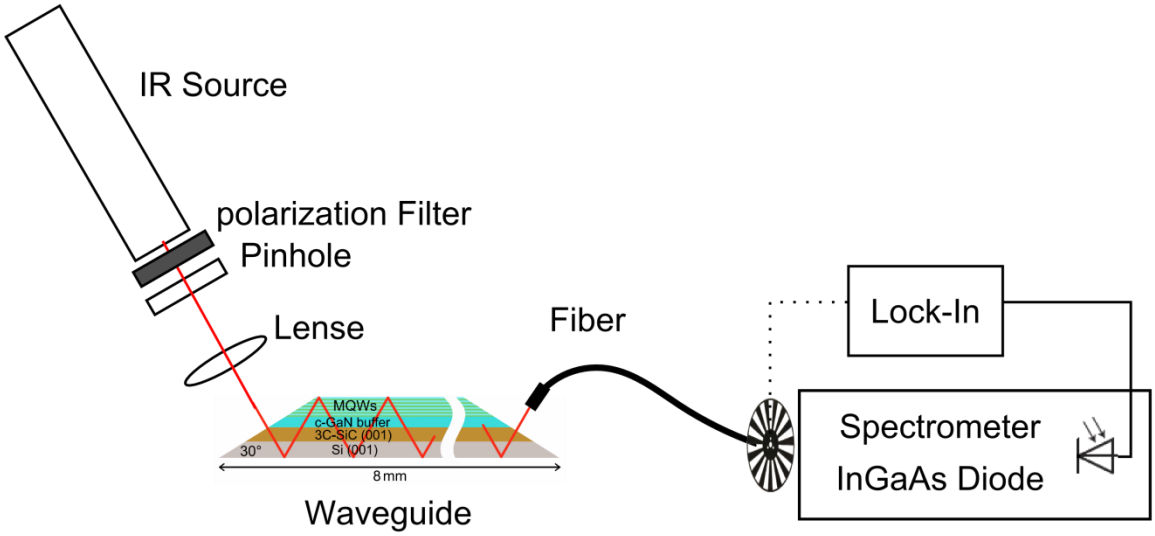

Figure 3.8 Sketch of the absorption setup used for the IR absorption measurements. (AG Betz TU Dortmund)

3.7 Spatially-resolved Raman Spectroscopy

The investigation of the longitudinal optical mode was performed by a µ-Raman setup in back scattering geometry in the workgroup of Artur Zrenner in the University of Paderborn. These experimental data lead to a correlation of the FWHM of the Raman mode with the dislocation density obtained by HRXRD. The setup is shown in Figure 3.9.

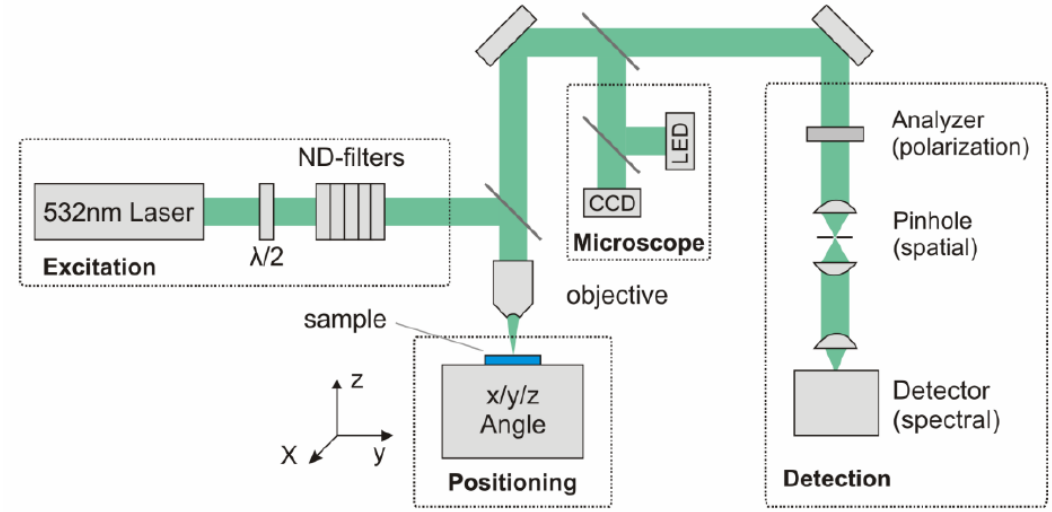

Figure 3.9 Sketch of the µ-Raman setup. The sample is excited with a Nd:YAG CW laser (532 nm). The detection is done by a holographic grating spectrometer with an applied CCD camera. (AG Zrenner Paderborn)

For excitation a frequency doubled Nd:YAG CW laser at 532 nm wavelength and 50 mW output power is used. The light is focused on the sample by an objective lens (Mitutoyo Plan APO 100x) with a numerical aperture of 0.7. The achievable spot diameter on the sample is less than 1 µm

The scattered light is analysed in terms of (linear) polarisation, spatial origin and spectral composition. A pinhole module with 10 µm diameter spatially filters the signal. The spectral analysis is performed by a holographic grating spectrometer (Kayser Optical Systems, Holospec f/1.8i) with integrated Notch-filter and focused on a CCD camera (Andor Newton, BI, 1024 Pixel x 256 Pixel). The used grating covers a spectral range from approximately $0\,\mathrm{cm}^{-1}$ to $4000\,\mathrm{cm}^{-1}$ with a resolution of $2.3\,\mathrm{cm}^{-1}$. A more detailed description of the setup can be found in [39],[40].

3.8 Picosecond Acoustics TU Dormtund

The setup exploiting strain pulses to shift the photon energy of a thick QW is based on a time-resolved pump-probe setup. The setup is placed in the workgroup of Manfred Bayer in TU Dortmund Department of Experimental Physics 2 (see Figure 3.10). For this setup only one laser is used for the pump pulse and the probe pulse. The pump pulse creates acoustic pulses in the sample. For this step the Si substrate layer is thinned to 90 µm and a 100 nm thick Al layer is evaporated on the backside of the sample, to achieve a good absorption. The absorbed light induces a temperature change leading to a strain pulse, which travels through the sample [41]. The light source is an optical parametric amplifier with pulses of 100 fs duration, a wavelength between 700 - 900 nm, and a repetition rate of 30 kHz. In front of the source a 90/10 beam splitter divides the pump and the probe pulses. In order to achieve the time tuning, a mechanical delay stage in the pump pulse is used. Then the pump pulse is focused on the Al coated backside of the sample with a spot diameter of about 100 µm. The probe beam passes a nonlinear BBO crystal (Beta-Barium-Borat) to generate second harmonic light. To reduce additional phonons influencing the acoustic pulse, the sample is cooled in a flow cryostat reaching 40 K [42].

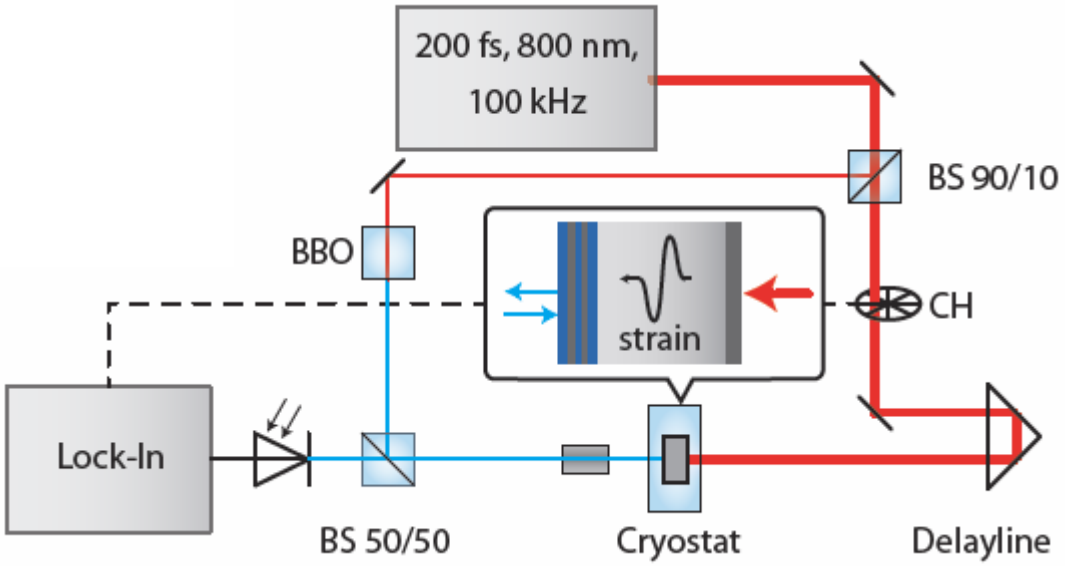

Figure 3.10 Sketch of the pump probe setup for measuring picosecond acoustics. (AG Bayer TU Dortmund)

3.9 Intraband Non-linear Measurements TU Dortmund

The third order nonlinear susceptibility can be measured by a degenerate femto-second pump probe setup in the workgroup of Markus Betz in TU Dortmund Department of Experimental Physics 2, visible in Figure 3.11. For excitation a laser together with an optical parametric amplifier (Coherent OPA 9850) is used, which emits ~50 fs pulses at 250 kHz repetition rate. Its central wavelength is tuneable from 1375 nm (0.8 eV) to 1550 nm (0.9 eV). The pump and the probe pulse are focused at the sample with a spot FWHM of ~50 µm at a relative angle of ~10°. The transmission change $\Delta T = T$ of the probe signal caused by the pump pulse is measured with Lock-In detection. For investigation of the intersubband transition (ISBT) polarisation dependent measurements have to be done. This is realised with a polarisation filter directly in front of the source. Furthermore the sample is tilted to an angle of incidence of ~65. Due to the non-linear properties of the Si substrate, the sample is glued onto a fused silica window at the MQW side and the Si was removed mechanically from the backside. The time resolution is realised with a motorised delay stage in the pump beam.

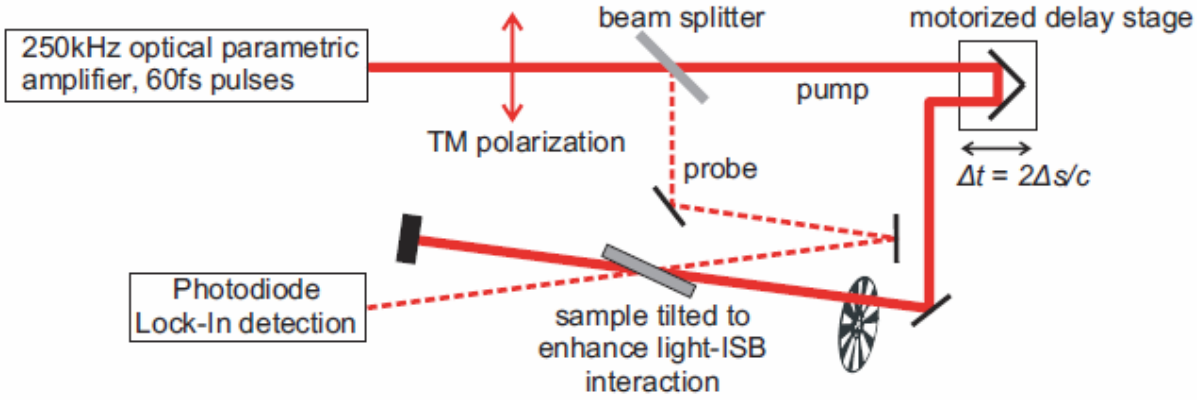

Figure 3.11 Sketch of the pump probe setup for measuring intraband non-linearity. (AG Betz TU Dortmund)

4 Results and Discussion

Many of the results described in this thesis have already been published. A general comparison of the defect densities in GaN bulk layers measured with Raman spectroscopy and high resolution X-Ray diffractometry (HRXRD) was done together with Michael Rüsing of AG Zrenner University of Paderborn [29]. Another analysis about strain pulses in GaN/$Al_xGa_{1-x}N$ single QWs was done by Thomas Czerniuk with a time-resolved pump-probe setup [43]. Besides the optical behaviour of asymmetric GaN/$Al_xGa_{1-x}N$ double QWs are studied in great detail using PL [12], time-resolved PL [14] and PLE [13] measurements which were partly provided by Gordon Callsen of AG Hoffmann TU Berlin. These investigations revealed the barrier thickness at which the coupling for GaN/$Al_xGa_{1-x}N$ double QW starts. This information is important for the design of the GaN/AlN MQWs, to reduce the FWHM of the IR absorption.

IR absorption experiments on GaN/AlN MQWs were performed by Thorben Jostmeier of AG Betz in TU Dortmund [10] and TEM measurements on similar structures have been done by Torsten Rieger of AG Pawlis in FZ Jülich [11]. First experiments concerning the nonlinear behaviour of MQW intersubband transitions (ISBT) have been executed by Thorben Jostmeier [10].

4.1 GaN Bulk: Raman and Defect Density

The crystal quality depends on the amount of defects in the layer, limiting the optical and electrical properties in semiconductor devices. The common method to investigate the structural quality of epitaxial layers is HRXRD. Another method is Raman spectroscopy (RS) providing the vibrational properties of such structures [44], [45]. RS is sensitive to the crystal structure, symmetry and different phases [46], [47], defects [30], dielectric constants [48] or free carrier densities [49], [50], [51]. Both methods can be used to investigate the details of the defects, which inflict the crystal quality. This information can be used to optimise the growth processes. Raman enables the investigation of very thin layers, barely measureable with HRXRD. Thus this first experiment with bulk GaN is a starting point for the determination of important parameters of MQWs, like doping in the QWs and defects especially for MQW with few periods. Hall Effect measurements on MQW are difficult because of the background doping of the thick substrate layer. The thickness of the MQWs is in the order of 100-300 nm this is much smaller than the 10 µm thick 3C-

SiC. Up to now a series of MQWs with different doping profiles is planned to investigate the influence of the doping on the Raman spectra.

In previous reports stacking faults (SFs) along (111) planes have been identified to be the dominant defect type in c-GaN [52-56]. The amount of this defect is directly correlated to the smoothness of the substrates [57]. A well-established technique used to decrease this defect type, is the growth of thick layers. Unfortunately this defect leads to hexagonal inclusions in the cubic phase, caused by the change in the stacking period of the atoms. Due to the SFs geometry an annihilation process occurs, in case of two SFs, with (111) and $(11\bar{1})$, meet in the crystal. Only sessile dislocations [58], [59] remain, which leads to an increase of crystal quality for thicker layers [57].

In order to compare both characterisation methods a series with thick cubic GaN (001) layers were grown on a 10 µm 3C-SiC (001) layer deposited on a 0.5 mm thick Si substrate. The layer thickness was increased from 75 to 505 nm as can be seen in Table 4.1. More details concerning the growth of cubic GaN on 3C-SiC can be found in [60]. Atomic force microscopy measurements revealed an RMS surface roughness of around 5 nm for 5×5 µm² areas. The layer thicknesses have been measured by Reflectometric Interference Spectroscopy in case of the thickest samples (thicker than 300 nm) with a resolution in the range of ±25 nm [61]. For the thinner samples a similar growth rate is assumed, leading to estimated thicknesses.

Figure 4.1 shows two ω profiles of the thickest and the thinnest sample, in order to compare the FWHM of both layers. The sample GNW2350 is 75 nm thick leading to a very high FWHM compared to the sample GNW2345 with 505 nm thickness. To evaluate the FWHM Voigt functions are used. With this FWHM the dislocation density was calculated as described in chapter 3.5.1.1. High dislocation densities cause disorder in the material resulting in a broader FWHM. Thus the FWHM can be used to determine the dislocation density.

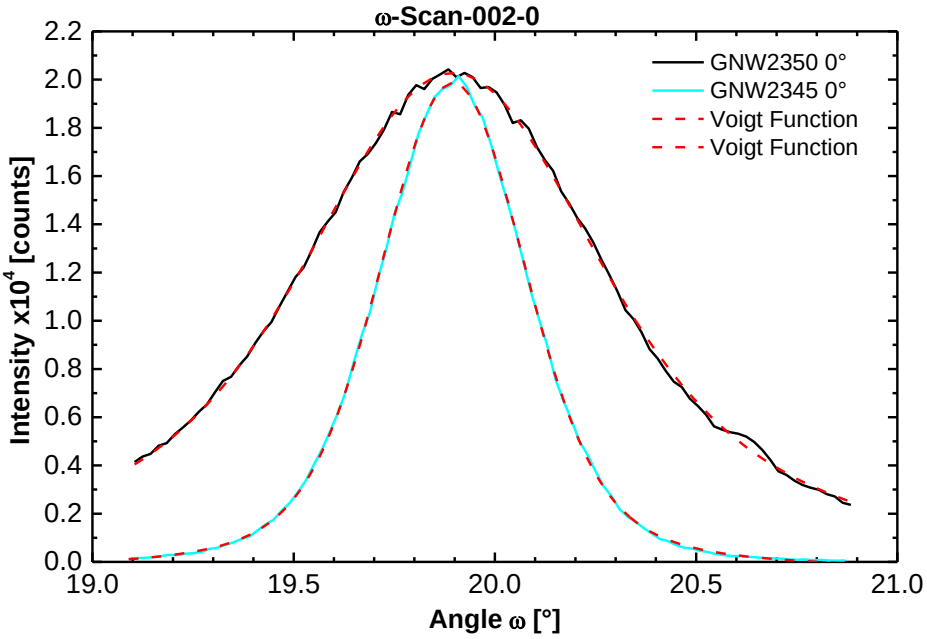

Figure 4.1 Omega profile of the thickest sample GNW2345 (505 nm) and the thinnest sample GNW2350 (75 nm). A clear decrease of the FWHM for the 505 nm thick sample can be seen.

The most important parameters of the samples are summarised in Table 4.1. The previously described decrease of the defect density D (see chapter 3.5 for details) of one order of magnitude for thicker layers can be observed in the measured data. The values are in the typical range reported for c-GaN grown on 3C-SiC substrate [54], [57], [59]. Also a saturation in the quality improvement above 400 nm is well known, because the SFs have mostly annihilated and other defects become important. More details on the evaluation of the data can be found in [29].

Table 4.1 Collection of the most important results of the c-GaN bulk layer series. The defect density D is calculated by the HRXRD Δθ. A correlation of the layer thickness d with the defect density D and the Raman FWHM $\Delta\bar{\nu}$ can be seen. (Evaluation done together with Michael Rüsing)

Nr	d [nm]	Δθ [arc min]	D [10^9 cm^2]	$\Delta\bar{\nu}$ [cm^{-1}]
GNW2345	505	32.4	9.73	11.2
GNW2346	460	31.3	9.06	10.8
GNW2347	475	32.9	10.0	11.1
GNW2348	380	35.4	11.6	10.7
GNW2349	150	42.6	16.8	12.9
GNW2350	75	49.2	22.4	13.4

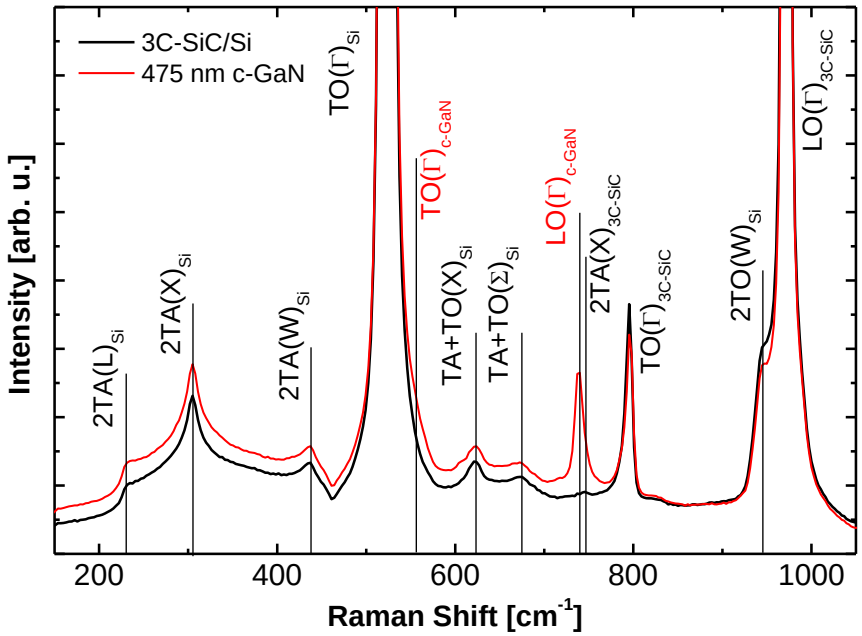

Figure 4.2 A comparison of Raman spectra of a 3C-SiC/Si substrate piece (dashed) and a thick c-GaN layer (red) reveals two additional peaks (marked in red). These peaks are attributed to the TO and LO mode of c-GaN. (Measured in University of Paderborn by Michael Rüsing)

Figure 4.2 shows a typical back-scattering Raman spectrum of c-GaN on 3C-SiC/Si substrate (red) with a reference 3C-SiC/Si substrate (dashed). Various distinct features are visible in the spectrum, which are mostly related to the substrate. By comparing both spectra only two features are different and labelled in red. These features correspond to the c-GaN (at $738\ \mathrm{cm}^{-1}$ is the LO mode and at $550\ \mathrm{cm}^{-1}$ is the TO mode). They are similar to the values in literature [46], [30], [51]. The TO mode is barely visible, due to the selection rules in c-GaN. Thus the main results are concentrated on the LO mode only. Besides even small inclusions of hexagonal GaN results in a strong peak at $560-570\ \mathrm{cm}^{-1}$ [30], [62], but this peak is absent in all investigated samples. This is a proof for the cubic phase purity of the samples.

In addition, an estimation of the layer thickness is possible by comparing the integrated intensities of the LO mode. This is suitable even for thin layer, which are difficult to measure by HRXRD. This linear correlation is plotted in Figure 4.3.

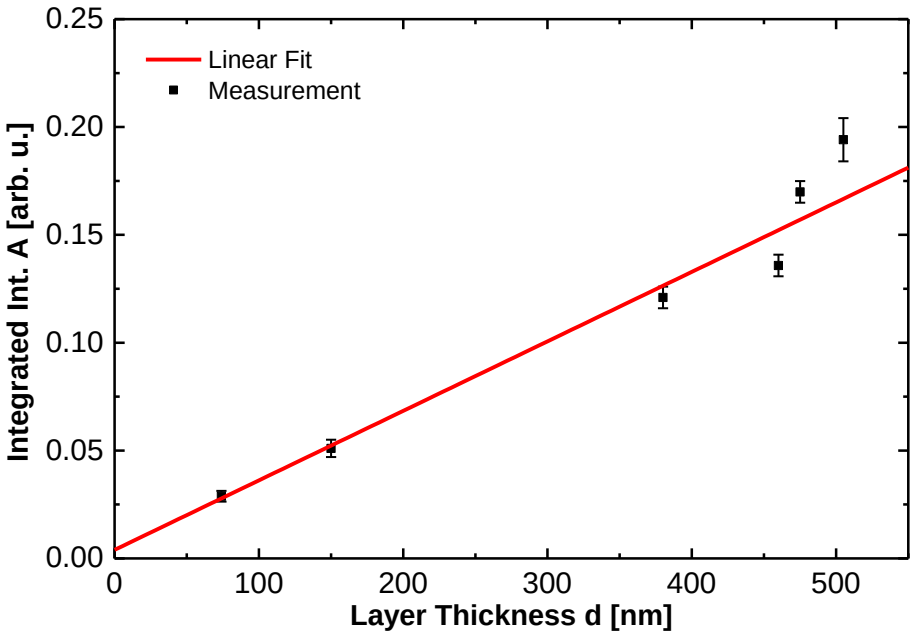

Figure 4.3 Raman spectroscopy enables another way to measure the thickness of layers. A linear correlation between the integrated intensity, given by the area underneath the LO Raman line A, of the LO mode and the layer thickness of c-GaN bulk layers can be seen. (Evaluation done together with Michael Rüsing)

Figure 4.4 shows the connection between the dislocation density determined via HRXRD with the FWHM of the LO mode $\Delta\bar{\nu}$ measured with Raman. A linear trend is found. This enables Raman spectroscopy as a further investigation method, in order to get information about the structural quality.

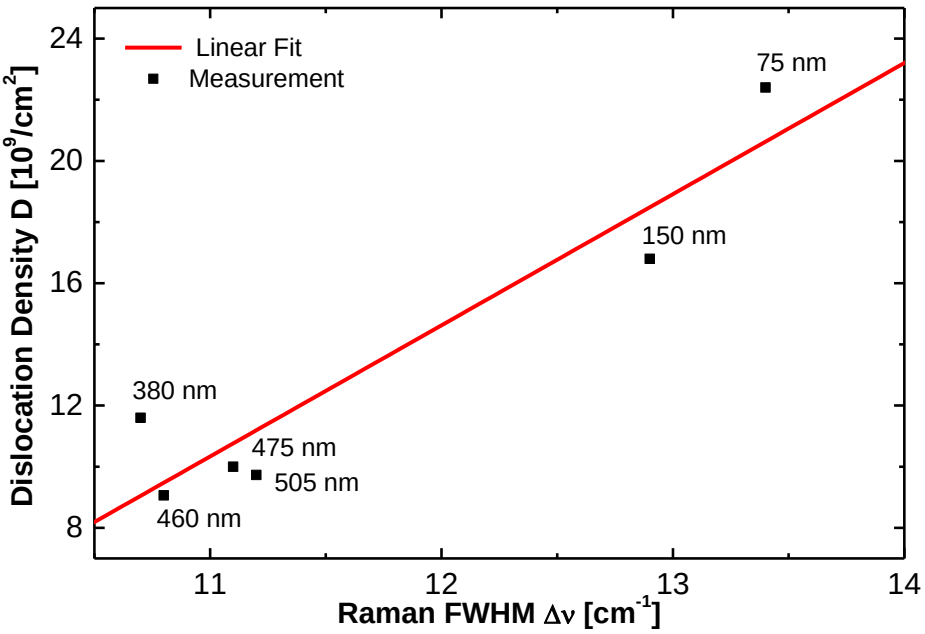

Figure 4.4 A linear correlation between the dislocation density D via HRXRD and Raman FWHM $\boldsymbol{\Delta\bar{\nu}}$ is found. These data can be used as a calibration to determine the dislocation density with Raman only. (Evaluation done together with Michael Rüsing)

With this data a calibration between HRXRD and Raman is found. Thus further determination of the dislocation density of c-GaN layers can be done via Raman spectroscopy only. This enables a spatial resolved investigation of the defects. Furthermore these first results can be adapted to more complex samples like MQWs leading to a possibility to measure also structures with only a few periods. HRXRD can only be used to measure thick samples with several periods.

4.2 Thick QW: Strain Pulse

Picosecond acoustics can be used to investigate the influence of strain pulses on heterostructures. Due to strain pulses the optical response of the material changes leading to different emission/absorption in QWs compared to the unstrained case. With this knowledge detectors for sub terahertz and terahertz elastic waves can be designed with picosecond temporal resolution. The group III nitrides are suitable for measuring coherent phonons with frequencies up to 2 THz [63-72]. Besides the different layer thicknesses can be modelled enabling a detailed insight into the real layer thicknesses and the interfaces of the different heterostructures. Complex MQW structures with several periods have not been investigated so far, but the basic principle is shown for a single QW structure. This provides information about the strain behaviour of the different layers. More details can be found in [43]. After the publication of [43] further investigation revealed a deviation of the nominal layer thicknesses. Here the newest results are shown, as written in [73].

Two single cubic GaN/$Al_xGa_{1-x}N$ QWs were analysed with picosecond acoustic pulses revealing a sufficient change in the signal to serve as a detector. Their backside Si(100) is thinned to 90 µm and coated with 100 nm Al, in order to excite the samples by a laser together with an optical parametric amplifier. The undoped QW is 10 nm thick surrounded by 35 nm thick $Al_xGa_{1-x}N$ barriers. The Al content in the barriers is different for the two investigated samples. The sample GNW2446 has an Al content of x = 0.1 and GNW2448 has x = 0.8. In addition, a 550 nm thick reference c-GaN bulk sample (GNW2424) was investigated, to compare with the two ADQWs. On the backside of the sample an Al film is evaporated, to heat the sample with the pulses. The sample structure is shown in Figure 4.5.

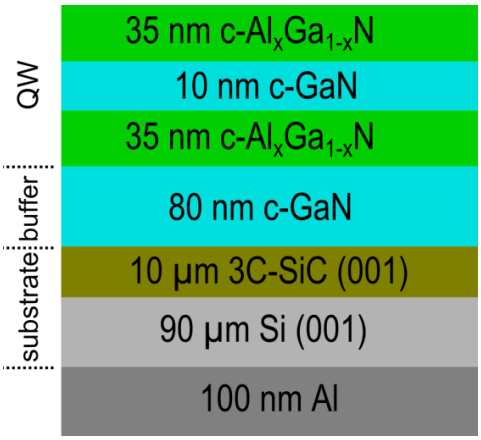

Figure 4.5 Single QW structure consisting of a 10 nm thick c-GaN QW and 35 nm thick c- $Al_xGa_{1-x}N$ barriers. Two samples are investigated with different Al content of 0.1 (GNW2446) and 0.8 (GNW2448).

In Figure 4.6 two normalized PL spectra at low temperature are plotted. The dashed curve corresponds to the QW sample with $Al_{0.8}Ga_{0.2}N$ barriers, the emission is shifted by 45 meV compared to the bulk c-GaN reference (straight line). The energy shift is caused by the quantisation energy of the QW emission. For the sample with $Al_{0.1}Ga_{0.9}N$ the quantisation energy of the QW and the $Al_{0.1}Ga_{0.9}N$ emission cannot be resolved in the experiment. Thus we focus only on the sample with high Al content.

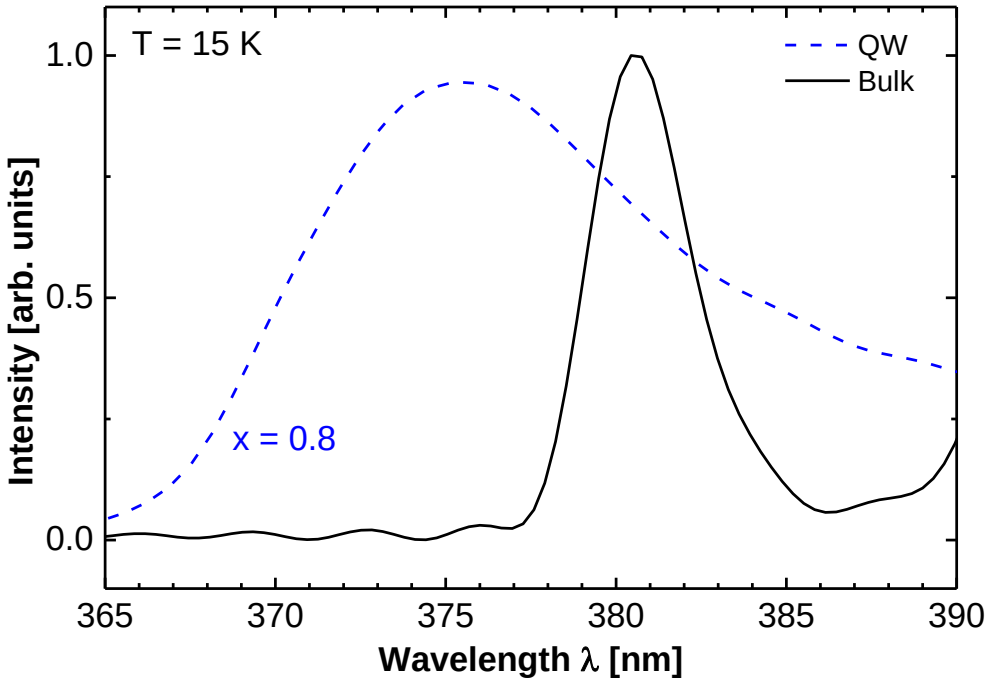

Figure 4.6 PL spectra for the reference c-GaN sample (GNW2424) and the QW structure with $Al_{0.8}Ga_{0.2}N$ (GNW2448) at low temperature. The excitation was done with a Nd:YAG laser emitting at 266 nm with 5 mW. (Measured in University Paderborn by me)

For the picosecond acoustics the Al film absorbs the optical energy of the laser and is heated locally. Thermal expansion launches an acoustic pulse into the Si substrate at this spot. This pulse travels through the whole sample and is transmitted/reflected at each interface. When the pulse approaches at the GaN bulk and QW layer, it interferes with the probe beam. The probe beam is reflected at the sample surface and at the acoustic pulse and Brillouin oscillations are formed [74]. This leads to an interference, which is complicated by all the transmitted/reflected waves of the different interfaces. The measurements for two different pump powers (W_0 and $4W_0$) are shown in Figure 4.7. The curve for a probe wavelength of 370 nm shows a simple shape, as expected for a picosecond strain pulse in a thin layer near the surface [65] ,[66]. In this case the shape is mainly caused by the QW layer. For the probe wavelengths 375 nm and 380 nm the shape gets more complicated, due to the increasing contribution of the c-GaN layer. For the wavelength of 370 nm the QW is in resonance with the pump signal and in case of 380 nm the c-GaN buffer layer is in resonance. The $Al_{0.8}Ga_{0.2}N$ layer does not contribute to the measurement, because of the much higher bandgap energy compared to the QW emission. The parameter β is the ratio of the photo elastic coupling efficiency of the QW over the one of the bulk layer.

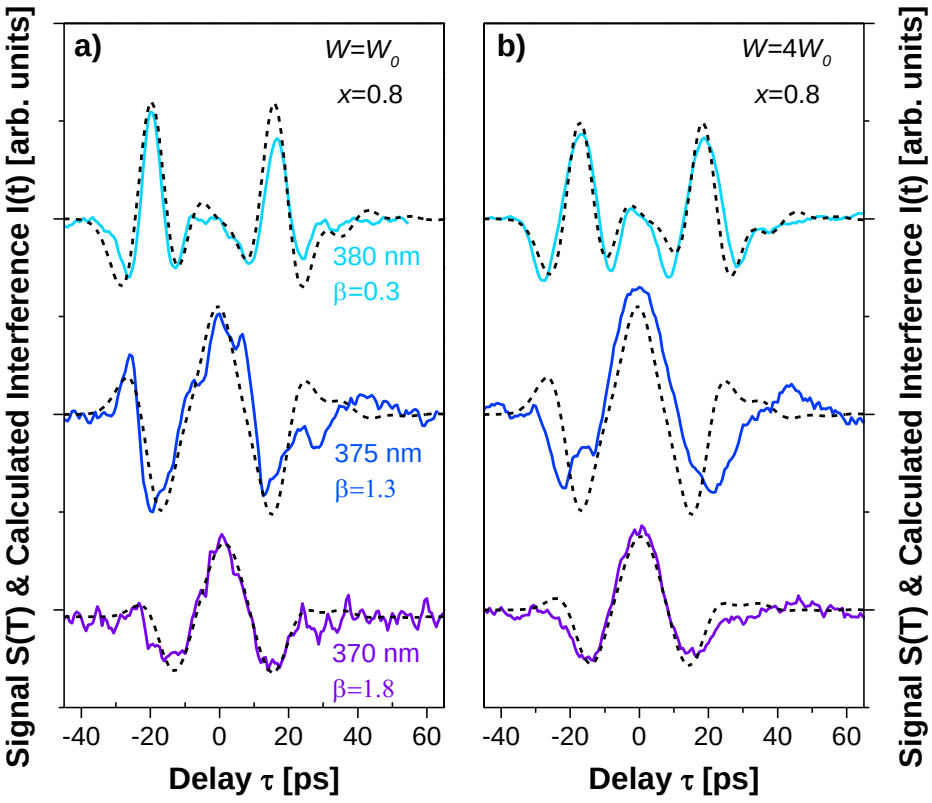

Figure 4.7 Measured acoustic signal (dashed lines) and simulated signal (straight lines) for the sample with x = 0.8 (GNW2248) for three different probe wavelengths. The pump power was increased from W_0 (left) to $4W_0$ (right). The parameter β represents the ratio of the photo elastic coupling efficiency of the QW over the one of the bulk layer. (Measured in TU Dortmund by Thomas Czerniuk) [73]

For a theoretical understanding two contributions to the measurements should be considered. The first is the photo elastic effect, which changes the band gap and refractive index in case of strain. The second part is caused by interferences of the reflected light at the surface and the interfaces, leading to a phase shift and displacement. The simulations shown in Figure 4.7 are performed with an input acoustic pulse, which propagates through the sample (calculated via transfer-matrix and scattering-states method), in order to get the strain and displacement profiles. These simulations reveal a stronger contribution of the photo elastic response compared to the interface displacement effect.

These results validate the elastic constants which are also used for the simulations of the optical transitions (nextnano³) and the strain investigations via MadMax. Thus the parameter set needed for a complete understanding of c-GaN/c-AlGaN is confirmed.

4.3 Asymmetric Double Quantum Wells (ADQW)

In order to get an insight into the basics of a quantum cascade laser (QCL), as a first step asymmetric double quantum wells (ADQW) were grown and investigated. The following chapters covering the ADQWs are divided in 3 main topics. At first two series with average Al content of x = 0.26 ± 0.03 and x = 0.64 ± 0.03 in the barriers were used to investigate the coupling of the two QWs depending on the barrier thickness between them. The second part covers the time-resolved measurements on the ADQWs series with Al content of x = 0.64 ± 0.03 dealing with the carrier dynamics in more detail. In the third chapter one sample of the first series with x = 0.25 ± 0.03 was investigated exploiting photoluminescence excitation spectroscopy (PLE) leading to more information about excited energy levels. By collecting the data of these chapters the model and parameters used in the nextnano³ simulations are adapted and the prediction of the emission and absorption for more complex structures like MQWs important for quantum cascade lasers can be done. Nearly all of the measurements and the complete analysis of this chapter have been performed by me with the assistance of the mentioned cooperation partners.

4.3.1 General Characterisation

The growth of c-GaN and c-$Al_xGa_{1-x}N$ was realised at a substrate temperature of T_S = 720 °C under one monolayer of Ga excess on the surface. More details concerning the growth of cubic GaN on 3C-SiC can be found in [60]. The Al, Ga and N shutter have been opened together for the c-$Al_xGa_{1-x}N$ layers, in order to measure RHEED oscillations. Two series of ADQWs have been grown with different Al content in the $Al_xGa_{1-x}N$ barriers. The first series consists of $Al_xGa_{1-x}N$ barriers with x = 0.26 ± 0.03 (Series 0.26) and the second has x = 0.64 ± 0.03 (Series 0.64). In both cases the substrate consists of a 10 µm 3C-SiC (001) layer deposited on a 0.5 mm thick Si (001) substrate. Directly on the 3C-SiC substrate a 100 nm thick c-GaN buffer layer was grown, followed by the ADQW. The barrier thickness d between a wide quantum well (QW_W) and a narrow quantum well (QW_N) was varied between 1 nm and 15 nm. The ADQW structure is embedded between two 50 nm thick cubic $Al_xGa_{1-x}N$ layers. The sample structures are shown in Figure 4.8.

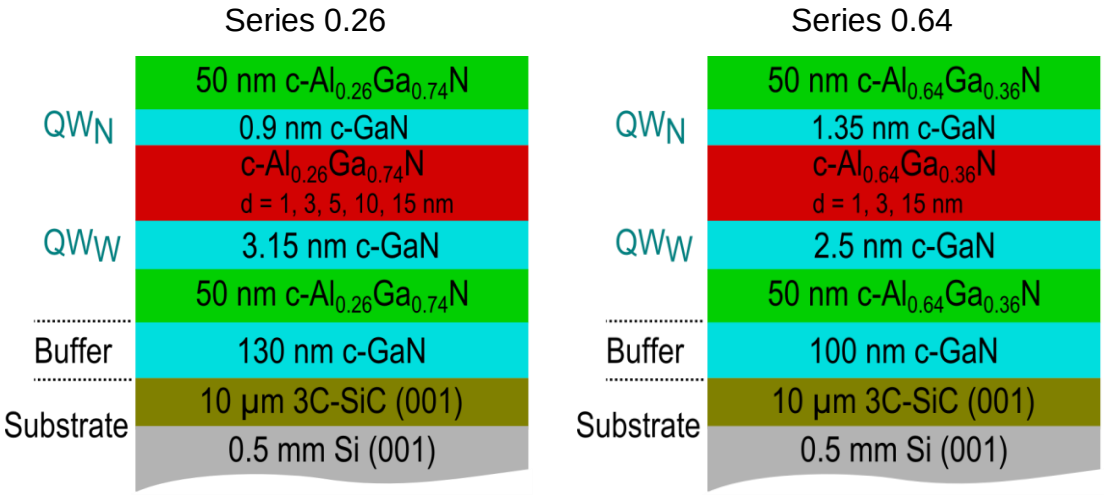

Figure 4.8 Sample structure of the two ADQW series. The barrier thickness d was varied from 1 nm to 15 nm. In series 0.26 (left) the Al content is x = 0.26 ± 0.03 and for series 0.64 (right) the Al content is x = 0.64 ± 0.03.

Some of the important parameters of the two ADQW series are summarised in Table 4.2.

Table 4.2 Overview of the parameters for the two ADQWs series.

Parameter	**Series 0.26**	**Series 0.64**
Degree of Relaxation R	0.4 ± 0.05	0.48 ± 0.07
Barrier Thickness d [nm]	1, 3, 5, 10, 15	1, 3, 15
Al content in barriers	0.26 ± 0.03	0.64 ± 0.03
Thickness wide QW [nm]	3.15 ± 0.225	2.5 ± 0.225
Thickness narrow QW [nm]	0.9 ± 0.225	1.35 ± 0.225

AFM measurements revealed a rms surface roughness for 5x5 µm^2 areas reaching from 1.9 nm to 2.6 nm for the series 0.26 and around 4 nm for the second series. Other structural properties were characterized by high resolution X-Ray diffraction (HRXRD). The defect density of the order of $D = 2 \times 10^{10}\ \mathrm{cm}^{-2}$ was determined by rocking curve FWHM around the (002) reflection. From the reciprocal space map (RSM) around the (113) reflection the Al content could be determined. As an example a RSM of one sample of the series 0.26 is shown in Figure 4.9 (left). In this case the Al content was measured to x = 0.25 ± 0.03. From this RSM also the degree of relaxation R = 40% of the $Al_xGa_{1-x}N$ layers is provided. One sample of the se-

ries 0.64 has an Al content of x = 0.62 ± 0.03 and the degree of relaxation is R = 48% (Figure 4.9 on the right). All c-$Al_xGa_{1-x}N$ layers in all ADQWs are partly tensile strained to the GaN buffer layer, thus an equilibrium lattice parameter is formed in the ADQW structure leading to partly compressively strained QWs.

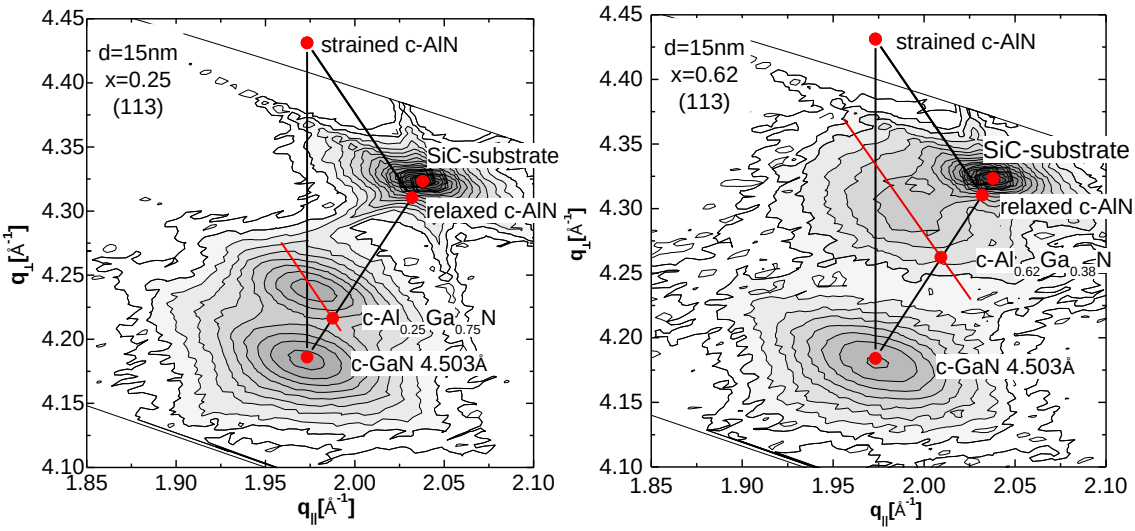

Figure 4.9 RSM of the (113) reflection of two cubic GaN/$Al_xGa_{1-x}N$ ADQW with d = 15 nm of the two different series. A partial strain of the barriers is visible in both measurements. (Left) An Al content of x = 0.25 ± 0.03 is determined. (Right) The Al content is x = 0.62 ± 0.03.

In order to evaluate the strain of the individual layers, the degree of relaxation R can be expressed by.

$$R = \frac{(a_{||} - a_s)}{a_L - a_s} \tag{4.1}$$

It describes the difference in the lattice constant of the in plane lattice constant $a_{||}$ of the investigated layer to the value of the substrate a_s and includes the lattice parameter for the unstrained layer a_L.Thus the real $Al_xGa_{1-x}N$ lattice parameter can be determined using a RSM (Figure 4.9) and this value is projected to the x axis ($q_{||}$). The substrate in this case is the GaN buffer layer [38] [76]. These strain effects are also considered in the nextnano³ calculations.

4.3.2 Influence of Barrier Thickness to the Coupling

For a detailed analysis of influence of the barrier thickness on optical measurements two series of asymmetric cubic GaN/$Al_xGa_{1-x}N$ double quantum wells (ADQWs) were grown. In both series the barrier thickness between the two QWs was varied. The series 0.26was grown with an Al content of x = 0.26 ± 0.03 and the series 0.64 has x = 0.64 ± 0.03. Figure 4.10 depicts the low temperature interband photoluminescence measurements at 13 K for the sample with d = 15 nm of series 0.26. For excitation a Nd:YAG CW laser (266 nm) was used. Four clearly distinguishable emission bands at 3.27 eV, 3.37 eV, 3.60 eV and 3.74 eV are observed. Using 4 Gaussian fit functions the emission bands were determined and they could be assigned to the c-GaN buffer [22], the wide QW, the narrow QW and the cubic $Al_{0.26}Ga_{0.74}N$ [77], respectively. The transition energies of both QWs are consistent with the calculations by nn[3] (see Table 4.3). This fit procedure was performed for all PL spectra of the series 0.26 and 0.64, in order to evaluate the intensities and the energy of the emission maximum.

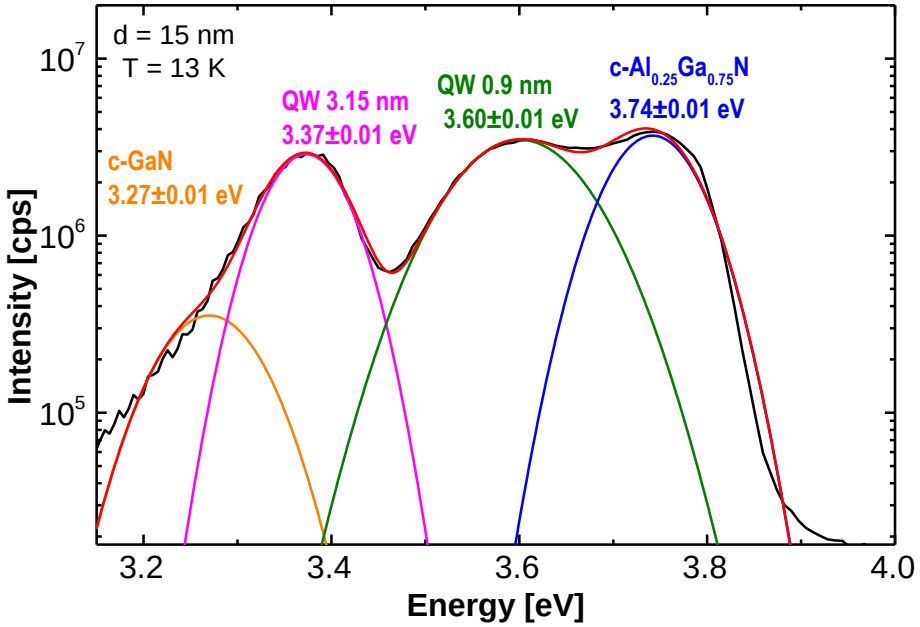

Figure 4.10 Low temperature PL spectrum of the cubic GaN/$Al_{0.26}Ga_{0.74}N$ ADQW with d = 15 nm excited with a Nd:YAG laser (266 nm).

In Figure 4.11 the low temperature PL spectra of the two ADQW series with different barrier thicknesses d are shown. For better comparison the PL spectra have been normalized to the emission of the $Al_xGa_{1-x}N$ and are plotted in a semi-

logarithmic scale. The PL experiments for series 0.64 in Figure 4.11 (right) were performed time integrated with a frequency-quadrupled, picosecond Nd:YAG laser (266 nm, 76 MHz repetition rate). The three emission bands could be assigned to the wide QW_W (3.49 eV), the narrow QW_N (3.73 eV) and the cubic $Al_{0.64}Ga_{0.36}N$ (4.12 eV) [77]. The two diagrams show a different spectral region. Due to the higher Al content of series 0.64 all emission bands are shifted to higher energies. Nevertheless the general behaviour for the different barrier thicknesses d is very similar.

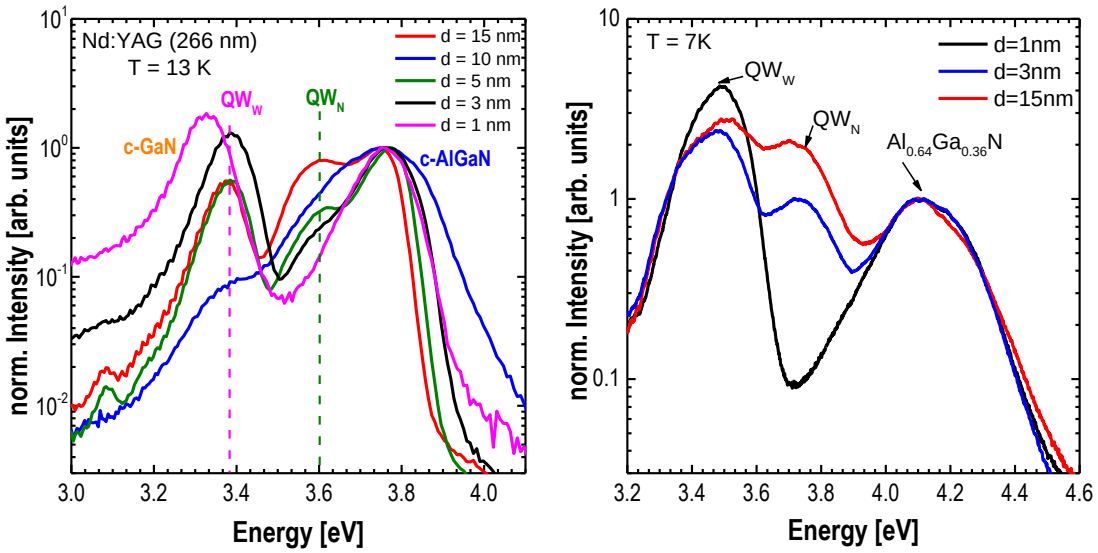

Figure 4.11 Semi-logarithmic plot of the low temperature (7 K) PL spectra of the cubic GaN/ $Al_xGa_{1-x}N$ ADQWs with x = 0.26 (left) and x = 0.64 (right). Three emission bands are visible for the wide QW (QW_W), the narrow QW (QW_N) and the $Al_xGa_{1-x}N$ barriers. The emission intensity of the narrow QW can be correlated to the barrier thickness d. (right: measured in TU Berlin together with Gordon Callsen)

A clear correlation between the intensity of the narrow QW I_N and the barrier thickness d can be seen. The emission of the narrow QW I_N decreases with increasing barrier thickness and the other way round for the wide QW. Thus coupling between the QWs is relevant for these barrier thicknesses. The energy shift of the emission of the wide QW for the sample with the lowest barrier thickness d = 1nm of series 0.26 (pink curve, left) may be caused by variation in the QW thickness of one monolayer. The sample with d = 10 nm (blue curve, left) of series 0.26 shows a strong broadening of the emission band related to the $Al_xGa_{1-x}N$ emission and the intensity of the wide QW emission is decreased compared to the other samples. The AFM, HRXRD and RHEED data of this sample are consistent with the data of

the other samples. But the PL measurements show a fluctuation of the intensities of the emission bands for different positions at this sample piece.

The intensity ratio of both QW series varies for different barrier thicknesses d (see Figure 4.12). For barriers thinner than 7 nm (series 0.26, left) and 3 nm (series 0.64, right) a strong drop in the intensity ratio is observed. This difference in barrier thickness, where the drop occurs, is caused by the higher Al content and the greater potential step at the interface. For thicker barriers no coupling is observed and a constant I_N to I_W ratio is found.

For radiative recombination processes the presence of both electrons and holes is necessary. Therefore, the carrier type with lower tunnelling rate is expected to limit the finally observed equilibrium intensity ratio in the steady state PL measurements. The intensity ratio is calculated for the carrier transfer processes for electron tunnelling (blue curve) and heavy hole tunnelling (red curve). The overall behaviour is well explained, however for low barrier thicknesses a deviation from the calculations is seen, indicating a reduced non-resonant tunnelling rate (higher I_N to I_W ratio) for thin barriers.

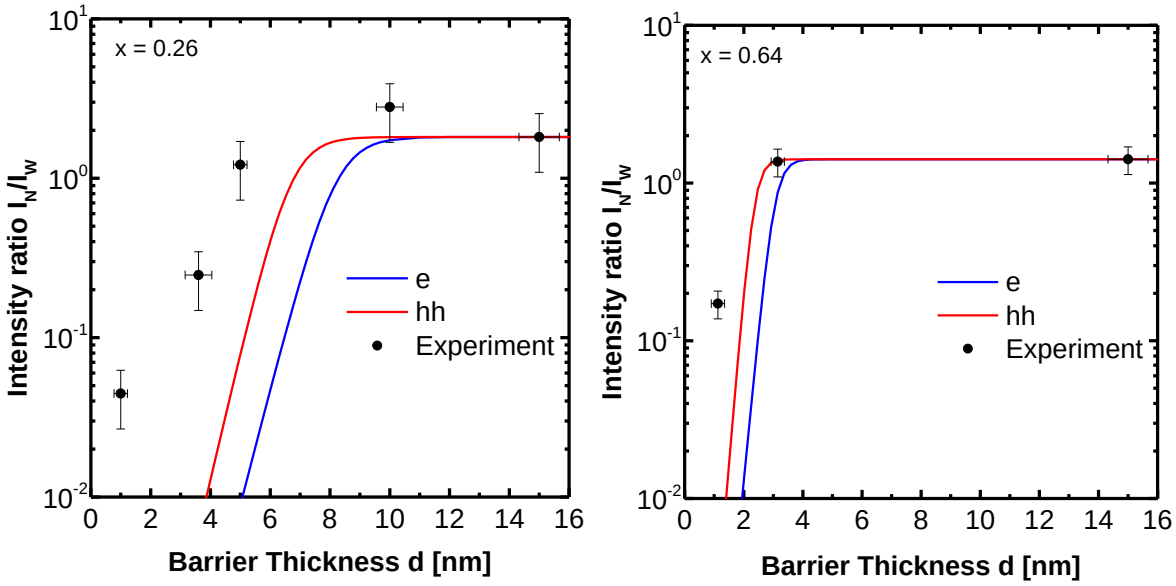

Figure 4.12 Intensity ratio I_N/I_W as a function of barrier thickness d for series 0.26 (left) and series 0.64 (right). The calculated curves for electrons (e) (blue line) and heavy holes (hh) (red line) follow the same trend as the measured ratios (dots). (Evaluation done by me)

More details for the evaluation of the data can be found in [12] [14]. We analyse the experimental results by considering the following processes (as described in chapter 2.2). Light of the excitation source is absorbed creating electron hole pairs in the

two QWs and in the surrounding barrier material, the carriers in the barriers diffuse into the QW_W and QW_N. Time-resolved PL measurements on decoupled samples estimate that the life times in both QWs are in the order of $\tau \approx 180\ ps$ for series 0.26. A detailed analysis for the times in series 0.64 is shown in the next chapter.

For the ratio of the generation rates the best match with the experimental data for the uncoupled QW with d = 15 nm is found to be $\frac{G_W}{G_N} = 0.55$ for series 0.26 and $\frac{G_W}{G_N} = 0.707$ for series 0.64. The details about the time-resolved PL measurements of series 0.64 are described in chapter 4.3.3.

The limiting process is the heavy hole transfer (red) which is slower than the electron transfer (blue). Only for thinner barriers a deviation to the experimental data (black points) is observed. A lower carrier transfer is measured than expected by our simple model. This difference between model and experiment can be explained by the parameters used for the calculation, for example the uncertainty of 5% for the band offset at the GaN/$Al_xGa_{1-x}N$ interfaces and the inaccuracy of the Al content in the barrier of $\Delta x = \pm 0.03$. Finally, scattering of carriers by defects in the barriers may increase the transfer time and lead to a higher I_N to I_W ratio.

For the comparison with the optical measurements and a detailed understanding of the energy levels, band structure calculations are accomplished with nextnano³ providing energy levels of the QWs important for the calculation of tunnelling. The parameters used for the nextnano³ simulations are summarised in the appendix. The details for the simulations are collected in chapter 5.1. The simulated and measured transition energies for the ADQWs at low temperatures are shown in Table 4.3. The ADQWs are nominally undoped. Nevertheless in all nextnano³ calculations a background n-type doping of around $5x10^{17}\ cm^{-3}$ in $Al_xGa_{1-x}N$ and of around $1x10^{17}\ cm^{-3}$ in GaN is assumed [75].

Table 4.3 Optical transitions measured via PL together with nextnano³ simulated transitions for both ADQW series.

	Series 0.26	**Series 0.64**
QW_W^{exp} **[eV]**	3.37	3.49
QW_W^{sim} **[eV]**	3.42	3.53
QW_N^{exp} **[eV]**	3.60	3.73
QW_N^{sim} **[eV]**	3.66	3.77

In Figure 4.13 and Figure 4.14 the conduction band edge and the valence band edges for electrons (e), heavy holes (hh) and light holes (lh) are plotted for the ADQW structure with the barrier of 1 nm and 5 nm. Electrons in the wide QW are confined as indicated by the dashed lines e_1 and e_2, respectively. The penetration depths of the wave functions for e, hh and lh are much larger than the 1 nm barrier thickness, leading to a different probability distribution $|\Psi_1|^2$. Therefore, a clear coupling of the two QWs and thus non-resonant tunnelling is expected, which can be described by non-resonant tunnelling of carriers. Additional calculations for the other GaN/$Al_xGa_{1-x}N$ ADQW structures with wider barrier thicknesses showed, that coupling is relevant for barrier thicknesses below 5 nm (see Figure 4.13 right). For thick barriers of d > 5 nm nn[3] simulations indicate that no significant coupling will occur.

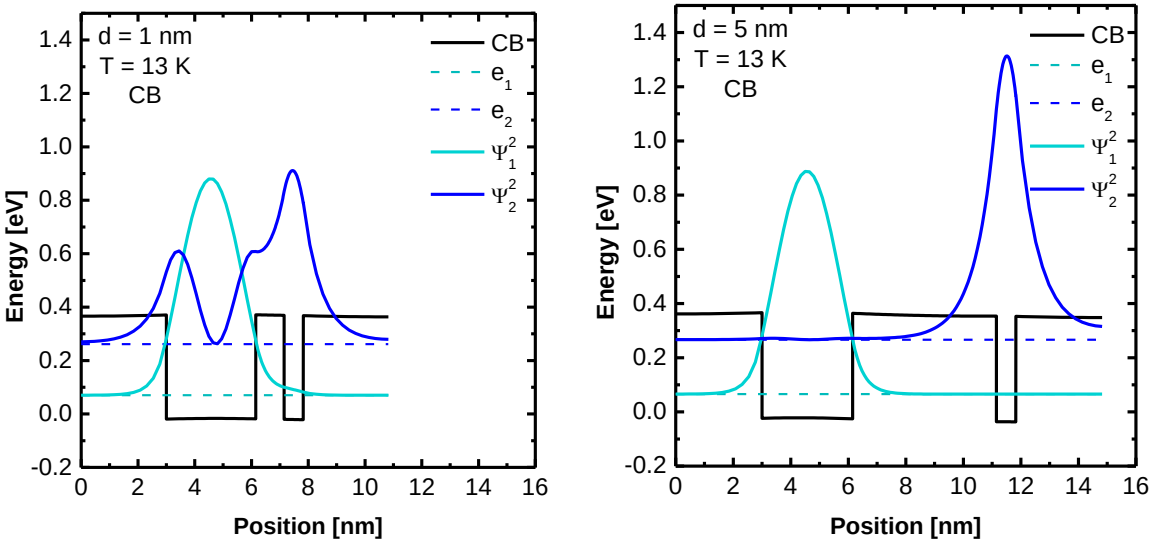

Figure 4.13 Simulated conduction band of the cubic GaN/$Al_xGa_{1-x}N$ ADQW with x = 0.26 and a barrier thickness d = 1 nm (left) and d = 5 nm (right) at 13 K.

Similar calculations of the band diagram for the heavy holes are illustrated in Figure 4.14.The general behaviour is analogous to the electrons. The wave function for the two heavy hole states hh_1 and hh_2 penetrate into the neighbouring QW leading to strong coupling of the two QWs for 1 nm barriers.

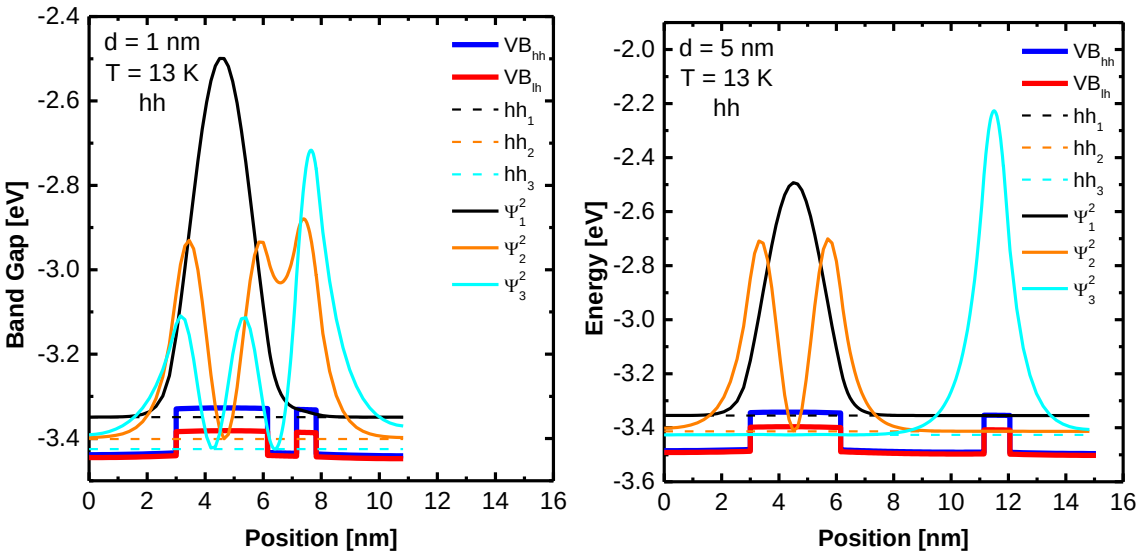

Figure 4.14 Valence bands as simulated by nextnano³ of the heavy holes (hh, blue) and light holes (lh, red) in case of the cubic GaN/$Al_xGa_{1-x}N$ ADQW with x = 0.26 and a barrier thickness d = 1 nm (left) and d = 5 nm (right) at 13 K. For clarity only the probability distribution $|\Psi|^2$ for the hh is plotted.

The residual strain measured via HRXRD leads to slightly different band gaps for heavy and light holes (blue curve for hh and red curve lh). The ground state for the lh is higher, due to their lower effective mass. Therefore we expect no e-lh transitions in PL spectra at low temperatures.

For the evaluation and understanding of the experimental optical results the exact knowledge of the different energy levels as well as the band edges is needed. The number of bound energy levels strongly depends on the Al content, which changes the depth of the potential step at the interface. This leads to different graphs for the Al contents x = 0.26 (Figure 4.15) and x = 0.64 (Figure 4.17). These energy levels are simulated with nextnano³ for a single c-GaN QW with $Al_xGa_{1-x}N$ barriers partly strained on a c-GaN buffer layer at a temperature of 13 K. Furthermore two diagrams are plotted to visualize the transition energies between the 3 electron levels and the 3 heavy hole levels (Figure 4.16 and Figure 4.18)

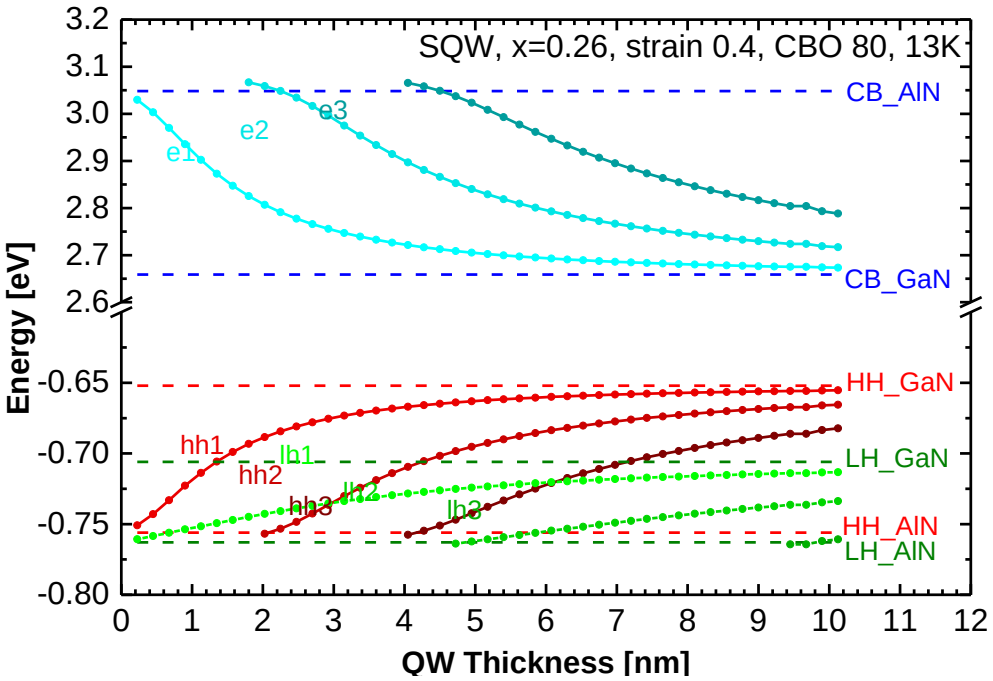

Figure 4.15 Simulated energy levels for electrons (e), heavy holes (hh) and light holes (lh) of a single c-GaN QW with $Al_xGa_{1-x}N$ barriers (x = 0.26) partly strained on c-GaN buffer at 13 K.

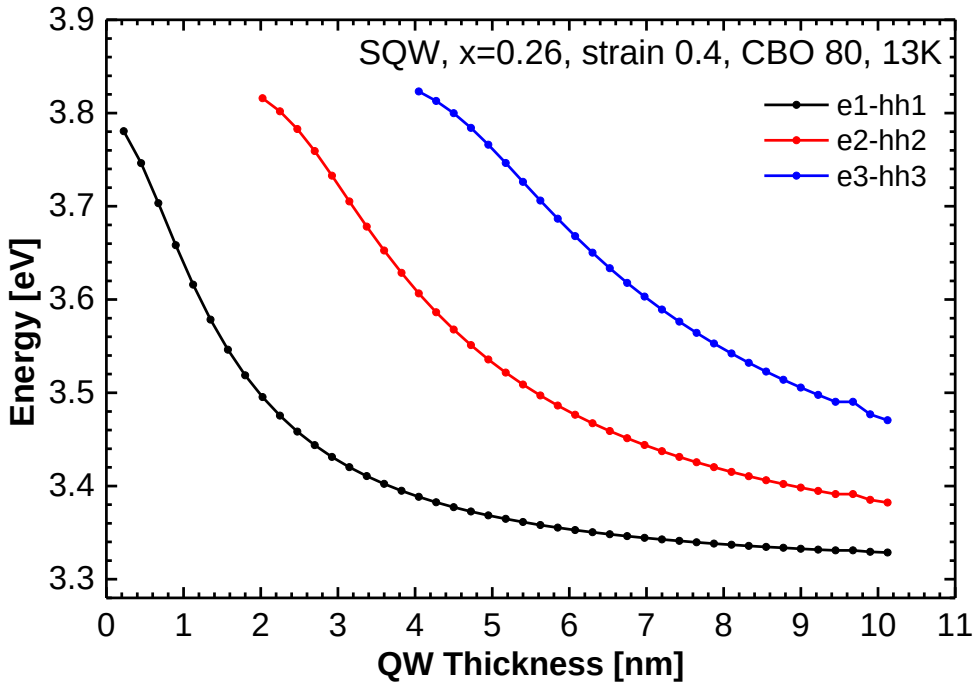

Figure 4.16 Transition energies of the 3 electron levels with the 3 heavy hole levels for the SQW with c-GaN QW and $Al_xGa_{1-x}N$ barriers (x = 0.26).

The strain changes for different Al content. For higher Al content the degree of relaxation increases (see Table 4.2).

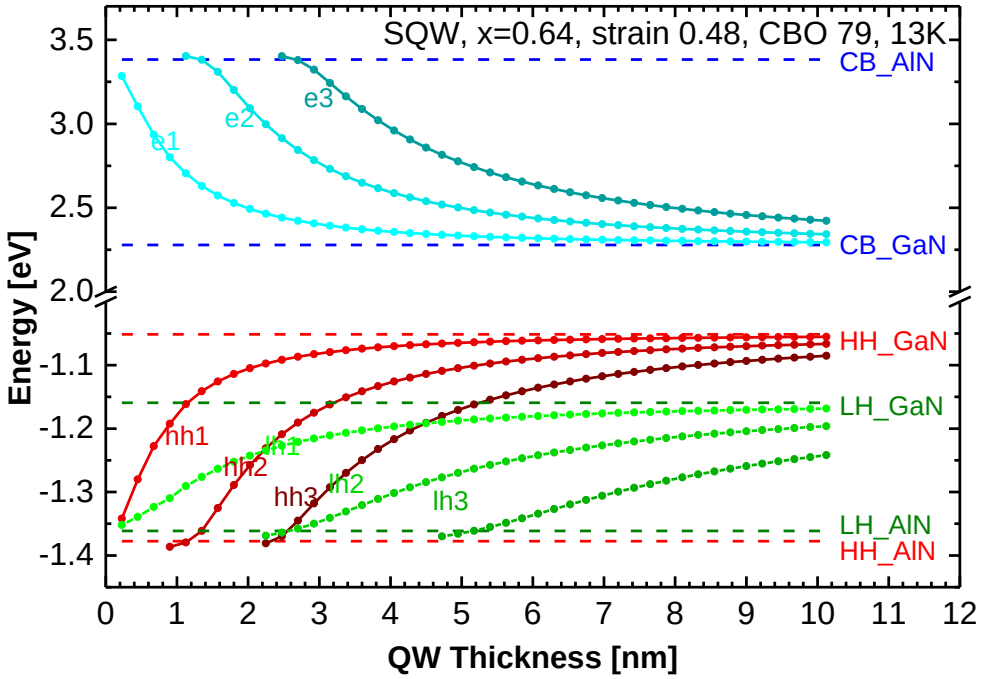

Figure 4.17 Simulated energy levels for electrons (e), heavy holes (hh) and light holes (lh) of a single c-GaN QW with $Al_xGa_{1-x}N$ barriers (x = 0.64) partly strained on c-GaN buffer at 13 K.

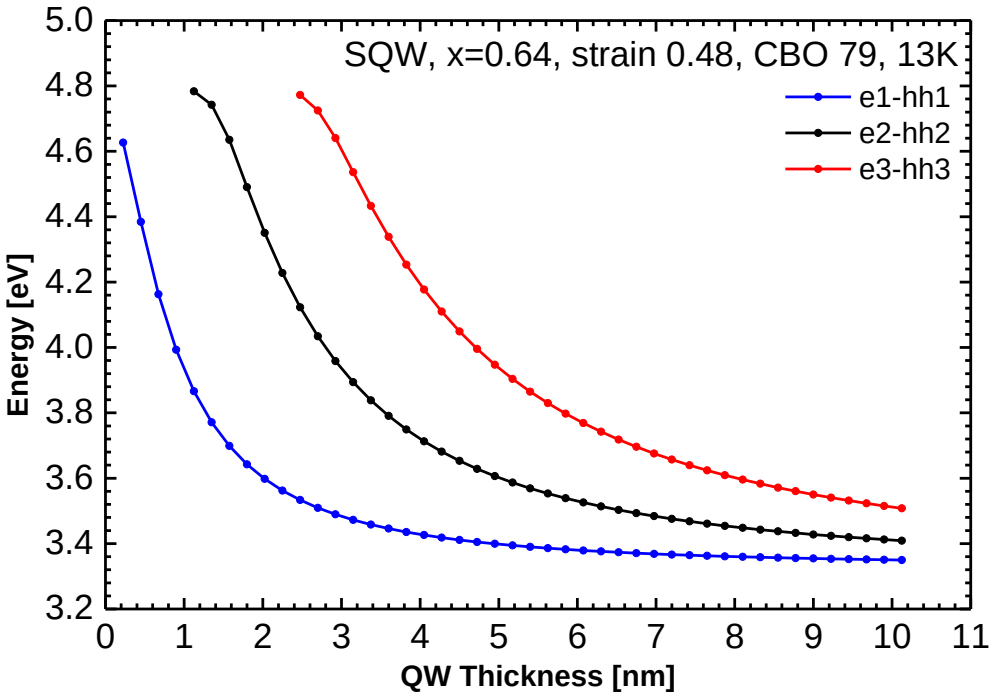

Figure 4.18 Transition energies of the 3 electron levels with the 3 heavy hole levels for the SQW with c-GaN QW and $Al_xGa_{1-x}N$ barriers (x = 0.64).

4.3.3 Time-resolved Investigation of Carrier Transfer

For the time-resolved measurements of series 0.64, the luminescence signal was analysed with a subtractive double monochromator (McPherson 2035 - 0.35 m focal length, 2400 g/mm, 300 nm blaze) and a single photon-detection was achieved with a multichannel-plate (MCP) photomultiplier tube (Hamamatsu R3809U-52).

For evaluation of the data a convolution routine has to been done, in order to extract the contribution of the temporal response of the setup and to identify the signal of the sample. For this reason a convoluted fitting approach [78] was applied to the data. In Figure 4.19 a time transient for the ADQW of series 0.64 with the barrier thickness d = 15 nm is shown. This time transient was determined at the emission wavelength for the wide QW (2.5 nm) at 7 K. The red curve is a fit function using a commercial software called Fluofit (Picoquant, GmbH) exploiting deconvolution of the laser emission characteristic $I_{source}(t')$ with the sample emission characteristic.

The experimental data are plotted as dots, the blue curve corresponds to the time transient $I_{source}(t')$ of the laser source and the red curve is the fit curve I(t) as described in the following formula.

A common approach for such experimental data is a bi-exponential fit.

$$I(t) = \int_{-\infty}^{t} I_{source}(t') \left(A_{fast} e^{-\frac{t-t'}{\tau_{fast}}} + A_{slow} e^{-\frac{t-t'}{\tau_{slow}}} \right) dt' \qquad (4.2)$$

The time transients of the emission for the 3 ADQW samples of series 0.64 are shown in Figure 4.20 for the QW_W (left) and for the QW_N (right). There is one fast decay time τ_{fast} (63 ps – 215 ps) and a slow component τ_{slow} (406 ps – 557 ps). Besides the peak areas A_{fast} (640 – 3717 counts) and A_{slow} (130 – 1251 counts) correspond to the intensity of the two exponential functions.

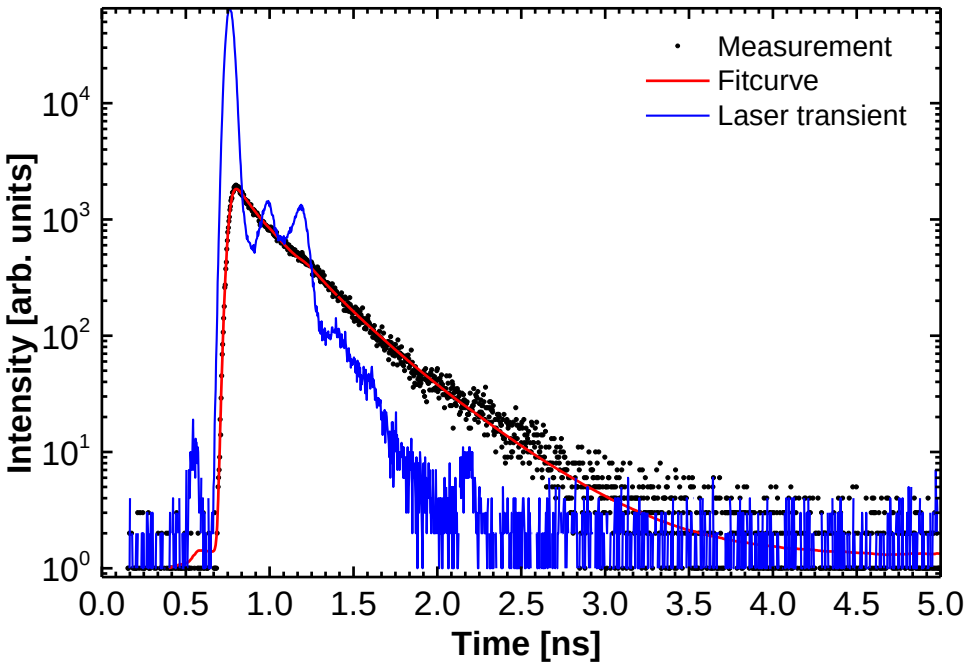

Figure 4.19 Time transients for the ADQW of series 0.64 with the thickest barrier d = 15 nm measured at the QW_W (2.5 nm) emission at 7 K. A bi-exponential fit was used with a convolution approach to match the data. (measured in TU Berlin together with Gordon Callsen)

The physical reason for the bi-exponential transient observed in our samples is up to now unidentified. In literature different explanations are discussed and are mentioned below. There are several papers describing also one fast and one slow time decay in AlGaAs/GaAs structures with an applied electric field. The explanations cover phonon-assisted tunnelling and impurity-/defect-assisted tunnelling [79][80]. Furthermore the valence band mixing of hh and lh is supposed to influence the tunnelling process [80] [81]. In addition, it is claimed, that exciton tunnelling times are much longer than the tunnelling times of individual electrons and holes causing two different decay times [80] [81].

Another approach is to distinguish between direct excitons and indirect excitons (also called crossed excitons) in multi quantum well structures. Due to the tunnelling process some of the direct excitons become crossed excitons. These are excitons where electron and hole are in different QWs and thus separated by the barrier. The binding energies of crossed excitons are considerably smaller leading to a much lower recombination probability [81] [82]. Finally experiments with hydrostatic pressure indicated the participation of Γ-X scattering in the fast decay time and the X-X scattering in the slow decay time [83]. These two decay times have also been reported for other material systems. For example in an investigation on CdTe/(Cd,Zn)Te ADQWs they explain the slow decay time with the process where the QWs get into thermal equilibrium after excitation [84]. As well as in InGaN/GaN double QWs the slow component may be caused by impurity related transitions [85][86].

The intensity influence of the slow component is much smaller than for the fast component. Thus in the following we focus mainly on the fast component.

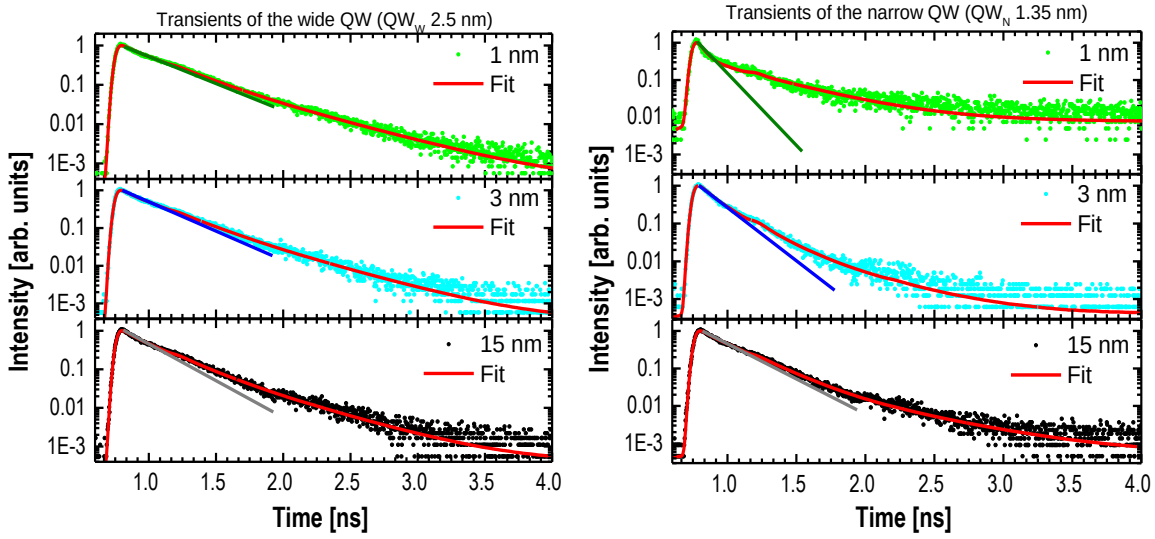

Figure 4.20 Time transients for the 3 ADQW samples of series 0.64 measured at the QW_W (2.5 nm, left) emission and at the QW_N (1.35 nm, right) emission for the three samples with different barrier thickness d. (measured in TU Berlin together with Gordon Callsen)

The dependency of the fast decay times on the barrier thickness can be seen in Figure 4.21. For thinner barriers the charge carriers of the narrow QW tunnel into the wide QW, thus the PL intensity of the narrow QW decreases faster. In addition these carriers cause more luminescence in the wide QW and the time decay gets slower. This hints the existence of coupling.

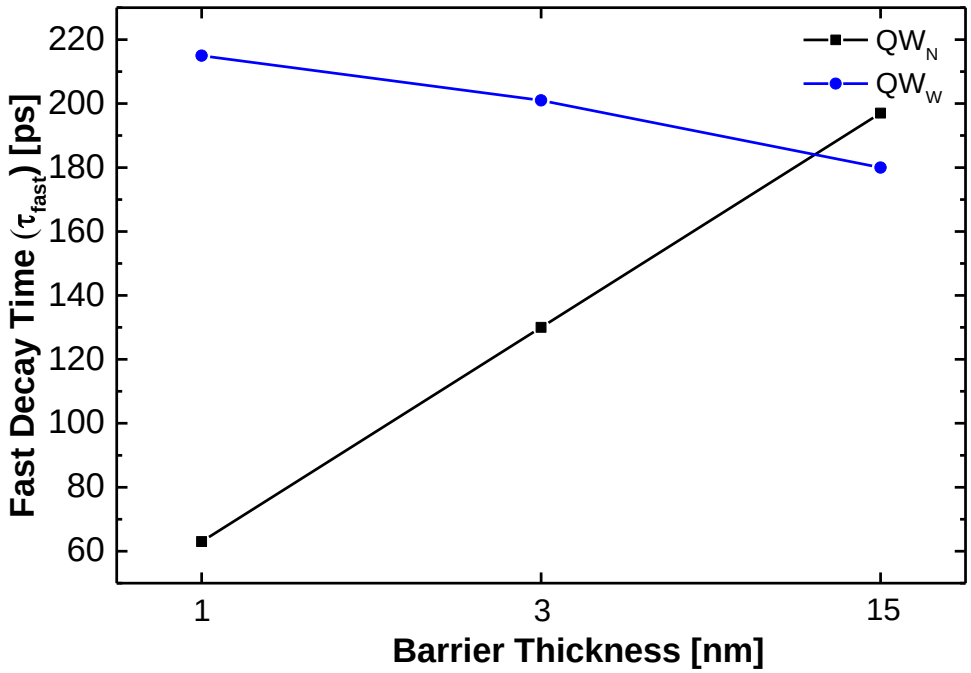

Figure 4.21 Decay time τ_{fast} of the QW_N (black) and QW_W (blue) emission corresponding to the barrier thickness d for low temperatures (7 K). The decay time increases for the wide QW due to additional electrons of the narrow QW for thinner barriers. The opposite behaviour takes place for the narrow QW. (evaluation done by me)

4.3.4 Excited Energy Levels

For an investigation of the excited energy levels an asymmetric cubic GaN/$Al_xGa_{1-x}N$ double quantum well with an Al content of x = 0.25 ± 0.03 was grown. The separating barrier between a wide (3.15 nm thickness) quantum well (QW_W) and a narrow (0.9 nm thickness) quantum well (QW_N) is 15 nm thick. Hence, these quantum wells can be considered to be uncoupled [12]. Nevertheless this sample can be used as a starting point for further considerations with coupled QWs. The ADQW structure is placed in between two 50 nm thick cubic $Al_{0.25}Ga_{0.75}N$ layers. The entire sample structure is depicted in Figure 4.22.

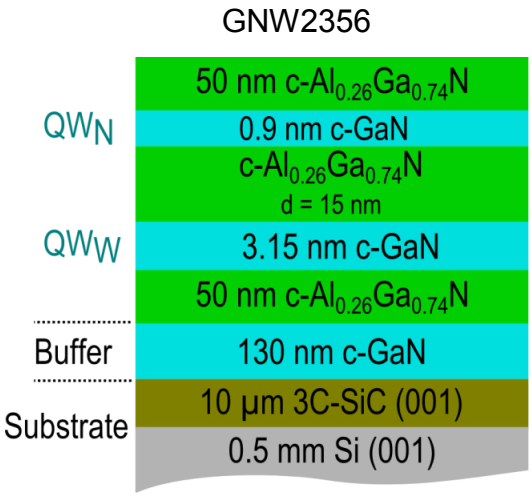

Figure 4.22 Sample structure of the cubic GaN/$Al_{0.25}Ga_{0.75}N$ ADQW. The barrier thickness between the two QWs is 15 nm, thus the wells are uncoupled.

The PLE spectra are measured at different detection wavelengths matching the emission maxima provided by PL (red for the QW_W, green for the QW_N, blue for the $Al_{0.25}Ga_{0.75}N$ barrier). The blue curve related to the emission maximum of the $Al_xGa_{1-x}N$ barriers show no additional transition except the band to band transition. The green curve for the narrow QW was compared with ellipsometry data of bulk $Al_xGa_{1-x}N$ [90]. In these ellipsometry data only the band edge of $Al_xGa_{1-x}N$ was measured, because there was no QW in the layer. This comparison revealed no additional feature, thus we expect there is no QW related transition visible in the green curve. The step visible in all PLE spectra at around 3.9 eV is caused by the band to band transition in bulk $Al_xGa_{1-x}N$ as also observed in [90] via absorption measurements at room temperature. In contrast, the PLE spectrum of the QW_W shows additional spectral features at lower excitation energies as analysed in the following.

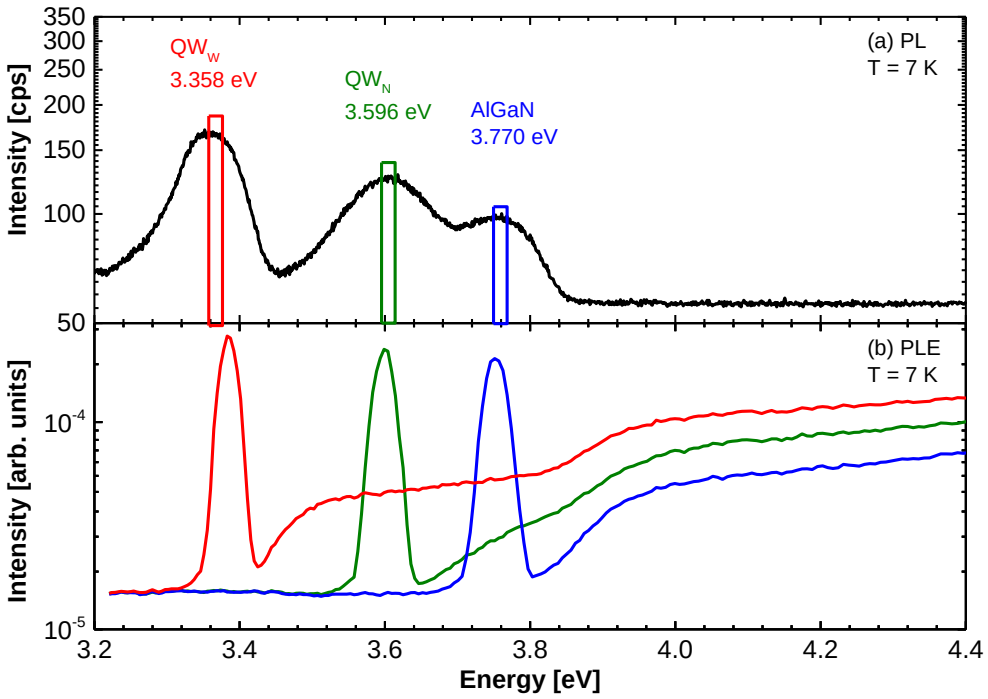

Figure 4.23 (a) Semi-logarithmic plot of the low temperature photoluminescence (PL) spectrum of the cubic GaN/$Al_{0.25}Ga_{0.75}N$ ADQW at a temperature (T) of 7 K. The depicted rectangles illustrate the applied spectral window for the detection of the PLE measurements. (b) Furthermore, photoluminescence excitation (PLE) data for three different detection wavelengths with T = 7 K are shown, which correspond to the emission maxima of the PL spectrum (red for the QW_W, green for the QW_N, blue for the $Al_{0.25}Ga_{0.75}N$ barrier). (measured in TU Berlin together with Gordon Callsen)

Figure 4.24 depicts the PLE spectrum detected at the maximum emission of the QW_W. The narrow peak at 3.38 eV is caused from an overlay of the excitation light and resonant sample luminescence, thus this part of the spectrum is neglected in our evaluation. Although the simulations predict 5 allowed transitions, only two can be identified. The low energy transition occurs between the first electron level (e1) and the third heavy hole level (hh3) at 3.51 eV. The high energy one can be assigned to the second electron level (e2) and the second heavy hole (hh2) transition at 3.63 eV. The interface roughness leads to a broadening of the transition. This is more significant for higher energy levels, because the influence of QW thickness variation is stronger for a smaller energy separation of the bound energy level to the potential barrier (as is described in chapter 4.4.6). As an approximation the intensity is fitted exploiting two Gaussian functions with an error function to take into account the step behaviour of the 2D density of states. In order to distinguish between the $Al_xGa_{1-x}N$ emission and the QW transitions the green curve used as background for the fit is the PLE spectra of the QW_N. The two QWs are uncoupled. Therefore the

transitions cannot be assigned to the transition of the QW_N, although the energy is similar with 3.63 eV. The step at around 3.9 eV is a characteristic of band to band transitions in $Al_xGa_{1-x}N$, which was also measured in ellipsometry measurements of bulk $Al_xGa_{1-x}N$ [90].

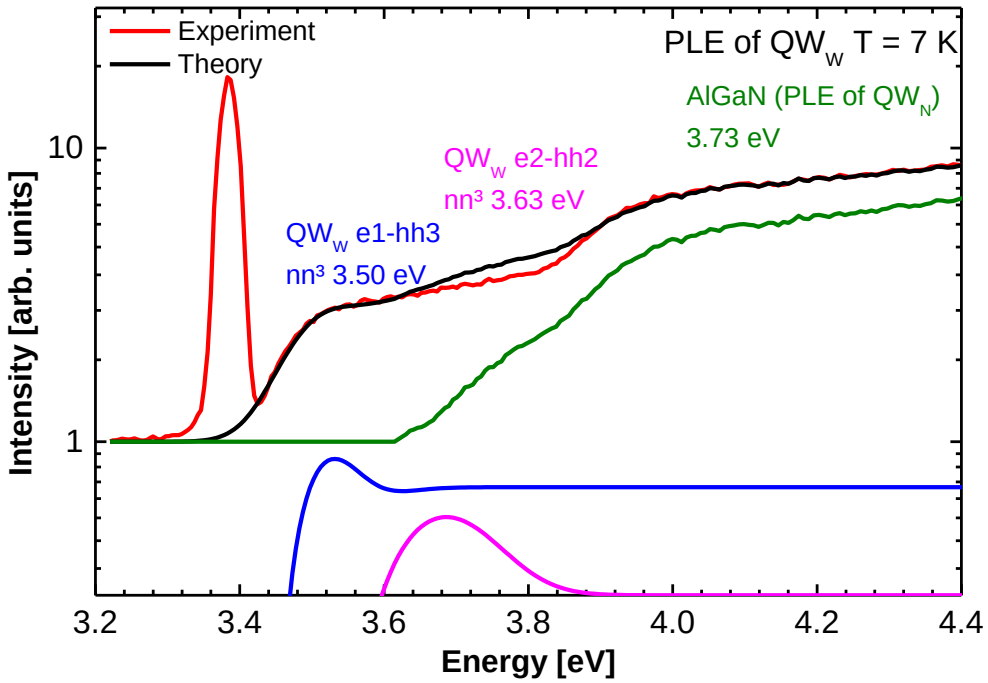

Figure 4.24 Detailed, semi-logarithmic plot of the low temperature photoluminescence excitation (PLE) spectrum detected at the emission maximum of the wide quantum well (QW_W) at a temperature (T) of 7 K. The narrow peak at 3.38 eV originates from an overlay of the excitation light and resonant sample luminescence. Furthermore, two transitions can be verified (e1-hh3 and e2-hh2) by a careful fitting routine. (measured in TU Berlin together with Gordon Callsen)

Due to the complexity of the band structure and the several energy levels for electrons (e), heavy holes (hh) and light holes (lh) a detailed simulation of the sample is needed, in order to evaluate the experimental data. These simulations were done with nextnano³ providing a good match with the experimental data for a 0.9 nm and 3.15 nm QW at 7 K. Details concerning the used nextnano³ inputs are explained in chapter 5.1. In the nextnano³ calculations excitonic effects are neglected, thus a separate calculation was done analogue to the theory chapter. The different masses of lh and hh affect the excitonic binding energies. In case of an exciton (X), which is formed by an e and hh ($X_{e\text{-}hh}$) or e and lh ($X_{e\text{-}lh}$) the binding energy is different. In addition, the effective mass $m^*(\epsilon)$ is energy dependent, leading to different

values for excited energy levels. Thus the binding energy is also energy dependent, which is taken into account using a modified Kane formula [9] [87] [88]

$$\frac{m_0}{m^*(\epsilon)} = 1 + 2F + \frac{E_p}{3}\left(\frac{2}{E_g+\epsilon} + \frac{1}{E_g+\Delta_{so}+\epsilon}\right) \quad (4.3)$$

With the confinement energy ϵ, the interband matrix element for cubic GaN $E_p = 16.86\,eV$ [9] [89], a coupling constant of remote bands F, and the spin-orbit splitting of the valence band $\Delta_{so} = 15\,meV$. The value for F is estimated in order to reach the bulk value for zero confinement ($\epsilon = 0$). F is different for electron ($F_e = -0{,}48$), heavy hole ($F_{hh} = -2{,}50$) and light hole ($F_{lh} = -1{,}32$).

The calculated binding energies are summarised in Table 4.4. Furthermore in Table 4.5 the theoretical transitions are compared with the data provided by the optical experiments.

Table 4.4 Summary of the excitonic binding energies (E_b) for the two QWs. Due to different effective masses of light hole (lh) and heavy hole (hh) the excitonic binding energy change if the electron (e) interacts with an hh ($X_{e\text{-}hh}$) or lh ($X_{e\text{-}lh}$). The energy dependence of the effective mass is considered by a modified Kane formula. (evaluation done by me)

QW thickness [nm]	E_b for $X_{e1\text{-}hh1}$ [meV]	E_b for $X_{e2\text{-}hh2}$ [meV]	E_b for $X_{e1\text{-}hh3}$ [meV]	E_b for $X_{e1\text{-}lh1}$ [meV]	E_b for $X_{e2\text{-}lh2}$ [meV]
3.15	35	36	26	31	25
0.9	36			30	

Table 4.5 Overview of the theoretic expected transition energies and the fit curve maxima in the PLE and PL spectra. The excitonic binding energies (see Table 4.4) are included in this comparison.

	Transition	Theory [eV]	PLE [eV]	PL [eV]
QW_W	**e1-hh1**	3.39		3.36
	e1-hh3	3.48	3.51	
	e2-hh2	3.68	3.63	
QW_N	**e1-hh1**	3.62		3.59
	e1-lh1	3.67		

Due to the thick $Al_xGa_{1-x}N$ barrier (15 nm) the QWs can be investigated and simulated independently. In Figure 4.25 and Figure 4.26 the conduction band edge (blue line) and the valence band edges are plotted vs. the position along the growth direction for the QW_W and the QW_N The residual strain in the QW structures lead to a

difference in the band gaps for hh and lh. This inflicts also the energy levels for hh and lh diverge regarding to the unstrained QW (red for hh, green for lh).

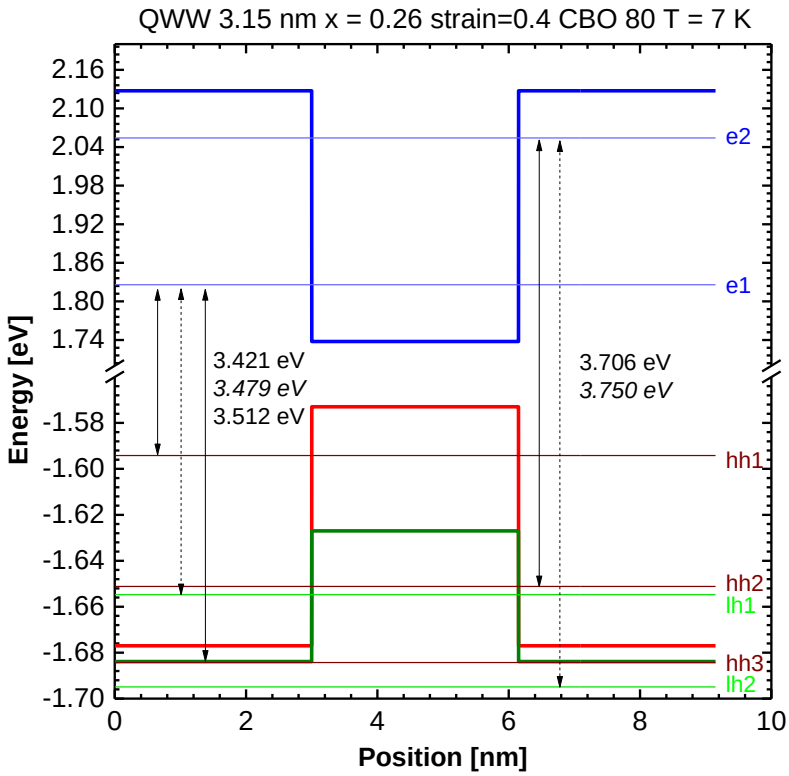

Figure 4.25 Nextnano³ simulation of the energy levels and the band edges for the wide QW (3.15 nm) at 7 K. Two bound energy levels exist for the electrons (e), whereas the holes have five bound states, three for the heavy holes (hh) and two for the light holes (lh). This leads to 5 allowed transition.

Furthermore, the bound energy levels for e, hh, and lh are plotted as dashed lines. These simulations provide a prediction of the allowed transitions. There are five allowed transitions for the wide QW and two for the narrow QW. The hh3 and lh2 energy levels in the wide QW seem to be unbound, because the results directly from nextnano³ do not consider excitonic effects. In order to provide a correct description also the excitonic binding energy and the energy dependency of the effective masses has to be taken into account (see Table 4.4, Table 4.5). Thus these two levels are bound.

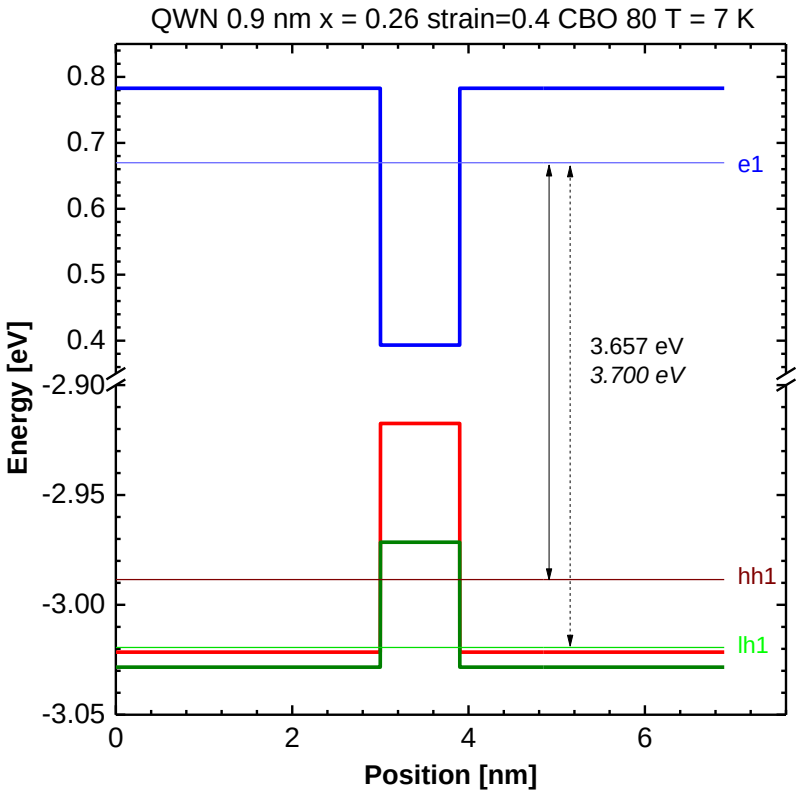

Figure 4.26 Simulation results via nextnano³ of the energy levels and the band edges of the narrow QW (0.9 nm) for 7 K. There is one bound energy level for every charge carrier (electrons (e), heavy holes (hh) and light holes (lh)). Thus two allowed transitions are predicted.

The low temperature optical measurements are shown in Figure 4.23. The upper part depicts a PL spectrum and the lower part depicts the three PLE spectra. In the PL spectrum three clearly distinguishable emission bands can be observed at 3.358 eV, 3.596 eV, and 3.770 eV and are associated to the wide QW_W, the narrow QW_N, and the cubic $Al_{0.25}Ga_{0.75}N$.

4.3.5 Summary ADQWs

In this chapter two series of asymmetric double quantum wells (ADQWs) have been analysed in order to achieve a complete theoretical understanding of the energy structure and the coupling between the two quantum wells (QW). For this reason several photoluminescence (PL) measurements have been performed to investigate the influence of the barrier thickness to the coupling between the two QWs. Although the series have different Al content (0.26 and 0.64) the general behaviour in the PL spectra is very similar. The higher Al content in the series 0.64 cause a lower tunnelling rate leading to a significant coupling at a thinner barrier (3 nm) compared to the series 0.26 where the coupling starts at 7 nm thick barriers. For the evaluation time-resolved PL was used to determine the decay times needed for rate equations as well as simulations of the energy levels in the QWs via nextnano³. In addition, photoluminescence excitation spectroscopy (PLE) was used to determine higher transitions (e1-hh3 and e2-hh2) which cannot be measured by PL. This is very important to confirm the parameters used for the nextnano³ simulations, because for higher energy levels the conduction band valence band offset (CBO:VBO) gets more important.

The theoretical considerations presented in this chapter fit very well with the experimental data, thus the parameter set is consistent and can be applied to more complex heterostructures.

4.4 Multi Quantum Wells (MQW)

The experimental and theoretical knowledge gained with the ADQWs was used for the design of the MQW samples. Especially the influence on the IR absorption FWHM and intensity was in the focus of interest. The intersubband transitions (ISBT) can be used to investigate nonlinear effects, due to their high nonlinear properties. Besides the influence of parameters like doping, period number and substrates on the FWHM in ISBT have been investigated. Furthermore such MQWs can be used for quantum cascade lasers (QCL).

This chapter is divided in different parts. At first general information about the growth of the MQW samples is described briefly followed by an investigation of the real layer thicknesses of one MQW sample via TEM [11]. This layer thickness is crucial for the exact simulation of the energy levels via nextnano³. Then HRXRD measurements showed the existence of additional SL peaks, which is the proof for the formation of a SL structure. Besides the photoluminescence (PL) spectra revealed very similar emission bands providing the good reproducibility of the QW layer thicknesses. The IR absorption data revealed a FWHM of 370 meV for the MQW with 80 periods and 250 meV for the MQW with 40 periods. The difference is caused by an unexpected high doping of the first sample and the higher period number. A detailed theoretical modelling of the FWHM in the IR absorption revealed the high significance of the interface roughnesses. The last sub-chapter deals with one of the first non-linear measurements on MQWs based on the cubic phase of the group III-nitrides. These first experimental data present a third order susceptibility in the order of $\mathrm{Im}\,\chi^{(3)} \sim 1.1 \cdot 10^{-20}\ \mathrm{m}^2/\mathrm{V}^2$ as described in [10].

4.4.1 Growth of MQW Samples

Cubic GaN/AlN MQWs were grown on a 100 nm c-GaN buffer layer, which was deposited on a 10 µm 3C-SiC (001) layer on top of a 0.5 mm thick Si substrate. For these samples 80 and 40 periods of GaN QWs were grown separated by 1 nm wide AlN barriers (see Figure 4.27).

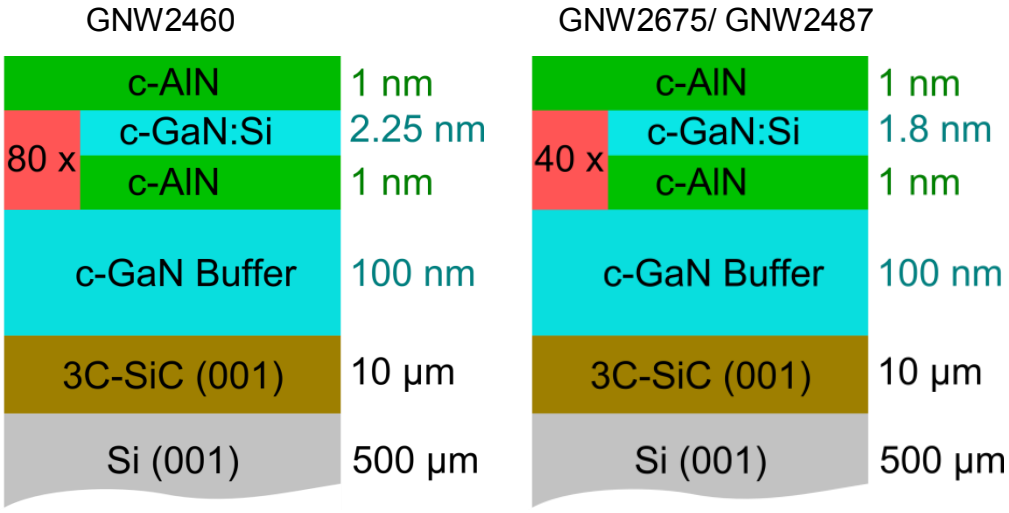

Figure 4.27 Sample structure of two different types of MQW with 80 periods (left) and 40 periods (right) of GaN QWs and 1 nm AlN barriers and a homogeneous Si doping in the c-GaN QWs in the order of $N_{Si} \sim 10^{19}$ cm^{-3}.

The growth of the MQW samples was initiated with a GaN buffer layer, which was started by a growth process of 20 s GaN growth with 30 s growth interruption with 10 cycles at a substrate temperature of T_S = 720 °C. Prior each GaN growth 1 Monolayer Ga was deposited (7 s Ga without N). After 100 nm GaN the first AlN barrier for the MQW was started, by opening Al and N simultaneously at a substrate temperature of T_S = 730 °C. For all the c-GaN QWs the substrate temperature was decreased to T_S = 720 °C. In Figure 4.29 the RHEED intensity profile of the central spot (red area in Figure 4.28) during the growth of the first QW and second AlN layer is shown. Before each GaN QW layer 7 s of Ga was deposited. Then the N shutter was opened for 7 s and GaN was formed. At this time the Si shutter was opened. After the QW a growth interruption of 60 s was followed by the second AlN layer. At the end of the AlN layers another growth interruption of 40 s was done. The growth interruptions are needed to evaporate excess Ga and lead to a smoother surface for GaN and AlN. All 80 periods have been grown similar.

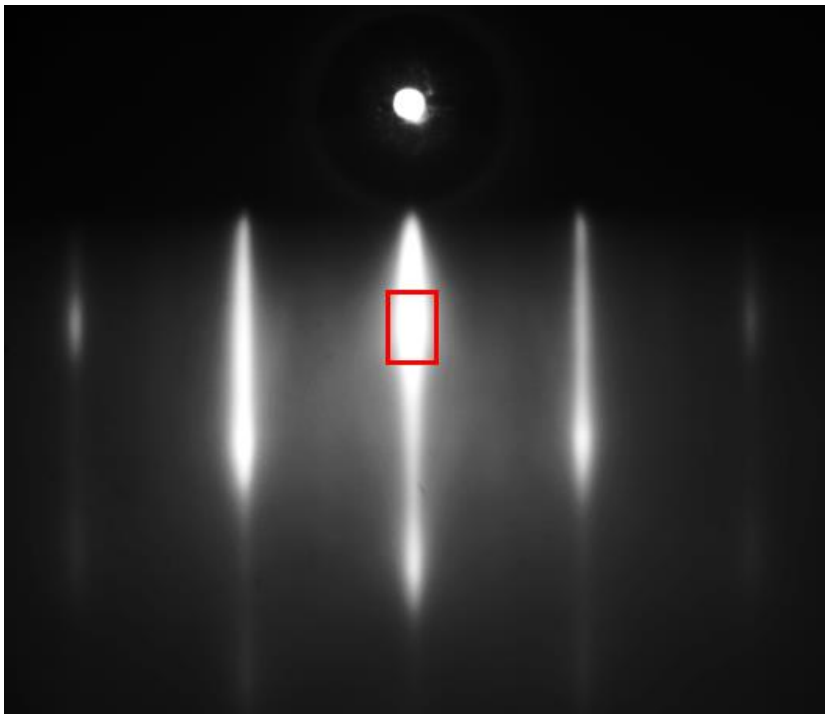

Figure 4.28 RHEED diffraction pattern taken after the first MQW cycle of sample GNW2460.

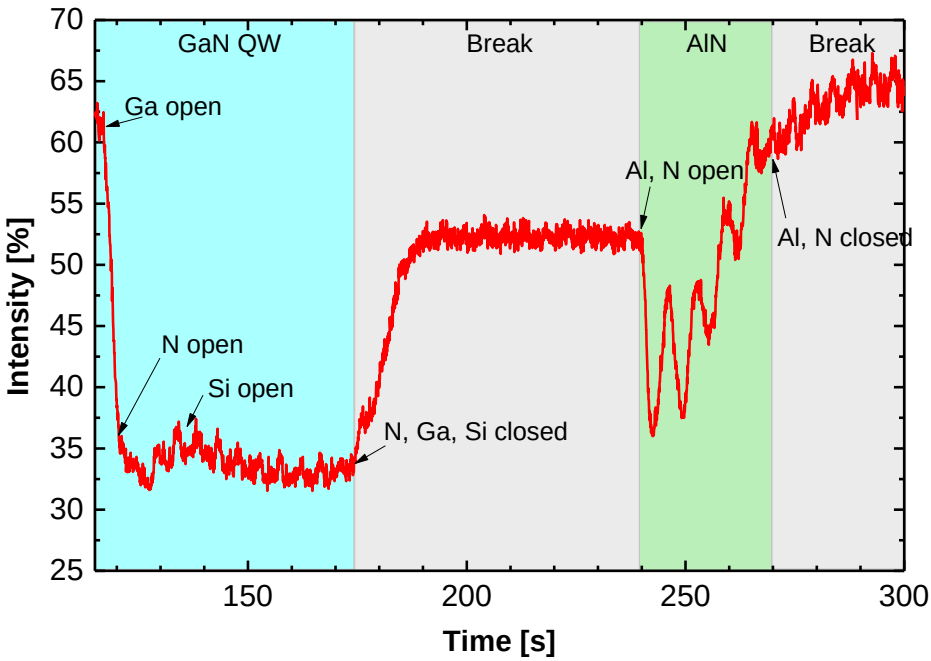

Figure 4.29 RHEED intensity profile of the first QW and second AlN layer of the MQW structure (GNW2460) measured in the red area in Figure 4.28.

In all MQWs a homogeneous doping of the c-GaN QWs with Si in the order of $N_{Si} \sim 10^{18}$ -10^{19} cm^{-3}) is intended, in order to shift the Fermi energy above the first electron level (e1). This is crucial for the absorption measurements. Only if there are electrons populating the first electron level, absorption between e1 and e2 can

be measured. The sample structures of the most important MQWs are shown in Figure 4.27. The main difference is the QW thickness and the period number. For GNW2460 the QW is 2.25 nm thick with 80 periods. In order to match the desired 1.55 µm in the IR absorption, the QWs of the other MQWs are 1.8 nm thick. Besides the period number of 40 is expected to be sufficient to achieve a good IR absorption and to decrease the FWHM in the absorption spectra.

4.4.2 Investigation of MQWs by HRXRD

Similar to the ADQWs all MQW layers have been investigated via HRXRD. An average defect density of the order of $D \approx 2 \times 10^{10}\ cm^{-2}$ was obtained by measuring the width of the rocking curve of the (002) reflection of the MQW samples. Atomic force microscopy measurements revealed a surface roughness of 5-6 nm (rms) for 5x5 µm^2 areas.

By growing a MQW structure with several periods of AlN/GaN layers a superlattice (SL) is formed. This superlattice is characterised by an averaged lattice constant, which can be calculated by adding the AlN barrier thickness and the GaN QW thickness. Furthermore additional reflections are visible in the HRXRD, caused by this SL lattice constant. In Figure 4.30 the RSM around the (113) direction for GNW2460 with 80 periods (left) and GNW2687 with 40 periods (right) are shown. In both (113) RSM two additional reflections corresponding to the lattice constant of the superlattice can be seen, proving the existence of a superlattice. Thus the growth of the superlattice was successful on the structural level. Besides the RSM reveal a partial strain in the SL. A deviation in the reciprocal lattice constant parallel to the surface ($q_{||}$) of the additional SL peaks compared to the c-GaN and c-AlN is visible. This leads to partial strain in the QW and barrier materials, thus an averaged lattice constant is formed. The degree of relaxation of all MQWs measured in this thesis is $R = 0.25 \pm 0.04$, determined via the additional SL peaks visible in the RSM in (113).

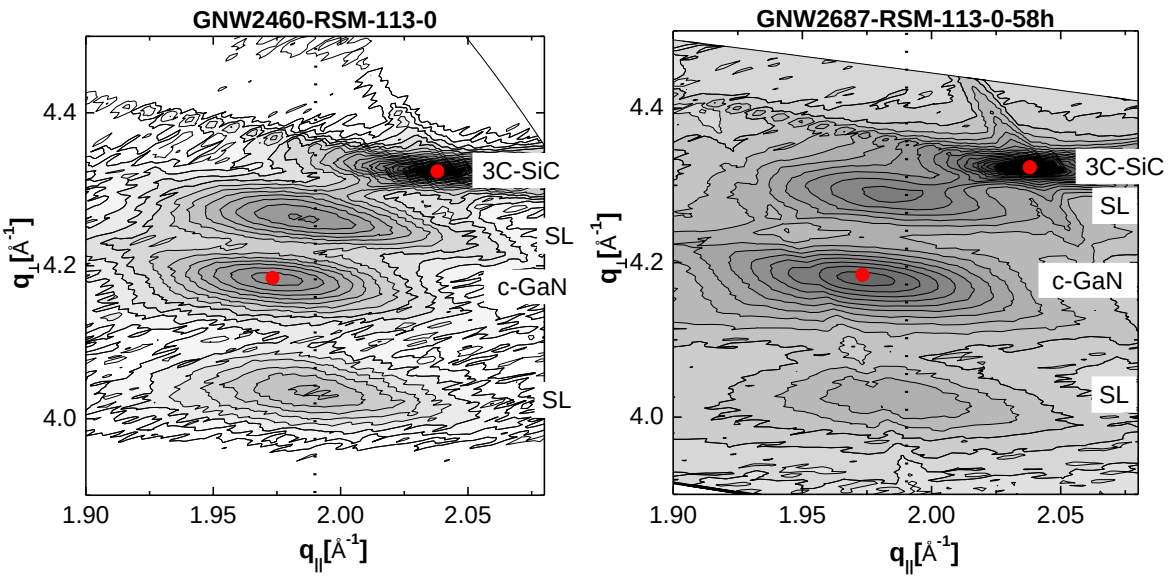

Figure 4.30 RSM in (113) direction of GaN/AlN MQW structures with 80 periods (left) and 40 periods (right).

In Figure 4.31 the RSM in (002) direction of the same MQWs are depicted. Although in the (113) direction two additional peaks occur in the (002) direction of the MQW with 40 periods (right) only one SL peak is visible. This is caused by the relatively high intensity of the 3C-SiC reflection and the SL peak is too weak to be detectable.

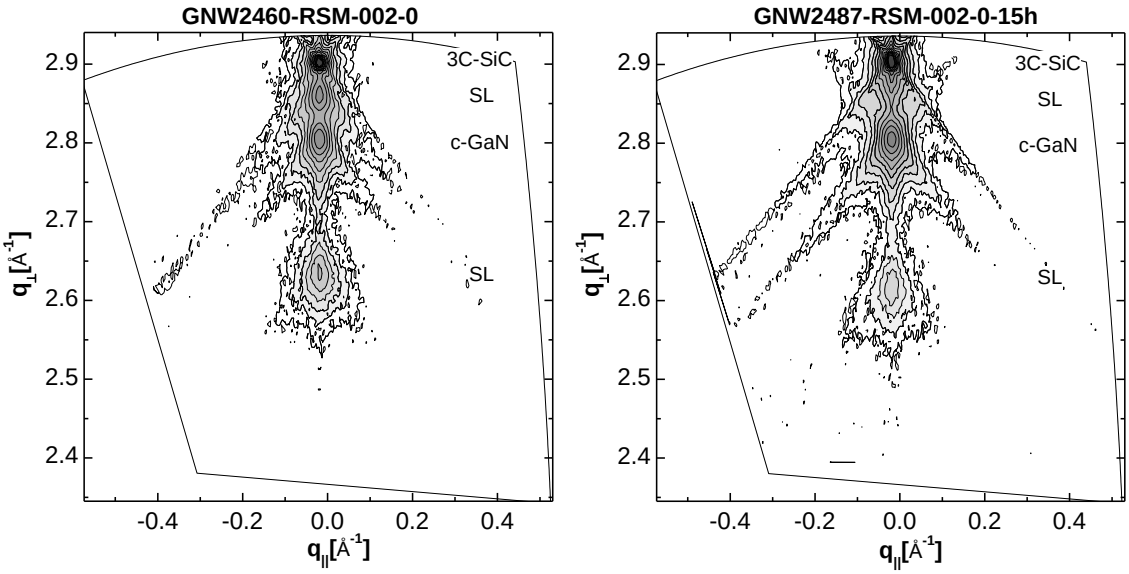

Figure 4.31 RSM in (002) direction of GaN/AlN MQW structures with 80 periods (left) and 40 periods (right).

4.4.3 Calibration of QW Thickness by TEM

The growth rate for c-GaN layer is estimated by growing a nominal 600 nm thick c-GaN sample. The real sample thickness is measured by reflection interference spectra leading to the growth rate. This procedure determines the growth speed of c-GaN on c-GaN without interface effects. But the growth speed strongly depends on the underlying material, leading to a deviation of the growth speed for complex heterostructures. In order to investigate the real thicknesses of the MQWs, Transmission electron microscopy (TEM) measurements were done by Torsten Rieger of AG Pawlis in FZ Jülich [11]. So a general calibration of the real QW thickness with the simulations and the optical transitions (nextnano³) can be achieved. A MQW sample with 20 periods of nominal 1.35 nm c-GaN QWs and 5 nm AlN barriers was deposited on a 100 nm thick c-GaN buffer layer on top of 3C-SiC/Si substrate (see Figure 4.32). The c-GaN QWs are homogeneous doped with Si in the order of $N_{Si} \sim 10^{19}$ cm^{-3}.

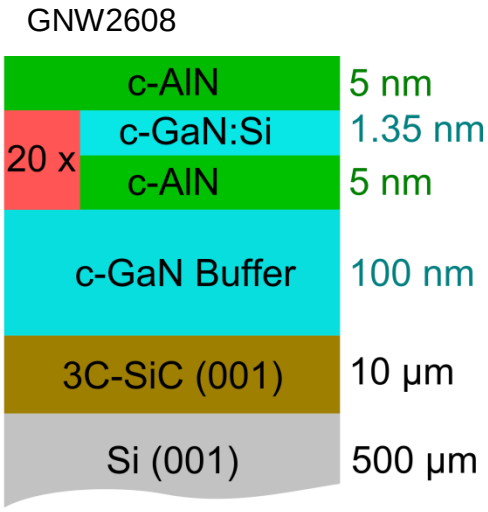

Figure 4.32 Sample structure of a MQW with 20 periods of 1.35 nm GaN QWs and 5 nm AlN barriers and a homogeneous Si doping in the c-GaN QWs in the order of $N_{Si} \sim 10^{19}$ cm^{-3}.

Cross-sectional high resolution TEM bright field images along the <110> direction (see Figure 4.33) are measured with a FEI Tecnai G² F20 microscope [91]. A TEM lamella was prepared by focused ion beam using Ga ions and a final polishing step with an acceleration voltage of 5 kV. In this diagram 5 c-AlN layers and 4 c-GaN QWs are visible. Furthermore in the lower left corner are some stacking fault (SF) measured.

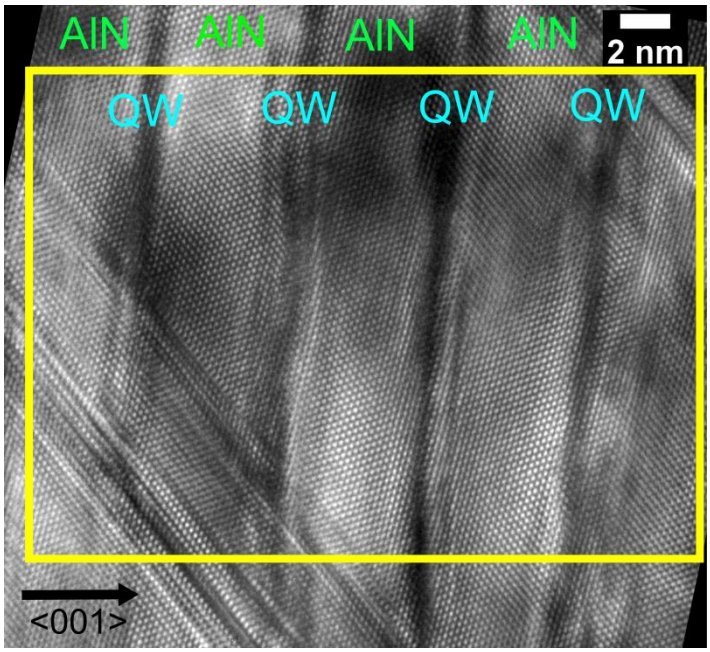

Figure 4.33 High resolution TEM micrograph of a MQW sample with 20 periods of 1.35 nm c-GaN and 5 nm AlN oriented along the <110> direction of the MQWs (measured in FZ Jülich together with Torsten Rieger)

In order to investigate the layer thicknesses, an intensity profile of the yellow area in Figure 4.33 was performed with a free software ImageJ. (ImageJ is a graphic software allowing an intensity profile of a grayscale image.) In this area several defects and thickness fluctuations are visible, leading to a strong noise in the intensity. Thus several line profiles in this area are averaged to reduce the noise. The result of this averaged profile is shown in Figure 4.34. Furthermore a mean value for the intensity of the AlN barrier was used (visible as blue lines in Figure 4.33). The criterion for the calculated thicknesses is the point at which the intensity between the AlN and GaN layers has dropped to the half value (crosses in Figure 4.33). This leads to a medial width of (1.2 ± 0.1) nm for the GaN QWs and (4.77 ± 0.46) nm for the AlN barriers. There couldn't be a layer thickness between 1.125 nm (5 ML) and 1.35 nm (6 ML), because a monolayer (ML) of c-GaN is 0.225 nm thick and this is the smallest possible thickness. Thus for the GaN QWs a layer thickness of 1.125 nm (5 ML) or 1.35 nm (6 ML) are expected. These two different layer thicknesses lead to the average width of (1.2 ± 0.1) nm. The best match of the QW layer thickness with the linear optical measurements exploiting nextnano³ is 1.35 nm.

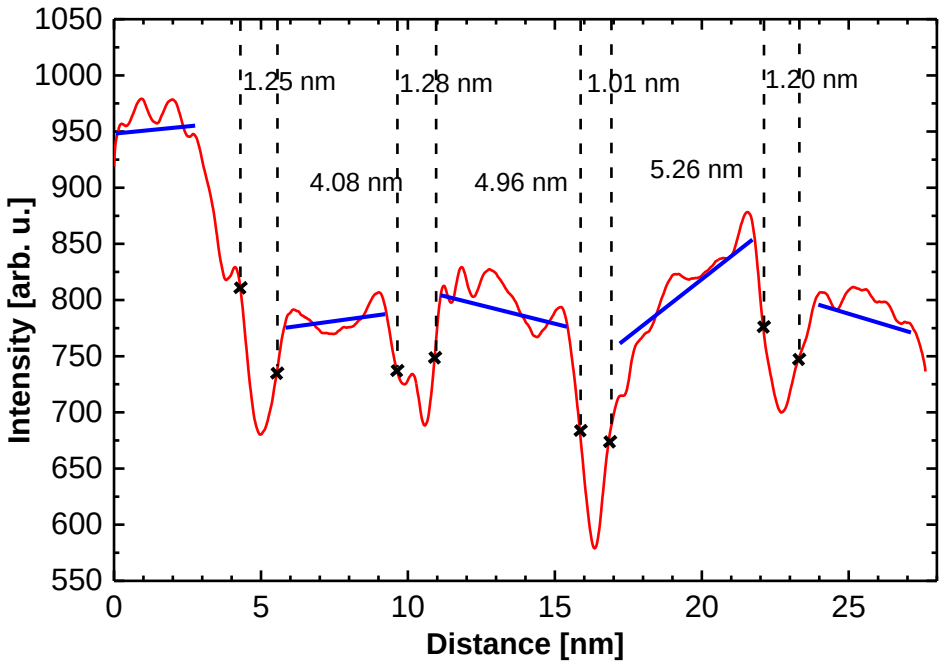

Figure 4.34 TEM intensity contrast profile averaged over the yellow area in Figure 4.33. The medial QW thickness is (1.2 ± 0.1) nm and the medial thickness for the AlN barriers is (4.77 ± 0.46) nm. (the evaluation done by me)

4.4.4 Photoluminescence Spectroscopy (PL)

In the following the most important parameters of the used substrates and the grown samples will be compared via photoluminescence spectroscopy. All the substrates referred to in this chapter have very similar roughness (0.6 – 0.8 nm) and FWHM of ω-scans in (002) (5 - 7 arcmin). Furthermore the samples show also similar roughness (3 - 5 nm) and FWHM in HRXRD (44-46 arcmin) (see Table 4.6). In Figure 4.35 the room temperature PL spectra of 3 different MQW samples with equal doping of $N_{Si} = 10^{19}$ cm^{-3} grown on different substrates are shown. The doping is always done homogenous in the QWs. All the spectra are normalized in order to compare the emission energy and the FWHM. The difference in the emission energy between GNW2460 and GNW2675/GNW2687 was intended to adapt the IR absorption to 1.55 µm by growing thinner QWs. The similarities of GNW2675 and GNW2687 are a clear indication for the independency of the PL spectra in regard to the substrate.

Table 4.6 Overview of the important structural properties, like roughness and FWHM of ω-scans of the used substrates and the grown MQW samples.

Substrate	Roughness AFM [nm]	HRXRD [arcmin]	Sample numbers	Roughness AFM [nm]	HRXRD [arcmin]
UniPad1102	0.6	7.3	2460, 2486, 2487	5.3	45.7
14CO050	0.7	5.1	2675, 2729-32	4.1	44.1
14CO144	0.8	5.2	2684,2687	3.0	43.8

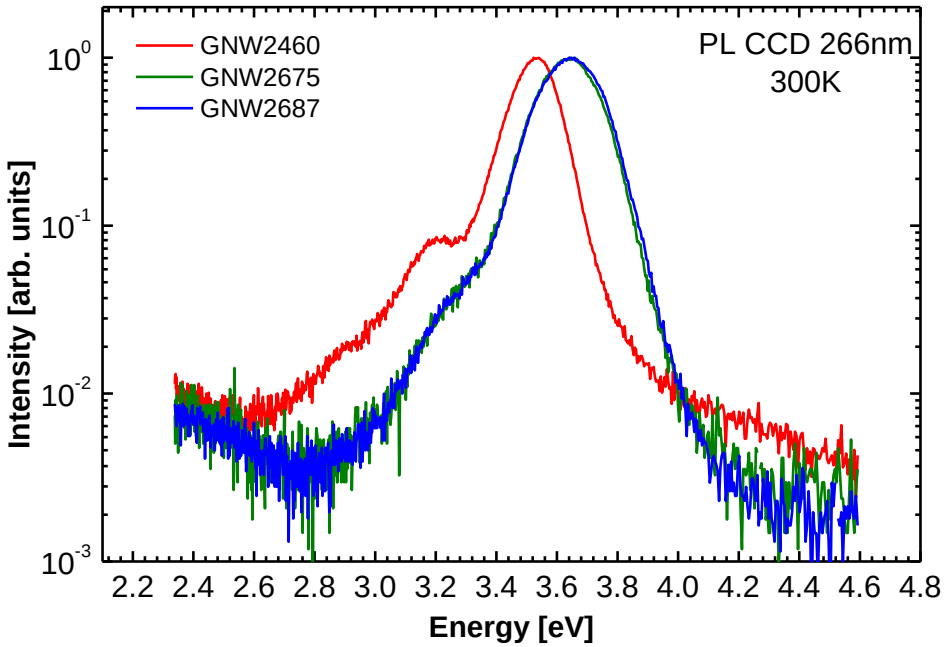

Figure 4.35 PL spectra of MQW with 80 periods (red) and 40 periods (green, blue) grown on different substrates.

There is no significant influence of the number of periods on the energy and FWHM of the emission, as can be seen in Figure 4.36. In this figure the three samples have 40, 50 and 60 periods, corresponding to GNW2675, GNW2732 and GNW2729, respectively. Nevertheless only GNW2460 and GNW2675 show IR absorption, but the PL data are also very similar in regard to the emission energy and the FWHM. Another parameter, which affects the IR absorption, is the doping density.

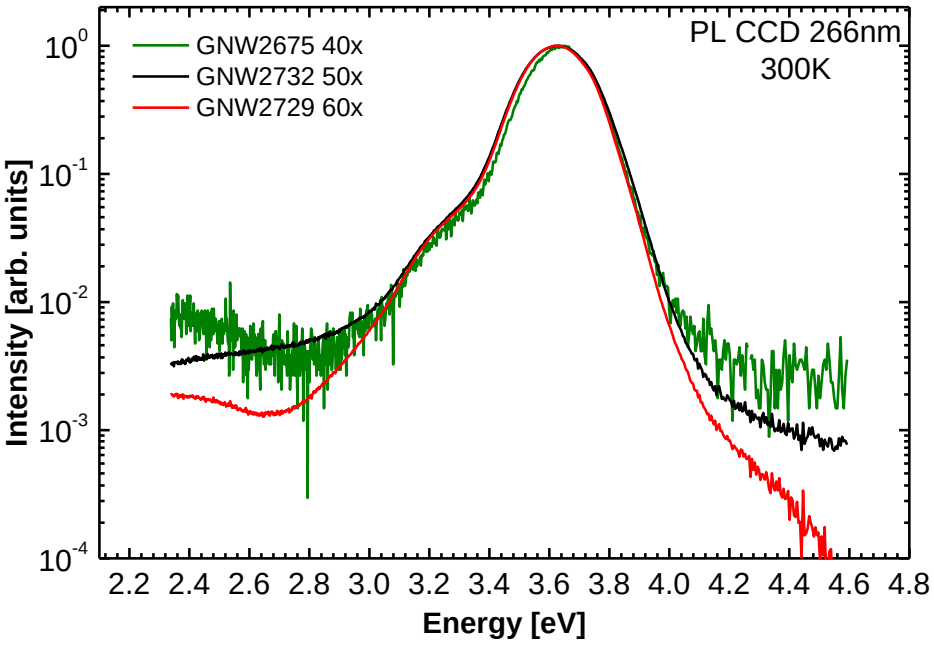

Figure 4.36 PL spectra of MQW with 40 (green), 50 (black) and 60 (red) periods of GaN/AlN. The spectrum of GNW2675 shows a higher noise, because of a lower integration time during the measurement.

In Figure 4.37 three spectra of samples with equal periods but different doping densities are shown. The sample GNW2675 has the lowest doping density with $N_{Si} = 10^{19}$ cm^{-3} and the sample GNW2731 has $N_{Si} = 2x10^{19}$ cm^{-3} and GNW2730 has $N_{Si} = 4x10^{19}$ cm^{-3}. The spectra are again very similar and only GNW2675 shows IR absorption.

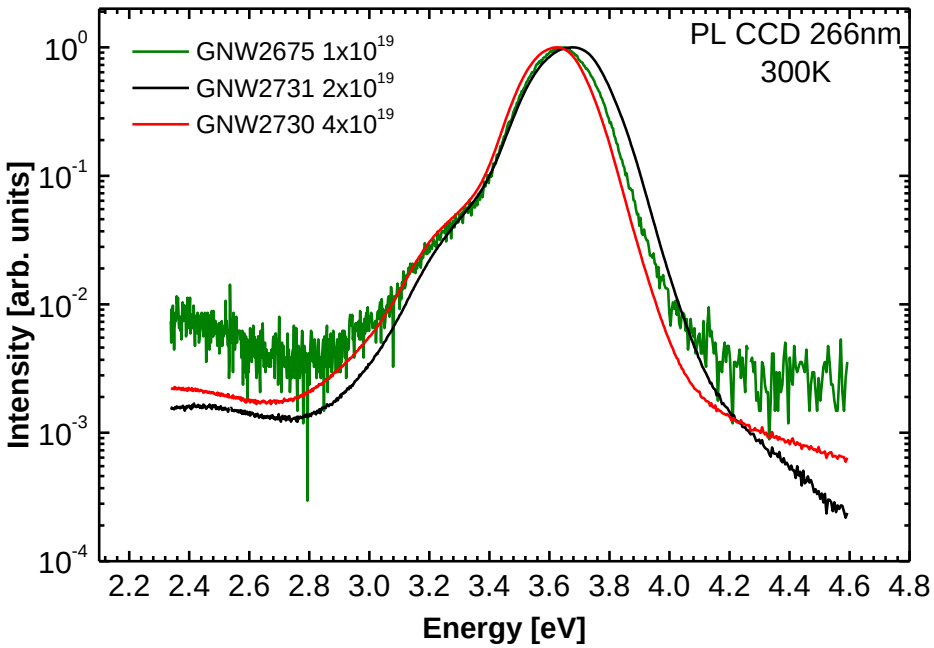

Figure 4.37 PL spectra of MQW with 40 periods and different doping. The spectrum of GNW2675 shows a higher noise, because of a lower integration time during the measurement.

4.4.5 Measurements of Intersubband Absorption

The absorption measurements of the intersubband transition (ISBT) are taken in TU Dortmund by AG Betz, but the evaluation of the data presented here was performed by me. More details about the sample processing can be seen in chapter 2.3 and 3.6. The incident light approaches perpendicular to the surface of the 30° facet. Due to the selection rules for ISBTs, the absorption is only expected for TM polarized excitation. In order to obtain the absorption spectrum the detected spectra for TM and TE excitation are subtracted for the MQW sample. Moreover, a reference sample of 600 nm c-GaN with equivalent 30° facets was used, to identify spectral features of the substrate and the c-GaN buffer layer contained in the absorption data. The spectra in Figure 4.38 are achieved subtracting the different TM and TE transmissions through the waveguide structure and normalize this by the spectrum of the reference. All absorption measurements were performed at room temperature

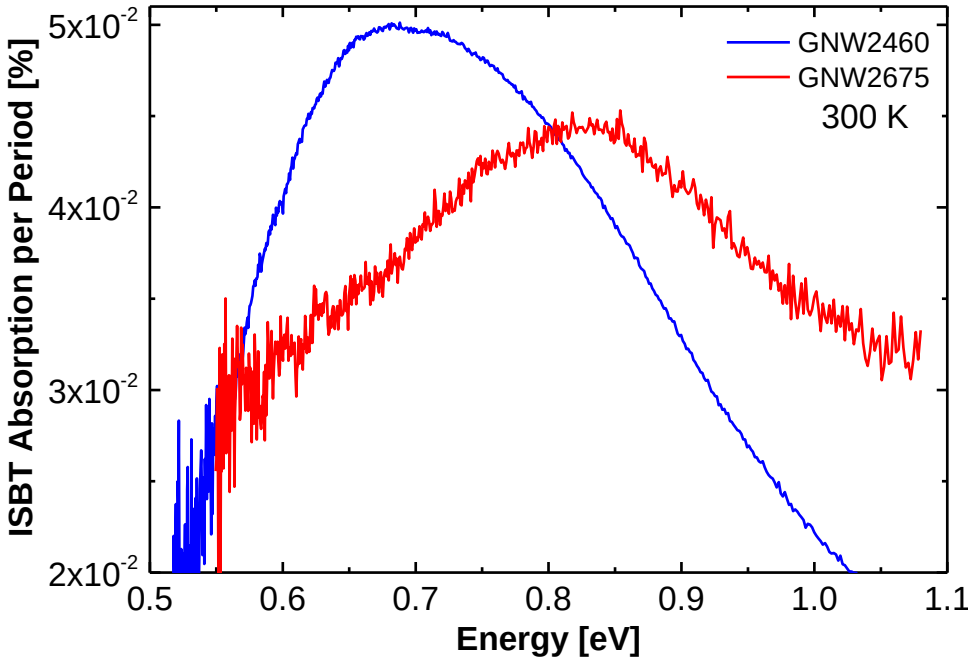

Figure 4.38 IR absorption spectra of the two MQW samples at room temperature. The FWHM of GNW2460 is with 370 meV much broader than for GNW2675 (250 meV), caused by higher doping. For GNW2460 e1-e2 and e2-e3 is absorbing, leading to a broader spectrum. (measured in TU Dortmund AG Betz)

The absorption maximum for sample GNW2460 is about 0.7 eV and for the sample GNW2675 it is at 0.83 eV, which is caused by the different layer thicknesses. The

FWHM of sample GNW2675 is 250 meV and for sample GNW2460 it is 370 meV. The FWHM of GNW2460 is higher than that cited in literature for both the cubic [8][6] and the hexagonal [92-94] phase. The FWHM of sample GNW2675 is close to the value 267 meV reported for similar structures [6]. The explanation will be given in the following together with the detailed presentation of the different energy levels and transitions provided by nextnano³.

Figure 4.39 shows the band diagram for a QW thickness of 2.25 nm (left) and 1.8 nm (right) with the different energy levels at room temperature. Due to the partly strained AlN barriers the QW is also strained. This results in an average lattice constant of the MQW structure. The transition responsible in PL is the first electron to the first heavy hole transition (e1-hh1). For the IR absorption measurements the first and the second electron levels take part (e1-e2). As a result of unexpected high doping the Fermi energy E_F of the sample with 80 periods is above the e2 level, leading to an additional absorption (e2-e3) visible in Figure 4.38. This result in a much broader absorption compared to the sample with 40 periods.

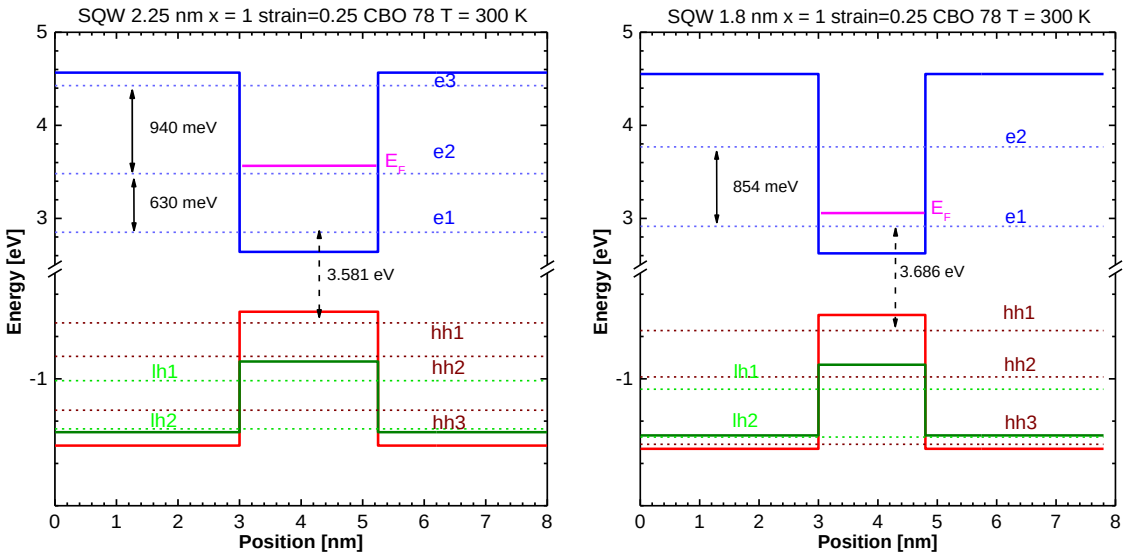

Figure 4.39 Band diagram of the sample with 80 periods (d_{QW} = 2.25 nm, left) and with 40 periods (d_{QW} = 1.8 nm, right) at 300 K.

In order to compare this very broad absorption with the nextnano³ simulations Figure 4.40 and Figure 4.41 can be used. Figure 4.40 presents the calculated transition energies between the electron levels in the conduction band. It shows the absence of an e3 level for QWs thinner than 2.25 nm, thus the QWs of sample GNW2640 has to be at least 2.25 nm thick. The transition energy of e1-e2 for this thickness is 630 meV as depicted in Figure 4.39 (left) and e2-e3 has 940 meV. Taking both transitions into account the absorption of GNW2460 can be explained. Furthermore, in Figure 4.40 the needed QW thickness for an e1-e2 transition with an energy difference of 0.8 eV (1.55 µm) can be seen. The MQW with the QW thickness of 1.8 nm is very close to this transition, as also provided by the nextnano³ calculations.

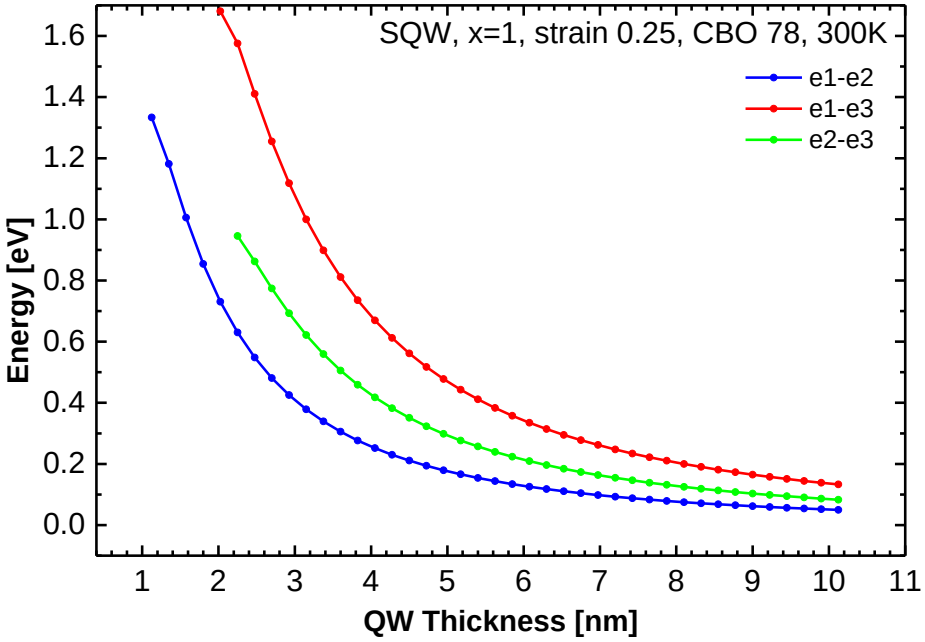

Figure 4.40 Calculated ISBT of a single QW with a degree of relaxation of 0.25 and AlN barriers at 300K.

Figure 4.41 shows the bound energy levels provided by nextnano³ for a single QW with AlN barriers partly strained on a c-GaN buffer layer at 300 K. The AlN cannot be measured in HRXRD, thus the degree of relaxation for x = 1 is determined with the additional SL peaks visible in RSM along (113) to $R = 0.25 \pm 0.04$.

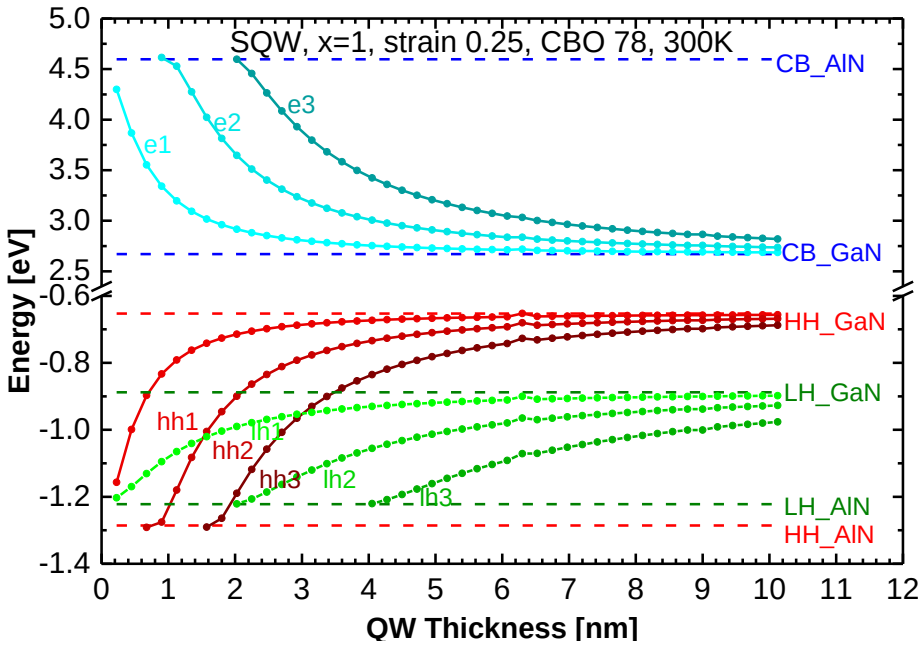

Figure 4.41 Simulated energy levels for electrons (e), heavy holes (hh) and light holes (lh) of a single c-GaN QW with AlN barriers partly strained on c-GaN buffer at 300 K.

Only two of the MQW structures (GNW2460, GNW2675) show IR absorption, although the experimental data of AFM, HRXRD and PL are similar also for the non-absorbing samples. The reason for the difference in the IR absorption couldn't be identified. There is no correlation on the substrate, doping and period number observable in PL (see previous chapter).

4.4.6 Intersubband Absorption Linewidth and Roughness

This subchapter deals with the influence of interface roughnesses on the intersubband absorption linewidth. All considerations and calculations in this chapter have been performed by me. The FWHM of the optical measurements of the MQW samples is affected by the amount of defects and monolayer fluctuation. The main contribution on the linewidth is the ML fluctuation. To describe the influence of the thickness variation of the QW width L on the energy levels E_m and E_n, the following formula for the form factor F_{mn} can be used [95].

$$F_{mn} = \sqrt{\frac{\partial E_m}{\partial L} \cdot \frac{\partial E_n}{\partial L}} \tag{4.4}$$

The energy levels have been simulated with nextnano³ for different QW thicknesses. The function used for the fits is:

$$y = \frac{A}{x-C} - y_0 \tag{4.5}$$

There is a deviation to the fit for very thin QWs. In case of the first electron level e1 this occurs at 0.225 nm and for e2 it starts for 1.35 nm. In Figure 4.42 the electron energy levels for a c-GaN/AlN QW are plotted. They have been simulated with nextnano³ for a degree of relaxation of 0.5 at 300K. The derivative of this fit function was taken for the calculation of F_{mn} (see Figure 4.43).

$$y' = -\frac{A}{(x-C)^2} \tag{4.6}$$

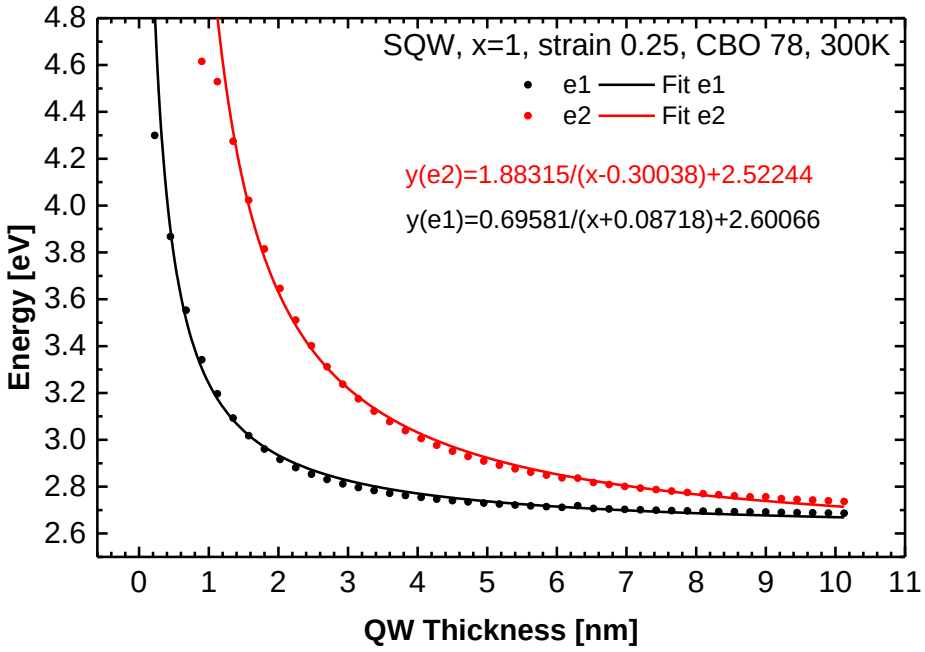

Figure 4.42 Electron energy levels for a c-GaN/AlN QW provided by nextnano³ with a degree of relaxation of 0.5 at 300 K.

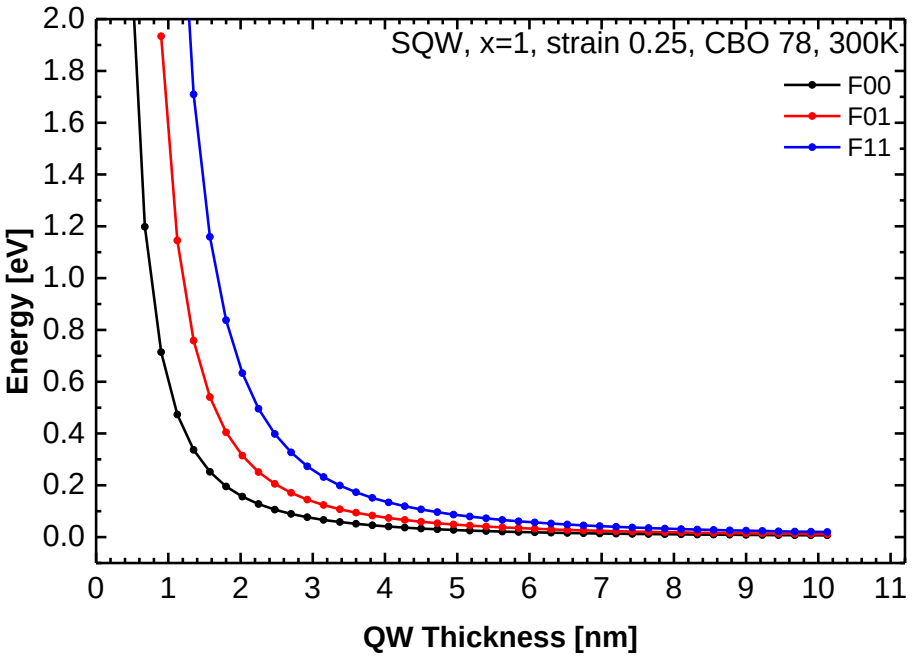

Figure 4.43 Influence of the QW thickness on the electron energy levels for a c-GaN/AlN QW.

In the following a simple roughness model is used to describe the influence on the absorption linewidth. The theory provided by Ando [95] connects the intersubband line shape for elastic scattering processes with the real part of the electric conductivity $\sigma_{zz}(\omega)$. The absorption at the frequency ω close to the energy difference of the subbands E_{10} depends on the optical scattering matrix element $\Gamma_{opt}(E)$ and the Fermi distribution $f(E)$.

$$Re\ \sigma_{zz}(\omega) \sim \int \frac{\Gamma_{opt}(E)}{(\hbar\omega - E_{10}) + \Gamma_{opt}(E)^2} f(E) dE \tag{4.7}$$

The scattering matrix element consists of the scattering matrix elements of the intraband and the interband.

$$\Gamma_{opt}(E) = \frac{1}{2}\left(\Gamma_{intra}(E) + \Gamma_{inter}(E)\right) \tag{4.8}$$

Both scattering elements depend on an exponential function, which has to be integrated for all scattering angles θ.

$$\Gamma_{intra}(E) = \frac{m^* \Delta^2 \Lambda^2}{\hbar^2} (F_{00} - F_{11})^2 \int_0^{\pi} e^{-q^2 \Lambda^2 / 4} d\theta \tag{4.9}$$

$$\Gamma_{inter}(E) = \frac{m^* \Delta^2 \Lambda^2}{\hbar^2} {F_{01}}^2 \int_0^{\pi} e^{-\tilde{q}^2 \Lambda^2 / 4} d\theta \tag{4.10}$$

The other parameters used are the effective mass m^*, the correlation length Λ, the mean height Δ of the roughness. The absolute values of the two-dimensional scattering vector q and $\tilde{q}$ can be expressed as:

$$q^2 = \frac{4m^*}{\hbar^2} E(1 - \cos\theta) \tag{4.11}$$

$$\tilde{q}^2 = \frac{4m^*}{\hbar^2}\left(E + \frac{E_{10}}{2} - \sqrt{E(E + E_{10})}\cos\theta\right) \tag{4.12}$$

For the calculation of the absorption Matlab was used. The source code can be seen in the appendix.

In the following the experimental results will be compared with the theoretical expectations considering also the influence of the material system on the FWHM of the intraband absorption between e1-e2. In Table 4.7 the main influences on the absorption linewidth for c-GaN and GaAs are collected. In equation 4.9 and 4.10 the effective mass m^* changes the linewidth linearly. The other contribution is the thickness fluctuation Δ of the QW ending up to different energy levels and thus broadening the width for a higher fluctuation quadratically.

Table 4.7 Comparison of two simulated QW structures with the same thickness of 2.025 nm consisting of different materials. The difference for the FWHM of the absorption between e1-e2 is mainly caused by the effective mass and the influence on thickness fluctuations of the QW on the energy levels F00, F01, F11.

	c-GaN/AlN	**GaAs/AlAs**
Effective Mass e	0.19[96]	0.069[95]
(F00-F11) [eV/nm]	0.5	0.08
F01 [eV/nm]	0.3	0.5
FWHM [eV]	2.78	0.047

For a GaAs/AlAs QW with thickness of 2.025 nm the calculated width in absorption is much smaller due to the smaller effective mass and the weaker thickness dependency of the energy levels. Thus for similar values of the correlation length $\Lambda = 4.3$ nm and the mean height $\Delta = 0.45$ nm of the roughness the FWHM of the absorption of GaN is 2.78 eV and in case of GaAs 47 meV (see Figure 4.44).

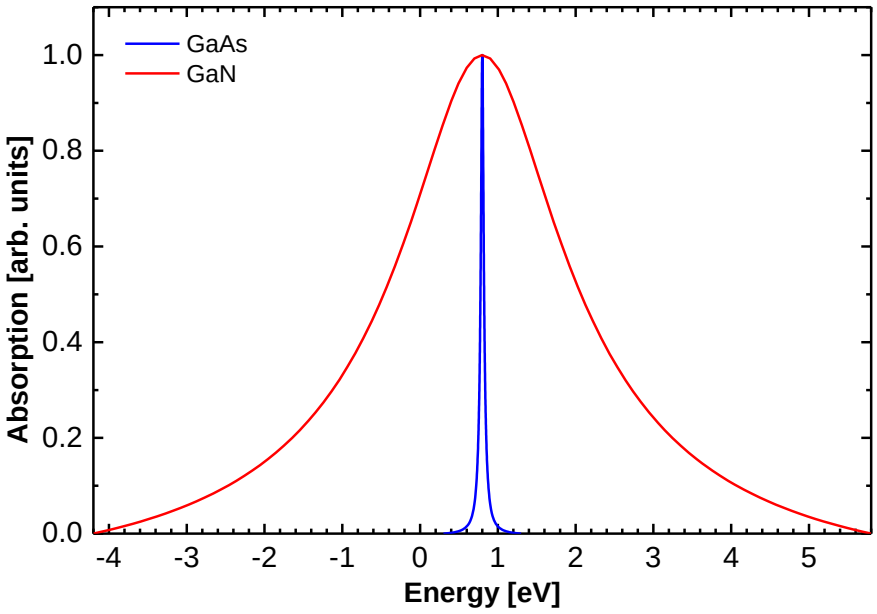

Figure 4.44 Calculated absorption between e1-e2 for a single QW of 2.025 nm for two material systems (GaAs/AlAs blue, GaN/AlN red) for the correlation length $\Lambda = 4.3\,nm$ and the mean height $\Delta = 0.45\,nm$ of the roughness.

Comparing the calculation for a realistic FWHM as measured of a GaN/AlN MQW (GNW2675) reveals a good match for a correlation length $\Lambda = 0.53\,nm$ and a mean height $\Delta = 0.45\,nm$ of the roughness. In Figure 4.45 the measurement of the GaN/AlN MQWs (blue) is fitted by a Voigt function (red) and plotted together with the calculated absorption (green) revealing a good match. The interpretation of these fit parameters is described below at a preliminary TEM measurement.

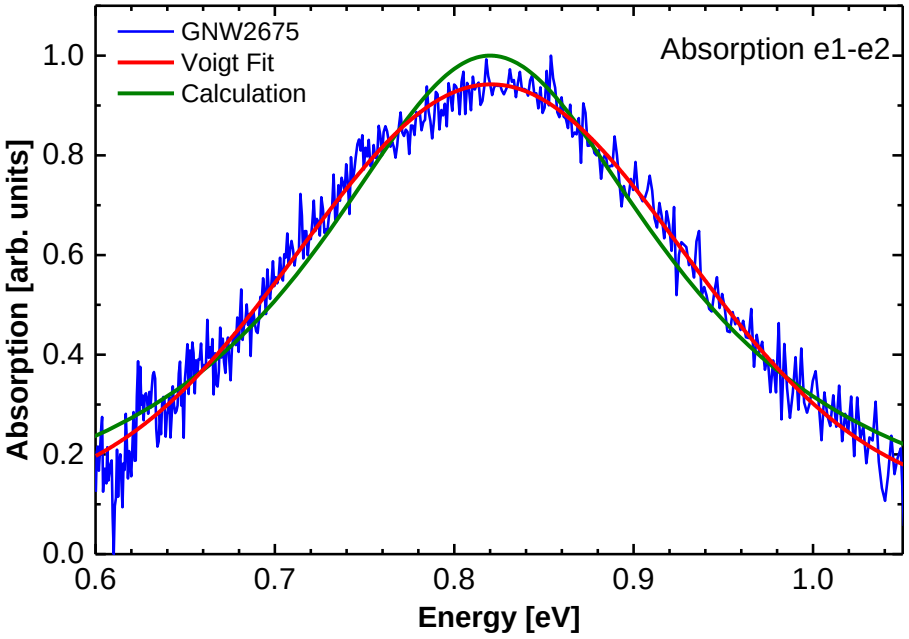

Figure 4.45 Absorption measurement of GNW2675 together with the calculated absorption (green). The calculation was performed with a correlation length $\Lambda = 0.53\,nm$ and a mean height $\Delta = 0.45\,\mathrm{nm}$ of the roughness.

Figure 4.46 shows a TEM image of an MQW grown by Christian Mietze (sample GNC2206). It reveals a much smoother interface roughness compared to the sample surface, thus the AFM RMS will not be used for the calculation of the FWHM in the absorption spectra. An interface roughness of about ± 2 ML is assumed (0.45 nm). As estimation for the correlation length the excitonic radius of c-GaN is considered (about 2.9 nm). In this length the interface is always rough, because the step size of the individual roughness regions is much smaller than 3 nm. For GaAs this is not the case, there are larger regions with similar thickness compared to the excitonic radius. So a much smaller correlation length compared to GaAs is assumed, in order to fit with the experiment of c-GaN QWs.

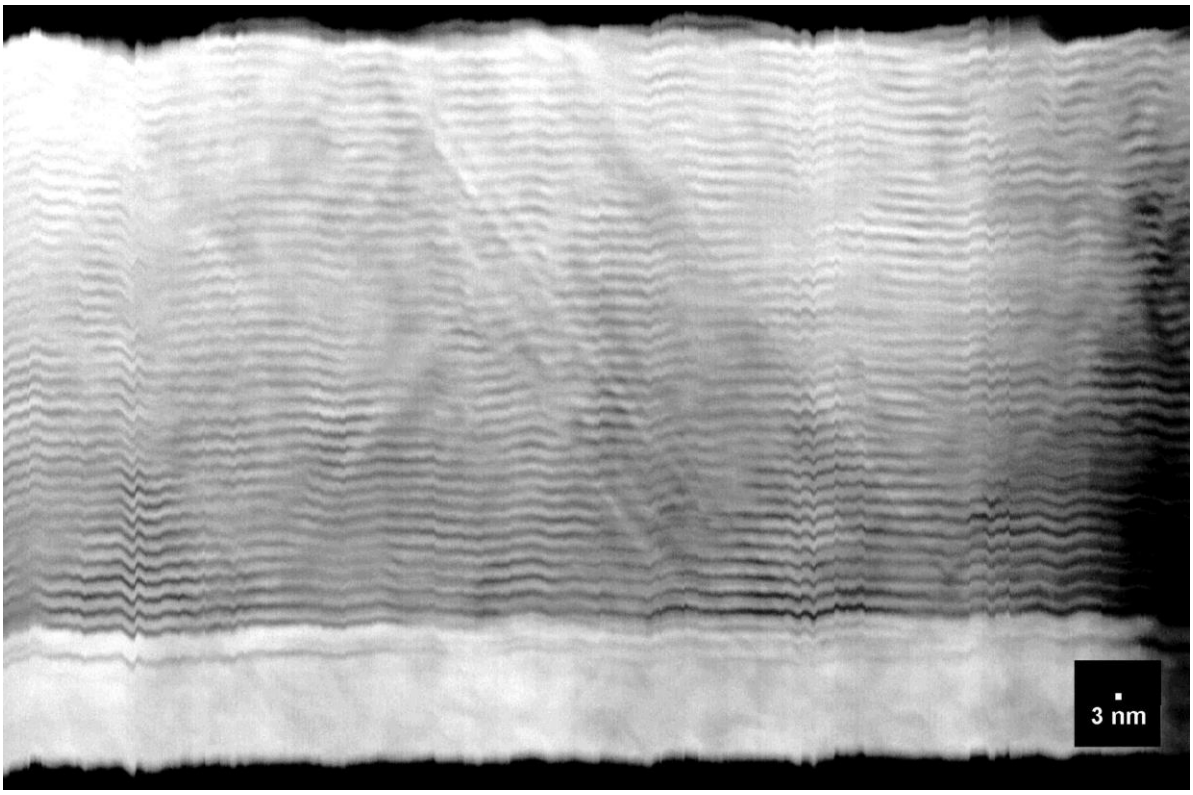

Figure 4.46 TEM Image of an MQW GNC2206 (provided by Christian Mietze)

In Figure 4.47 the influence of the correlation length on the FWHM in the absorption for a fixed roughness of 0.45 nm can be seen. A value of 0.54 leads to a FWHM of 250 meV as measured for sample GNW2675.

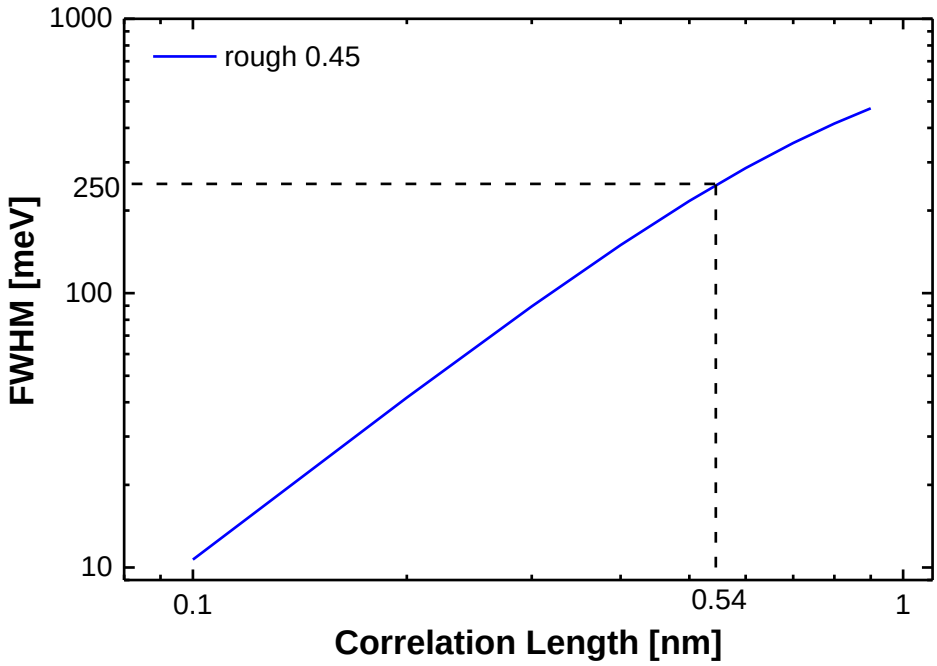

Figure 4.47 Calculated FWHM of the absorption for various correlation lengths. The value of 0.54 nm fits best with the experimental FWHM of 250 meV.

4.4.7 Non-linear Optical Measurements

The sample GNW2460 was also investigated by a degenerate femtosecond pump-probe setup to analyse the ultrafast and nonlinear dynamical response of the ISBT (see chapter 3.9). In Figure 4.48 three curves are depicted. The TE polarized excitation with 65° angle of incidence shows no nonlinear effect as expected (blue dots). Besides the black and red curve correspond to the TM polarized light with 90° and 65° angle of incidence as indicated in the inset. For the angle of 90° normally no coupling is expected, but the roughness of the interfaces allow for some intensity at this angle. The coupling between the light and some residual in-plane components of the electric field in the ISBT is for 65° higher than for 90°, because the component parallel to the MQW layers is increased. The pump pulse with central photon energy of 0.82 eV excites charge carriers into higher energy levels, thus no additional carriers can be absorbed. This leads to a higher transmission. Further measurements with variation of the pump irradiance revealed a third order susceptibility in the order of $\mathrm{Im}\,\chi^{(3)} \sim 1.1 \cdot 10^{-20}\ \mathrm{m^2/V^2}$ as described in [10].

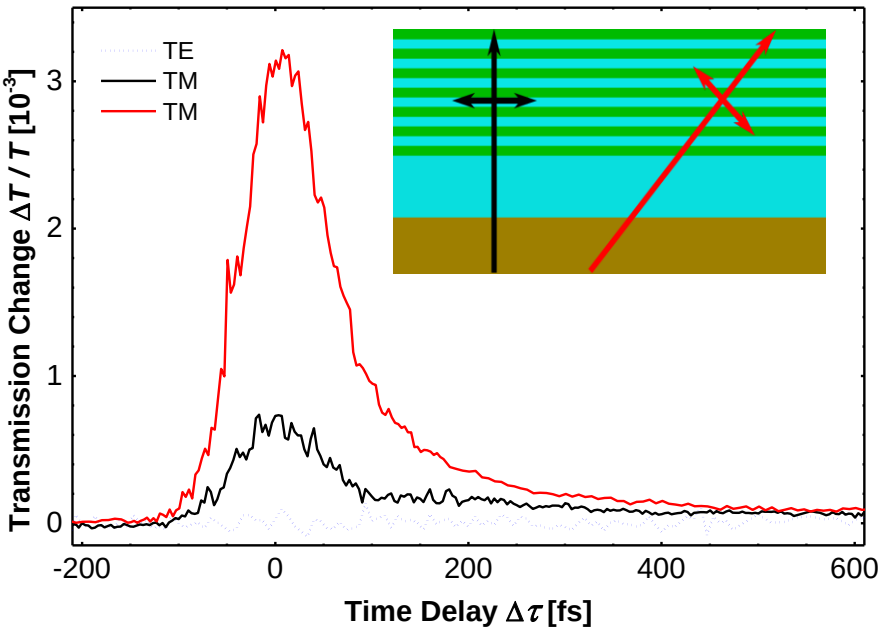

Figure 4.48 Pump induced change of the transmission of the MQW for a central photon energy of 0.82 eV. The blue curve corresponds to TE polarized light (angle of incidence 65°). The black and red curves belong to the TM polarisation with different angle of incidences, as can be seen in the inset. (measured in TU Dortmund by Thorben Jostmeier)

Figure 4.49 depicts the maximum transmission change $\Delta T/T$ at nominally zero time delay for different irradiance of pump pulses with central photon energy of 0.81 eV.

The linear behaviour indicates, that the absorption of the pump pulse doesn't saturate. For the nonlinear optical susceptibilities, this finding suggests that the pump probe measurements are restricted to the $\chi^{(3)}$ regime. The pump power has no significant influence on the temporal shape of the transients.

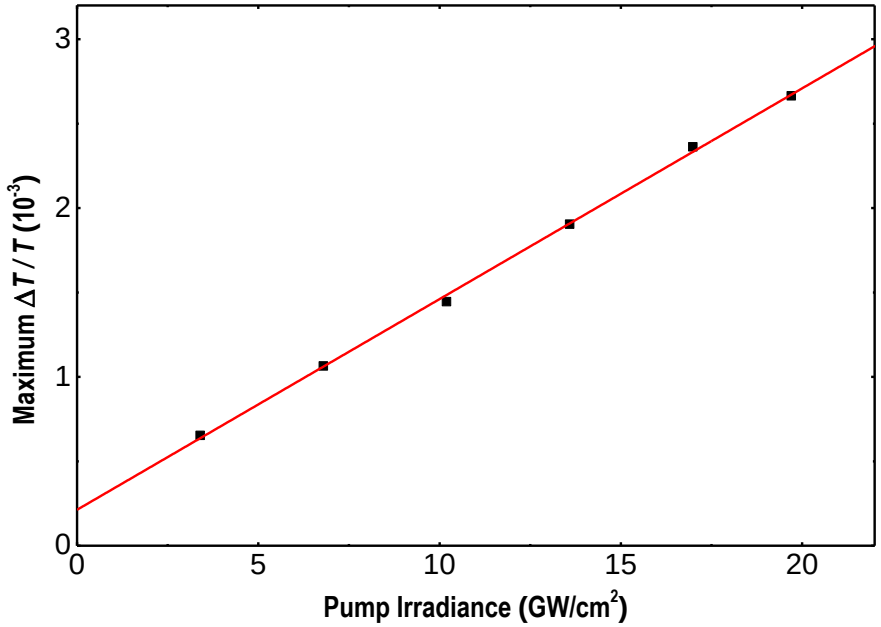

Figure 4.49 The peak pump-probe signal for various pump irradiances (central photon energy 0.81 eV, TM polarisation, 65° angle of incidence). The red line is a linear fit. (measured in TU Dortmund by Thorben Jostmeier)

4.4.8 Summary MQWs

In this chapter several Si doped cubic AlN/GaN multi quantum well (MQWs) samples have been investigated in order to achieve a systematic understanding of the intersubbandtransition (ISBT). This ISBT is very important for the field of non-linear optics, because of the high non-linear properties. Furthermore in our group III-nitride system the high band offset in the conduction band allows for a wavelength of the ISBT that covers the 1.55 µm range interesting for telecommunication.

At first some important information about the growth is presented followed by a chapter about the high resolution X-Ray diffractometry on the MQWs. Additional SL peaks have been determined at MQWs with HRXRD RSM around the (002) and (113) reflections. Strain investigations of the heterostructures have been performed by HRXRD RSM around (113) revealing partly strained MQWs with $\mathrm{R} = 0.25 \pm 0.04$. The strain is also validated by the theoretical calculations of the transition energies via nextnano³. Furthermore transmission electron microscopy (TEM) measurements on the MQW structures provided the real layer thickness. This thickness was used for the transition energy calculation via nextnano³ and a comparison with the PL data revealed a good agreement.

Another chapter deals with the investigation of the MQWs via photoluminescence spectroscpy (PL). These measurements have been used to analyse the influence of the doping, substrate and period number on the optical behaviour. There is no influence on the FWHM of the PL emission bands obersable for all these parameters.

In the next chapter intersubband absorption experiments were done with cubic AlN/GaN MQWs. The FWHM of this absorption was theoretically fitted leading to a correlation length of $\Lambda = 0.53\,\mathrm{nm}$ and a mean height $\Delta = 0.45\,\mathrm{nm}$ of the roughness. Furthermore a pump probe setup was used to measure the non-linear behaviour of MQW structures revealing a third order susceptibility of $\mathrm{Im}\,\chi^{(3)} \sim 1.1 \cdot 10^{-20}\,\mathrm{m}^2/\mathrm{V}^2$.

5 Simulation

For the interpretation of the experimental data in this thesis several simulations have been done. One of the great challenges in this thesis was the absence of consistent parameters for the cubic group III nitrides, thus all the experimental data have been used to identify a consistent parameter set. The parameters used in this thesis can be seen in the appendix. All theoretical considerations in this chapter have been done by me.

For the understanding of the band structure, energy levels and transitions of the QW structures nextnano³ (nn³) was used. Furthermore the HRXRD measurements for the MQWs are investigated by MadMax, in order to extract the exact layer thicknesses of the ω-2θ curves.

5.1 Nextnano³

Nextnano³ is a commercial available self-consistent Schrödinger-Poisson solver. These simulations are based on the effective mass approximation. For all nominally undoped samples a background n-type doping of around $5 \cdot 10^{17}\ cm^{-3}$ in $Al_xGa_{1-x}N$ and of around $1 \cdot 10^{17}\ cm^{-3}$ in GaN is assumed for the calculations [75]. The information about the energy levels provided by nextnano³ does not include excitonic effects. Thus for a comparison of the transition energies with experimental data the excitonic binding energy is calculated as shown in theory chapter and subtracted from the theoretical values. In addition, the band offset between $Al_xGa_{1-x}N$ and GaN is considered as explained in chapter 2.4. For the calculation of the band edges of valence and conduction band nextnano³ take the split off energy Δ_{SO} into account [97].

$$E' = E + \frac{\Delta_{SO}}{3} \tag{5.1}$$

HRXRD measurements revealed a partial strain in all heterostructures presented in this work. But nextnano³ cannot treat partial strain, only pseudomorphical strained or unstrained structures can be defined in the parameters of the program. So a virtual lattice constant $a_{buffer}^{virtual}$ is used replacing the lattice constant of the cubic GaN buffer layer, in order to achieve a partial strain in the heterostructure as delivered by HRXRD RSM. Besides the relaxed lattice constant of the $Al_xGa_{1-x}N$ layers $a_{buffer}^{virtual}$ is interpolated between the relaxed cubic GaN and relaxed cubic AlN (bowing factor b_{Bowing} = 0.85 [77]). The lattice constant of the strained $Al_xGa_{1-x}N$ is calculated by

equation (5.2) to realize the measured degree of relaxation for the $Al_xGa_{1-x}N$, provided by HRXRD RSM along the (113) direction.

In addition, the degree of relaxation in the QW $Strain_{QW}$ is considered to be $1 - Strain_{AlGaN}$, due to similar ratios of the elastic coefficients for $Al_xGa_{1-x}N$ and GaN. (a small part of the input file is shown in Figure 5.1)

$$a_{buffer}^{virtual} = \left(1 - Strain_{QW}\right) \cdot a_{GaN} + Strain_{QW} \cdot a_{AlGaN}^{rel} \quad (5.2)$$

This simple strain model assumes a constant strain over the whole structure. Nevertheless this assumption is consistent with HRXRD investigations of thick $Al_xGa_{1-x}N$ bulk samples (> 150 nm), revealing a partial strain even for x > 0.7. This was not expected, because these $Al_xGa_{1-x}N$ layers are well above the critical thickness [77].

Nextnano³ provides the possibility to create macros (marked in purple), so easy calculations can be done to adapt the parameters for each structure without the need to change the whole input file. The most important parts are collected in Figure 5.1. The blue marked words are comments for the developer and are ignored by nextnano³. The complete input file is attached in the appendix.

```
!Turn on the macro function
%FunctionParser = yes

%Strain_AlGaN = 0.48E0 ! 1= pseudomorph
%Strain_QW = 1-%Strain_AlGaN

%g_Buffer = (1-%Strain_QW) * %g_GaN+ (%Strain_QW)* %g_rel_AlGaN
```

Figure 5.1 Part of the input file necessary for the strain implementation. The $strain_{AlGaN}$ is measured by HRXRD, to provide a virtual buffer layer lattice constant.

5.2 MadMax and ω-2θ Profiles

In order to investigate the HRXRD data the program MadMax (Massively Accelerated Dynamical Multilayer Analysis by X-ray diffraction) was used [98]. It is suitable to evaluate the influence of strain and different layer thicknesses on ω-2θ curves in different directions. In this thesis only the (113) and (002) directions are measured. MadMax simulate diffraction profiles in co-planar diffraction geometry. Furthermore complex heterostructures can be calculated by adding all the different layers. For each layer the degree of relaxation R can be set. A value of R = 0 corresponds to a fully strained layer, thus this layer gets the lattice constant of the previous layer. For R = 1 the layer is fully relaxed leading to the lattice constant implemented in the database. In addition, ternary semiconductors can be introduced with various mixtures, by changing the x value. A screenshot of the main window is shown in Figure 5.2. Unfortunately the material parameters for the cubic nitrides are slightly different from the values determined recently with samples of our workgroup. The lattice constants used in MadMax for c-GaN and c-AlN are 0.452 nm and 0.438 nm, respectively. Moreover, 3C-SiC isn't implemented at all. To solve these problems the lattice constant of a GaAs substrate is replaced by the value for 3C-SiC (0.43596 nm [99]) and c- $Al_xGa_{1-x}N$ with x = 0.12 is used to match 0.4503 nm [35] expected for c-GaN. Only the correct lattice parameter for c-AlN (0.4373 nm [100]) couldn't be reached, this will be partly solved applying a different strain to the c-AlN layers. The result of the input of Figure 5.2 can be seen in Figure 5.3.

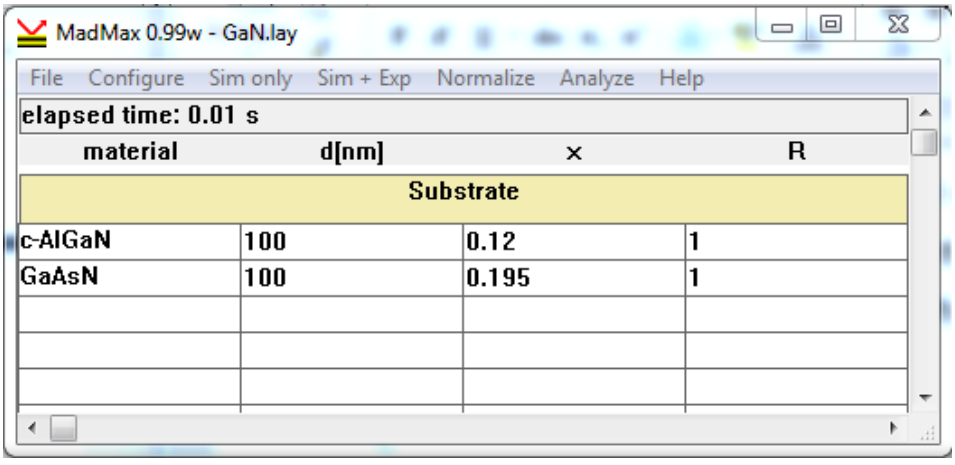

Figure 5.2 Input window of MadMax for a c-GaN reference sample. The c- $Al_xGa_{1-x}N$ layer is used to achieve the lattice constant of c-GaN. The GaAsN layer matches the lattice constant of the Si in the substrate.

The red line corresponds to the measured profile for a 500 nm (GNW2614) thick c-GaN reference sample and the black line is the calculated profile. The main intensity is caused by the 3C-SiC layer, which serves as a reference point. Next to this peak the c-GaN peak is visible and a very narrow peak appears at the left side of the profile. This narrow peak originates from the Si of the substrate and is measured for all samples and wafers. To evaluate the lattice constant necessary for this peak a $Ga_xAs_{1-x}N$ layer with x = 0.195 is used. This layer matches the lattice constant of Si with 0.5431 nm [101].

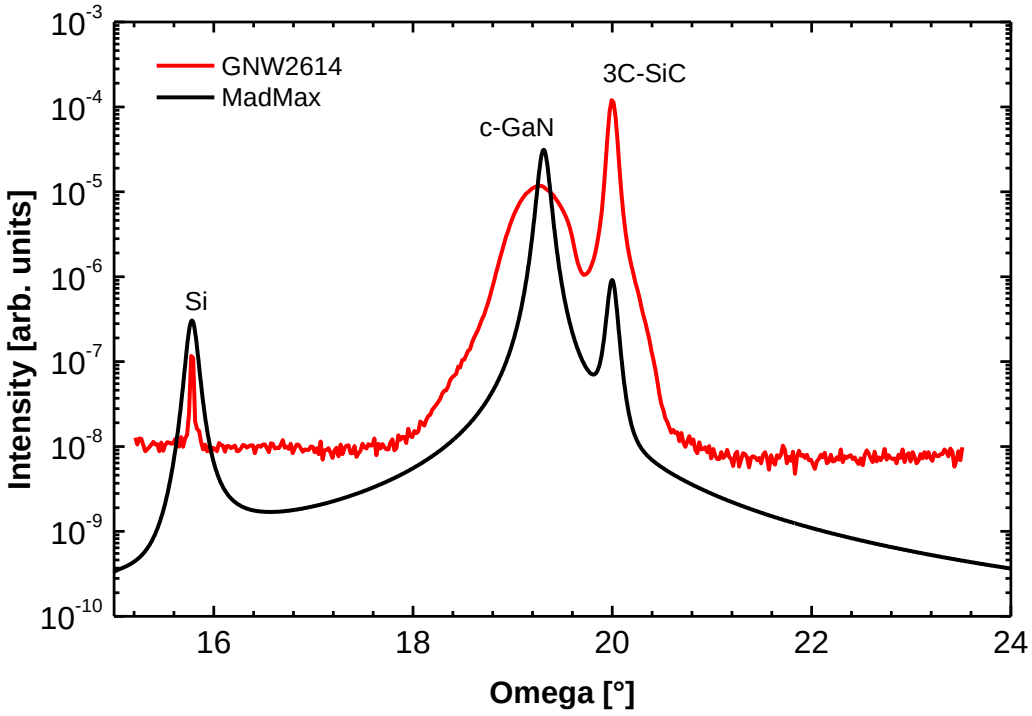

Figure 5.3 MadMax output profile (black) with the measured ω-2θ profile of a c-GaN reference sample (red) in (002). The three peaks are caused by the Si, c-GaN and 3C-SiC, respectively.

In detailed investigation of the ω-2θ profiles several very weak peaks appear in long measurements (around 24h per profile). These peaks originate from the substrate. This can be seen comparing a profile of the substrate (blue) with a MQW sample (green) as plotted in Figure 5.4. Only the c-GaN layer is causing a difference for those two profiles. This MQW sample shows no additional peaks corresponding to the SL.

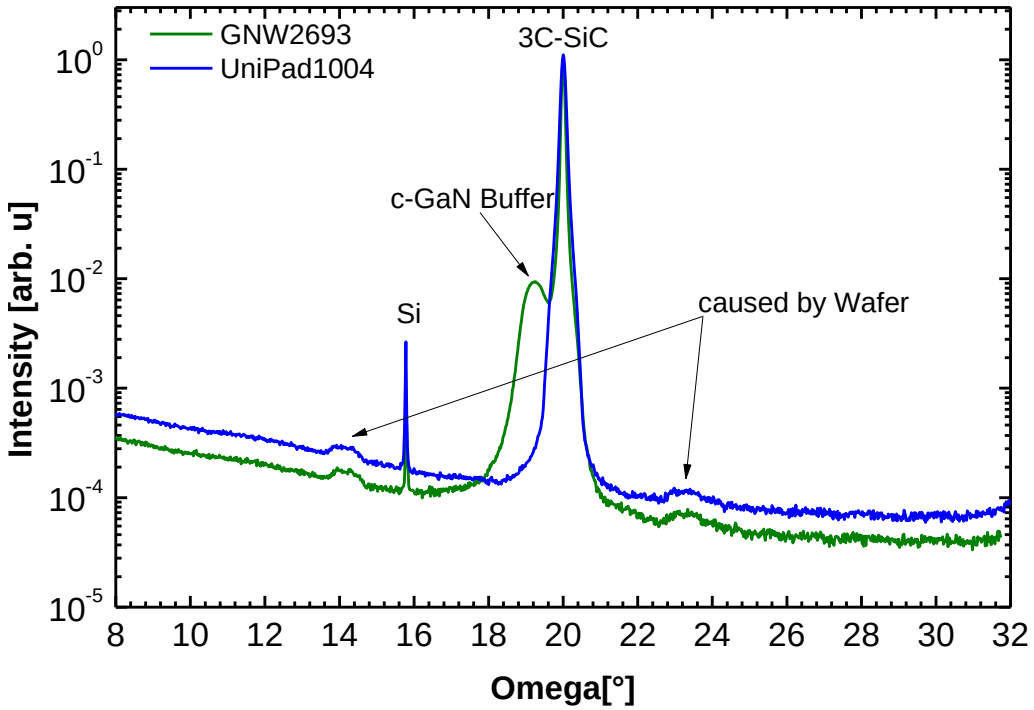

Figure 5.4 Comparison of two ω-2θ measurements in the (002) direction. The green curve corresponds to a MQW sample and the blue curve to a wafer piece without any grown layer.

In Figure 5.6 an ω-2θ measurement of a MQW sample with 80 periods in (002) direction is shown. This curve was fitted by 3 Gaussian curves for the sample emission and one sigmoid curve for the SiC peak. There are additional peaks visible which are caused by the SL (red Gaussian, blue Gaussian), as well as the c-GaN buffer layer peak (green Gaussian). The red dotted line corresponds to simulation data provided by MadMax (input in Figure 5.5). HRXRD measurements have shown a partial strain in the MQW layers caused by the c-GaN buffer layer. This partial strain was achieved in the simulation by inserting a virtual $Al_xGa_{1-x}N$ layer with x = 0.35. This results in a degree of relaxation of 0.25 and an in-plane lattice constant of 0.4471 nm, as measured in HRXRD. The QW thickness of 2.025 nm is exactly the same value as provided by the investigation of the optical experiments utilising nextnano³. This is a further proof of the consistence of all the theoretical considerations as well as the parameters used for the calculations.

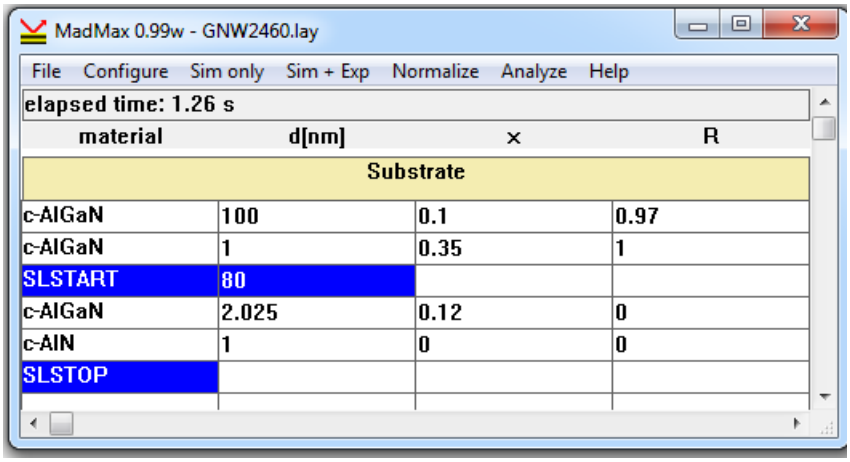

Figure 5.5 Input window of MadMax for a MQW sample with 80 periods of 2.025 nm GaN and 1 nm AlN on top of a c-GaN buffer layer. This buffer layer provides a partial strain, which was achieved inserting a virtual $Al_xGa_{1-x}N$ layer with x = 0.35.

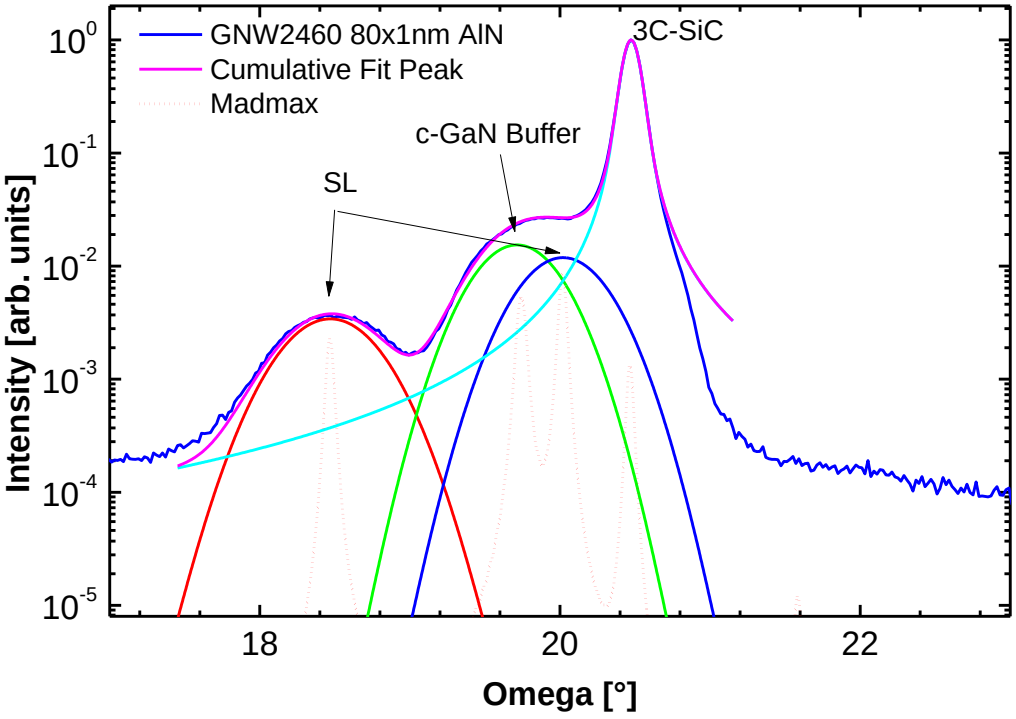

Figure 5.6 ω-2θ measurement and simulation data in the (002) direction for a MQW sample with 80 periods. Three Gaussian fit curves explain the experimental data very well corresponding to the first SL peak, the c-GaN buffer layer and the second SL peak.

6 Summary

In this thesis asymmetric double QWs (ADQW) and multi QWs (MQW) were used to investigate the carrier dynamics between QWs. A detailed analysis of the coupling behaviour of single and multi QWs based on cubic GaN/$Al_xGa_{1-x}N$ and the influence on optical properties was done. This leads to the experimental and theoretical knowledge needed for the understanding of intersubband transitions. These transitions are important for the research of non-linear effects and unipolar devices, which are emitting at a wavelength of 1.55 µm.

At first cubic GaN/$Al_xGa_{1-x}N$ ADQWs with different Al content in the barriers have been exploited to get a general insight into the coupling behaviour. For the series with x = 0.26 the coupling starts at 7 nm thick barriers, for x = 0.64 the coupling begins at 3 nm thick barriers and for x = 1 it is estimated to be 1-2 nm. For the theoretical evaluation rate equations, time-resolved photoluminescence (TRPL) and conventional photoluminescence were used. A clear correlation between the decay times of the TRPL data and the barrier thickness is shown. This is an indication for non-resonant tunnelling of carriers between the two QWs.

In addition, an insight into excited energy levels of an ADQW was performed by Photoluminescence Excitation Spectroscopy (PLE). This revealed the existence of excited energy levels as expected by the theory. These excited energy levels are crucial for the design of complex heterostructures and devices based on intraband transitions.

Also intersubband absorption experiments were done with Si doped cubic AlN/GaN MQWs. The FWHM of this absorption was theoretically fitted leading to a correlation length of $\Lambda = 0.53$ nm and a mean height $\Delta = 0.45\,\mathrm{nm}$ of the roughness. Furthermore a pump probe setup was used to measure the non-linear behaviour of MQW structures revealing a third order susceptibility of $\mathrm{Im}\,\chi^{(3)} \sim 1.1 \cdot 10^{-20}\ \mathrm{m^2/V^2}$.

Additional SL peaks have been determined at MQWs with HRXRD RSM around the (002) and (113) reflections. Strain investigations of the heterostructures have been performed by HRXRD RSM around (113). They are also validated by the theoretical calculations of the transition energies via nextnano³. Furthermore ω-2θ scans have been done and compared to theoretical considerations via MadMax. The layer thicknesses determined via MadMax match well with the expected layer thicknesses and the measured strain. This is most important in case of heterostructures with AlN barriers having few periods. In such structures the strain of the AlN layers can-

not be measured and the theory provided by nextnano³ and MadMax can be used to get strain information. Besides, TEM measurements on the MQW structures have been used to determine the real layer thickness. This thickness was used for the transition energy calculation via nextnano³ and a comparison with the PL data revealed a good agreement.

A systematic insight into heterostructures based on GaN/$Al_xGa_{1-x}N$ was achieved. Also the theoretical models needed for energy transitions (nextnano³), layer thicknesses and strain (MadMax) are compared to the experiments and revealed a good agreement. In this process a set of parameters for cubic group III nitrides was improved successively.

Furthermore GaN/$Al_xGa_{1-x}N$ QWs have been investigated by picosecond acoustics to get an insight into the influence of strain pulses on such heterostructures. This revealed additional information about the strain behaviour, the interfaces and the layer thicknesses. Raman and HRXRD experiments of thick GaN layers have been compared to enable Raman as an additional measurement for the defect density and the layer thickness also for very thin layers. Such thin layers are difficult to measure with HRXRD. Besides Raman can achieve a much better spatial resolution compared with HRXRD.

7 Appendix

7.1 Sample List

Sample GNW	Substrate	Structure	Remark	Date
2345	UniPad 11-03 Novasic	GaN 500 nm		11.12.12
2346		GaN 460 nm		17.12.12
2347		GaN 470 nm		18.12.12
2348	11CO186 Novasic	GaN 380 nm		16.01.13
2349		GaN 150 nm		17.01.13
2350		GaN 74 nm		17.01.13
2351		GaN 180nm/AlGaN 180nm	$x \approx 0{,}3$	21.01.13
2352		180nm/../170nm	$x \approx 0{,}3$	22.01.13
2353		170nm/../170nm	$x \approx 0{,}2$	23.01.13
2354		170nm/170nm	$x \approx 0{,}25$	24.01.13
2355		50nm/15nm/30nm/15nm/30nm	$x \approx 0{,}25$	28.01.13
2356		d=15nm, x=0,25 Series A		29.01.13
2357		d=5nm, x=0,26 Series A		30.01.13
2358		d=3,6nm, x=0,26 Series A		31.01.13
2359		d=10nm, x=0,26 Series A		04.02.13
2360		d=1nm, x=0,26 Series A		05.02.13
2361		d=15nm, x=0,19 Series B		06.02.13
2362		d=10nm, x=0,20 Series B		07.02.13
2363		d=5nm, x=0,20 Series B		11.02.13
2364		d=3nm, x=0,17 Series B		12.02.13
2365		d=1nm, x=0,20 Series B		13.02.13
2371		GaN	Optimization	27.03.13
2372		GaN AlGaN		28.03.13
2373		GaN AlGaN		23.04.13
2374		GaN 600 nm		24.04.13
2375		200nm GaN / 200nm AlGaN	x=0,32	29.04.13
2376		200nm GaN / 200nm AlGaN	x=0,27	30.04.13
2377		200nm GaN / 200nm AlGaN	x=0,39	06.05.13
2378		200nm GaN / 200nm AlGaN	x=0,62	08.05.13
2379		200nm GaN / 100nm AlGaN	x=0,8	14.05.13
2380		d=15nm, x=0,21	Narrow QW below wide QW → reabsorption?	15.05.13
2381		d=15nm, x=0,21		16.05.13
2382		d=3nm, x=0,37 Series C		21.05.13
2383		d=3nm, x=0,67 Series C/D		23.05.13
2384		d=3nm, x=0,8 Series C		27.05.13
2385		d=3nm, x=0,13 Series C		29.05.13
2386		d= 15nm, x=0,63 Series D		04.06.13
2387		d= 1nm, x=0,65 Series D		05.06.13
2388		d= 5nm, x=0,62 Series D		11.06.13
2389		d= 10nm, x=0,60 Series D		13.06.13
2417	Unipad 1102	-	Optimization	08.01.14
2418		-		09.01.14
2419		600 nm GaN		15.01.14

2420		-	No Ga flashes in RHEED	21.01.14
2421		400 nm GaN		23.01.14
2422		400 nm GaN:Si	Si 1040°C	27.01.14
2423		200nm GaN/ 200nm AlGaN	x = 0,17	29.01.14
2424		550 nm GaN		13.02.14
2425		200 nm GaN/ 200 nm AlGaN	x = 0,13	17.02.14
2426		100 nm/ 5 nm/ 1,8 nm/ 5 nm		19.02.14
2427		100 nm/ 5 nm/ 1,8 nm/ 5 nm		21.02.14
2428		100 nm/ 5 nm/ 1,35 nm/ 5 nm		24.02.14
2429		-	Optimization	19.03.14
2430		-		20.03.14
2431		600 nm GaN	Leo	26.03.14
2432		200 nm GaN/ 75 AlGaN	x =0,15 Leo	27.03.14
2440		100 nm / 5nm / 1,35/5 / 0,675/ 5	AlN Leo	06.05.14
2441	Unipad 1102	100 nm/ 10 nm/ 10 nm/ 10 nm	X =0,3	07.05.14
2442		100 nm/ 30 nm/ 10 nm/ 30 nm	X =0,3	07.05.14
2443		100 nm/ 30 nm / 10 nm/ 30 nm	AlN	08.05.14
2444		100 nm / 15nm / 1,35/15 / 0,675/ 15	AlN Leo	09.05.14
2445		1 µm GaN	Leo	12.05.14
2446		100 nm/ 50 nm / 10 nm/ 50 nm	X = 0,1	13.05.14
2447		100 nm/ 50 nm / 10 nm/ 50 nm	X = 0,6	14.05.14
2448		100 nm/ 50 nm / 10 nm/ 50 nm	X = 0,8	14.05.14
2449		1 µm GaN: Si	Si 1100 °C Leo	15.05.14
2450		100 nm/ 50 nm	X = 0,3	16.05.14
2451		100nm/ 17x Multi DQWs	without step 1,35 nm/0,45 nm Leo	19.05.14
2452		100 nm/ 20x Multi DQWs	without step 1,35 nm/0,45 nm Leo	20.05.14
2453		100 nm/ 100 nm	X =0,3	21.05.14
2454		100 nm/ 50 nm / 10 nm/ 50 nm	X =0,3	21.05.14
2455		100 nm (Si)/ 30 nm/ 20x Multi DQWs/ 30 nm/ 100 nm (Si)	without step 1,8 nm/0,45 nm Leo	22.05.14
2456		100 nm/ 50 nm / 10 nm/ 50 nm	X =0,2	23.05.14
2457		100 nm (Si)/ 30 nm/ 20x Multi QWs/ 30 nm/ 100 nm (Si)	without step 1,8 nm Leo	26.05.14
2458	Unipad 1102	100 nm/ 50 nm / 10 nm/ 50 nm	X =0,5	28.05.14
2459		100 nm/ 50 nm / 5 nm/ 50 nm	X = 0,3	02.06.14
2460		100 nm / 80x Multi QWs	1,8 nm doped (Si 1080°C)	04.06.14
2461	11CO192	HEMT Single Channel no BB	Last AlN 3 nm, x=0,7	05.06.14
2462		HEMT Single Channel no BB	No Isolation	11.06.14
2463		HEMT Single Channel no BB	Last AlN 6nm, x=0,3	18.06.14
2464		HEMT Single Channel no BB	AlN 6nm, x=0,3, different spacer	24.06.14
2465		HEMT Single Channel BB	last AlN 6 nm	25.06.14
2466		HEMT Double Channel no BB	last AlN 6 nm	07.02.14
2467		HEMT Double Channel BB	last AlN 6 nm Wrong Ga temperature	03.02.14
2468			Growth stopped Leo	08.07.14
2469			Growth stopped Leo	08.07.14
2470		100 nm (Si)/ 30 nm/ 20x Multi QWs/ 30 nm/ 100 nm (Si)	with step 0,45nm / 0,45 nm/0,45 nm	09.07.14

2486	UniPad1102	100 nm/ 80*MQW	1,8nm GaN/ 1 nm AlN	24.09.14
2487		100 nm/ 80*MQW Temperature rampe	1,8nm GaN/ 1 nm AlN	25.09.14
2488	11CO186	-	Optimization	29.10.14
2489		-		04.11.14
2490		-		05.11.14
2491		-		11.11.14
2492		-		12.11.14
2542	UniPad10-04	-	Optimization	14.07.15
2543		600 nm GaN		15.07.15
2544		-		13.08.15
2545		-		19.08.15
2548		-		24.08.15
2549		AlN optimised		25.08.15
2550		GaN hexagonal		28.08.15
2551		GaN	Optimization	01.09.15
2552		GaN/ AlGaN		02.09.15
2553		GaN/ AlGaN		03.09.15
2554		GaN/AlGaN	Ga 920°C	08.09.15
2556		GaN/AlGaN	Ga 927°C	10.09.15
2557	Unipad 1101	GaN/AlGaN	Ga 926°C	11.09.15
2559		GaN 321 nm	Ga 926°C	15.09.15
2560		GaN 351 nm	Ga 924°C	16.09.15
2561		GaN 331 nm	Ga 922°C, Hexagonal	23.09.15
2562		GaN 292 nm	Ga 928°C	24.09.15
2564		GaN 323 nm	Ga 930°C	28.09.15
2565	14CO 051	GaN 326 nm		01.10.15
2566		100 nm/ 3 nm AlN/ 1.8 nm/ 3 nm AlN		05.10.15
2567		100 nm/ 3 nm AlN /1.8 nm QW:Si/ 3 nm AlN	No RHEED after AlN	06.10.15
2568		100 nm/ 3 nm AlN/ 1.8 nm/ 3 nm AlN	No RHEED after AlN	08.10.15
2569		100 nm/ 3 nm AlN/ 1.8 nm/ 3 nm AlN		09.10.15
2570		100 nm/ 3 nm AlN /1.8 nm QW:Ge/ 3 nm AlN	Hexagonal	13.10.15
2571		1h 17 min GaN	No RHEED at the end	14.10.15
2572		5 h GaN		14.10.15
2573		100 nm/ 3 nm AlN /1.6 nm QW:Si/ 3 nm AlN		15.10.15
2574		100 nm/ MQW	Shutter didn't work	19.10.15
2588		1h GaN		05.01.16
2589		31min GaN		06.01.16
2590		GaN AlGaN		07.01.16
2591		510nm GaN		11.01.16
2594	14CO-051	GaN QW/ 3nm AlN		18.01.16
2597		GaN QW/ 3nm AlN		20.01.16
2599		GaN QW Si/ 3nm AlN		22.01.16

2600		582 nm GaN:Si	4x10^19 cm^-3	26.01.16
2603	14CO146	MQW 12x	Hexagonal, growth stopped	03.02.16
2604		MQW 20x 1,8nm/3nm		04.01.16
2608		MQW 20x 1,8nm/5nm	Hexagonal	15.01.16
2610		MQW 20x 1,8nm/8nm	Bad quality	17.01.16
2612		MQW 5x 1,8nm/5nm	Delta doping	24.01.16
2613		MQW 20x 1,8nm/5nm	Delta doping	25.01.16
2614		4h30min GaN		29.01.16
2618		100 nm GaN/ AlGaN	Optimization	21.03.16
2619		100 nm GaN/ AlGaN	Optimization	22.03.16
2649		MQW 10x1,8nm/5nm	GaN:Si	23.03.16
2650		MQW 20x1,8/5		24.03.16
2651		MQW 5x		28.03.16
2652		MQW 20x	AlN:Si	30.03.16
2653		MQW 20x	AlN:Si(delta)	05.07.16
2654		MQW 20x	AlN:Si(delta)	06.07.16
2655		MQW 20x	GaN:Si(delta) edge of QW	12.07.16
2656	14CO-146	MQW 20x	GaN:Si(delta) middle of QW	14.07.16
2665	14C0-133		Optimization	28.09.16
2666			Optimization	29.09.16
2667		20x1,8nm/5nm	Si 1000°C	05.10.16
2668		MQW 20x	Si 940°C	06.10.16
2675	14CO050	MQW 40x1,8nm/1nm	Si 940°C	08.11.16
2678		MQW 45x	Si Shutter didn't work	10.11.16
2684	14CO-144	MQW 40x		18.11.16
2687		MQW 40x	Rotation during QW growth	23.11.16
2693	14CO-144	MQW 40x 3nm AlN		30.11.16
2694		MQW 40x GaN:Si(delta)		01.12.16
2698		MQW 40x GaN:Si 2 nm AlN	Bad in RHEED	08.12.16
2699		MQW 40x GaN:Si 2 nm AlN		09.12.16
2729	14CO050	MQW 60x	GaN:Si 940°C	08.03.17
2730		MQW 40x	GaN:Si 1000°C	15.03.17
2731		MQW 40x	GaN:Si 970°C	16.03.17
2732		MQW 50x	GaN:Si 940°C	17.03.17
2748	14CO-144	SQW 1,238 nm		03.05.17
2749	14CO050	DQW 40x	Al shutter didn't work	04.05.17

7.2 Literature

[1] N. Suzuki and N. Iizuka, Japanese Journal of Applied Physics **37**, 369 (1998).

[2] C. Gmachl, S. V. Frolov, H. M. Ng, S. N. G Chu and A. Y. Cho, Electronics Letters **37**, 178 (2001).

[3] J. D. Heber, C. Gmachl, H. M. Ng and A. Y. Cho, Appl. Phys. Lett. **81**, 1237 (2002).

[4] N. Iizuka, K. Kaneko and N. Suzuki, Electronics Letters **40**, 962 (2004).

[5] J. Hamazaki, S. Matsui, H. Kunugita, K. Ema, H. Kanazawa, T. Tachibana, A. Kikuchi and K. Kishino, Appl. Phys. Lett. **84**, 1102 (2004).

[6] H. Machhadani, M. Tchernycheva, L. Rigutti, S. Saki, R. Colombelli, C. Mietze, D.J. As, F.H. Julien, Phys. Rev. B **83** (2011) 075313.

[7] C. Gmachl and H.M. Ng, Electron. Lett. **39**, 567 (2003).

[8] E.A. DeCuir, E. Fred, M.O. Manasreh, J. Schörmann, D.J. As and K. Lischka, Appl. Phys. Lett. **91**, 041991 (2007).

[9] C. Mietze, M. Landmann, E. Rauls, H. Machhadani, S. Sakr, M. Tchernycheva, F. H. Julien, W. G. Schmidt, K. Lischka, and D. J. As, Phys. Rev. B **83**, 195301 (2011).

[10] T. Jostmeier, T. Wecker, D. Reuter, D. J. As, and M. Betz, Appl. Phys. Lett. **107**, 211101 (2015)

[11] T. Wecker, T. Jostmeier, T. Rieger, E. Neumannn, A. Pawlis, M. Betz, D. Reuter, D.J. As, J. Crystal Growth (2016) in press

[12] T. Wecker, F. Hörich, M. Feneberg, R. Goldhahn, D. Reuter, and D. J. As, Phys. Status Solidi B **252**, 873 (2015).

[13] T. Wecker, G. Callsen, A. Hoffmann, D. Reuter and D. J. As, Jpn. J. Appl. Phys. **55**, 05FG01 (2016)

[14] T. Wecker, G. Callsen, A. Hoffmann, D. Reuter, and D. J. As, submitted

[15] M. Beeler, E. Trichas and E. Monroy, Semicond. Sci. Technol. **28,** 074022 (2013).

[16] M. Beeler, C. Bougerol, E. Bellet-Amalaric, and E. Monroy, Phys. Status Solidi (a) **211**, No. 4, 761–764 (2014).

[17] F. Scholz, Semicond. Sci. Technol. **27**, 024002 (2012).

[18] D.J. As and C. Mietze, Phys. Status Solidi (a) **210**, 474 (2013).

[19] C. Mietze, M. Bürger, S. Sakr, M. Thernycheva, F.H. Julien, and D.J. As, Phys. Status Solidi (a) **210,** 455 (2013).

[20] L. Pavesi, M. Guzzi, J. Appl. Phys. **75**, 4779 (1994)

[21] H. Mathieu, P. Lefebvre, P. Christol, Phys. Rev. B, Vol **46**, Nr 7 (1992)

[22] M. Feneberg, M. Röppischer, C. Cobet, N. Esser, J. Schörmann, T. Schupp, D. J. As, F. Hörich, J. Bläsing, A. Krost, and R. Goldhahn, Phys. Rev. B **85**, 155207 (2012)

[23] John H. Davies, „The Physics of low- dimensional semiconductors“, Cambridge University Press (1998)

[24] T. Tada, A. Yamaguchi, T. Ninomiya, H. Uchiki, T.Kobayashi, and T. Yao, J. Appl. Phys. **63**, 5491 (1988).

[25] R. Sauer, K. Thonke, and W. T. Tsang, Phys. Rev. Lett. **61**, 609 (1988).

[26] S. L. Chuang, Physics of photonic devices, second edition, Wiley Verlag, 2009 S.384 372 365

[27] O. Gauthier-Lafayea, et al., Physica E **7** (2000) 12-9

[28] J. Faist, F. Capasso, D. L. Sivco, C. Sirtori, A. L. Hutchinson, A. Y. Cho, Science Vol. **264** (1994)

[29] M. Rüsing, T. Wecker, G. Berth, D.J. As, and A. Zrenner, Phys. Stat. Sol. (b) **253**, 778 (2016)

[30] H. Harima, J. Phys.: Condens. Matter **14**, R967–R993 (2002).

[31] M. Landmann, E. Rauls, and W. G. Schmidt, Phys. Rev.B **00**, 005300 (2017)

[32] E. Tschumak, PhD Thesis, University of Paderborn (2010)

[33] P. Gay, P.B. Hirsch, and A.Kelley, Acta Metall. **1**, 315 (1953).

[34] D. Hull and D. Bacon, Introduction to Dislocation (Butterworth-Heinemann, Oxford, 2011).

[35] T. Schupp, unpublished

[36] K. Kim, W. R. L. Lambrecht, and B. Segall, Phys. Rev. B **52**(24), 16310–16326 (1996).

[37] J. Stangl et. al., Physik Journal **3** (2004) 6, S. 33

[38] V. Holý, U. Pietsch, T. Baumbach, "High-Resolution X-Ray Scattering from Thin Films and Multilayers", Springer-Verlag, Berlin Heidelberg New York (1999)

[39] V. Wiedemeier, G. Berth, A. Zrenner, E. M. Larramendi, U. Woggon, K. Lischka, and D. Schikora, Semicond. Sci. Technol. **26**, 105023 (2011).

[40] G. Berth,W. Hahn, V.Wiedemeier, A. Zrenner, S. Sanna, and W. G. Schmidt, Ferroelectrics **420**(1), 44–48 (2011).

[41] C. Thomsen, H. T. Grahn, H. J. Maris, and J. Tauc, Opt. Commun. **60**, 55 (1986).

[42] B. C. Daly, K. Kang, Y. Wang, and D. G. Cahill, Phys. Rev. B **80**, 174112 (2009).

[43] T. Czerniuk, T. Ehrlich, T. Wecker, D.J. As, D.R. Yakovlev, A.V. Akimov, M. Bayer: Phys. Rev. Appl. **7**, 014006 (2017)

[44] P. Y. Yu and M. Cardona, Fundamentals of Semiconductors, 3rd edition (Springer, Berlin, Heidelberg, New York, 2005).

[45] D. Gardiner,H. Bowley, P. Graves, D. Gerrard, J. Louden, and G. Turrell, Practical Raman Spectroscopy (Springer, Berlin, Heidelberg, 2012).

[46] T. Frey, D. J. As, M. Bartels, A. Pawlis, K. Lischka, A. Tabata, J. R. L. Fernandez, M. T. O. Silva, J. R. Leite, C. Haug, and R. Brenn, J. Appl. Phys. **89**, 2631 (2001).

[47] H. Morkoc, Handbook of Nitiride Semiconductors and Devices (Wiley-VCH, Weinheim, 2008).

[48] R. H. Lyddane, R. G. Sachs, and E. Teller, Phys. Rev. **59**, 673–676 (1941).

[49] Y. A. Pusep, M. T. O. Silva, J. R. L. Fernandez, V. A. Chitta, J. R. Leite, T. Frey, D. J. As, D. Schikora, and K. Lischka, J. Appl. Phys. **91**, 6197 (2002).

[50] T. Kozawa, T. Kachi, H. Kano, Y. Taga, M. Hashimoto, N. Koide, and K. Manabe, J. Appl. Phys. **75**, 1098 (1994).

[51] H. Harima, S. Nakashima, and T. Uemura, J. Appl. Phys. **78**, 1996 (1995).

[52] E. Martinez-Guerrero, E. Bellet-Amalric, L. Martinet, G. Feuillet, B. Daudin, H. Mariette, P. Holliger, C. Dubois, C. Bru-Chevallier, P. Aboughe Nze, T. Chassagne, G. Ferro, and Y. Montei, J. Appl. Phys. **91**, 4983 (2002).

[53] A. Trampert, O. Brandt, H. Yang, and K. H. Ploog, Appl. Phys. Lett. **70**, 583 (1997).

[54] H. Okumura, K. Ohta, G. Feuillet, K. Balakrishnan, S. Chichibu, H. Hamaguchi, P. Hacke, and S. Yoshida, J. Cryst. Growth **178**, 113–133 (1997).

[55] D. Wang, Y. Hiroyama, M. Tamura, M. Ichikawa, and S. Yoshida, J. Cryst. Growth **220**, 204–208 (2000).

[56] H. Yang, O. Brandt, and K. Ploog, J. Electron. Mater. **25**(5), 787 (1996).

[57] B. Daudin, G. Feuillet, J. Hbner, Y. Samson, F. Widmann, A. Philippe, C. Bru-Chevallier, G. Guillot, E. Bustarret, G. Bentoumi, and A. Deneuville, J. Appl. Phys. **84**, 2295 (1998).

[58] H. Yang, L. X. Zheng, J. B. Li, X. J. Wang, D. P. Xu, Y. T. Wang, X. W. Hu, and P. D. Han, Appl. Phys. Lett. **74**, 2498 (1999).

[59] D. J. As, Proc. SPIE **7608**, 76080G (2010).

[60] J. Schörmann, S. Potthast, D. J. As, and K. Lischka, Appl. Phys. Lett. **90**, 041918 (2007).

[61] C. Hänel and G. Gauglitz, Anal. Bioanal. Chem. **372**, 91–100 (2002).

[62] H. Siegle, L. Eckey, A. Hoffmann, C. Thomsen, B. Meyer, D. Schikora, M. Hankeln, and K. Lischka, Solid State Commun. **96**(12), 943–949 (1995).

[63] O. Matsuda, M. C. Larciprete, R. L. Voti, and O. B. Wright, Ultrasonics **56**, 3 (2015).

[64] P. Babilotte, P. Ruello, D. Mounier, T. Pezeril, G. Vaudel, M. Edely, J.-M. Breteau, V. Gusev, and K. Blary, Phys. Rev. B **81**, 245207 (2010).

[65] O. Matsuda, T. Tachizaki, T. Fukui, J. J. Baumberg, and O. B. Wright, Phys. Rev. B **71**, 115330 (2005).

[66] A. V. Akimov, A. V. Scherbakov, D. R. Yakovlev, C. T. Foxon, and M. Bayer, Phys. Rev. Lett. **97**, 037401 (2006).

[67] D. Moss, A. V. Akimov, R. P. Campion, M. Henini, C. T. Foxon, L. Eaves, A. J. Kent, and B. A. Glavin, Phys. Rev. B **83**, 245303 (2011).

[68] C.-K. Sun, J.-C. Liang, and X.-Y. Yu, Phys. Rev. Lett. **84**, 179 (2000).

[69] D. Moss, A. V. Akimov, S. V. Novikov, R. P. Campion, C. R. Staddon, N. Zainal, C. T. Foxon, and A. J. Kent, J. Phys. D **42**, 115412 (2009).

[70] Chuan He, Martin Grossmann, Delia Brick, Martin Schubert, Sergei V. Novikov, C. Thomas Foxon, Vitalyi Gusev, Anthony J. Kent, and Thomas Dekorsy, Appl. Phys. Lett. **107**, 112105 (2015).

[71] K.-H. Lin, C.-M. Lai, C.-C. Pan, J.-I. Chyi, J.-W. Shi, S.-Z. Sun, C.-F. Chang, and C.-K. Sun, Nat. Nanotechnol. **2**, 704 (2007).

[72] D. M. Moss, A. V. Akimov, B. A. Glavin, M. Henini, and A. J. Kent, Phys. Rev. Lett. **106**, 066602 (2011).

[73] T. Czerniuk, PhD Thesis, TU Dortmund (2017)

[74] C. Thomsen, H. T. Grahn, H. J. Maris, and J. Tauc, Phys. Rev. B **34**, 4129 (1986).

[75] D. Bouguenna, A. Boudghene Stambouli, N. Mekkakia Maaza, A. Zado, and D.J. As, Superlattices and Microstructures **62**, 260 (2013)

[76] M. Birkholz, "Thin Film Analysis by X-Ray Scattering", Wiley-VCH Verlag (2006)

[77] M. Landmann, E. Rauls, W. G. Schmidt, M. Röppischer, C. Cobet, N. Esser, T. Schupp, D. J. As, M. Feneberg, and R. Goldhahn, Phys. Rev. B **87**, 195210 (2013).

[78] D.V. O'Connor, W. R. Ware, and J. C. Andre, J Phys Chem **83**, 1333–1343 (1979).

[79] D. Y. Oberli, Jagdeep Shah, T.C. Damen, J. M. Kuo, J. E. Henry, Jenifer Lary and Stephen M. Goodnick, Appl. Phys. Lett. **56** (13) (1990).

[80] H. W. Liu, R. Ferreira, G. Bastard, C. Delalande, J. F. Palmier, and B. Etienne, Appl. Phys. Lett. **54**, 2082 (1989).

[81] R. Ferreira, P. Rolland, P. Roussignol, C. Delalade, A. Vinattieri, L. Carraresi, M. Colocci, N. Roy, B.Sermage, J. F. Palmier, B. Etienne, Phys. Rev. B, **45** (20) (1992).

[82] F. C. Michl, R. Winkler and U. Rössler, Solid State Communications, Vol. **99**, No. 1, pp. 13-18 (1996).

[83] M. Nido, M.G.W. Alexander, K. Reimann, K. Ploog, W.W. Rühle, Surface Science **229**, 195-198 (1990).

[84] S. Haacke, N. T. Pelekanos, H. Mariette, M. Zigone, A.P. Heberle, and W.W. Rühle, Phys. Rev. B. **47**, 24 (1993).

[85] Mee-Yi Ryu, Phil Won Yu, Eun-joo Shin, Joo In Lee, Sung Kyu Yu, Eun Soon Oh, Yong Jo Park, Hyeong Soo Park, and Tae Ill Kim, Journal of the Korean Physical Society, Vol. **37**, No. 4 (2000).

[86] Eun-joo Shin, N. W. Song, J. I. Lee, D. Kim, M. Y. Ryu, P. W. Yu, D. Lee, Y.-H-Choi, C.-H. Hong, Journal of the Korean Physical Society, Vol. **34** (1990).

[87] E. O. Kane, J. Phys. Chem. Solids **1**, 249 (1957).

[88] C. Wetzel, R. Winkler, M. Drechsler, B. K. Meyer, U. Rössler, J. Scriba, J. P. Kotthaus, V. Härle, and F. Scholz, Phys. Rev. B **53**, 1038 (1996).

[89] P. Rinke, M. Winkelnkemper, A. Qteish, D. Bimberg, J. Neugebauer, and M. Scheffler, Phys. Rev. B **77**, 075202 (2008).

[90] M. Röppischer, Dissertation, Fakultät für Mathematik und Naturwissenschaften, TU Berlin, Berlin (2011).

[91] M. Luysberg, M. Heggen, K. Tillmann, JLSRF **2** (2016) 138.

[92] M. Tchernycheva, L. Nevou, L. Doyennette, F.H. Julien, E. Warde, F. Guillot, E. Monroy, E. Bellet-Amalric, T. Remmele, M. Albrecht, Phys. Rev. B **73** (2006) 125347.

[93] A. Helman, M. Tchernycheva, A. Lusson, E. Warde, F.H. Julien, Kh Moumanis, G. Fishman, E. Monroy, B. Daudin, D. Le Si Dang, E. Bellet-Amalric, D. Jalabert, Appl. Phys. Lett. **83** (2003) 5196.

[94] X.Y. Liu, P. Holmstrm, P. Jnes, L. Thyln, T.G. Andersson, Phys. Status Solidi (a) **244** (2007) 2892.

[95] T. Unuma, M. Yoshita, T. Noda, H. Sakaki, H. Akiyama, J. Appl. Phys., Vol. **93**, No 3 (2003)

[96] L. C. de Carvalho, A. Schleife, F. Bechstedt, Phys. Rev. B **84,** 195105 (2011).

[97] M.P.C.M. Krijn, Sci. Technol. **6**, 27 (1991)

[98] MadMax (c) 2001-2005 Oliver Brandt, Patrick Waltereit, Martin Kästner, and Daniel Schaadt.

[99] V. Cimalla, J. Pezoldt, and O. Ambacher, „Group III nitride and SiC based MEMS and NEMS: materials properties, technology and appli-cations“, J. Phys. D: Appl. Phys. **40**, 6386(2007).

[100] T. Schupp, K. Lischka, and D.J. As, J. Crystal Growth **312**, 1500 (2010)

[101] D. Windisch and P. Beckers, phys. stat. sol. (a) **118**, 379 (1990)

[102] In h-AlN the difference in the energy gap from 0 K to 300 K is about 67 meV [106][107]. A similar value for c-AlN is assumed leading to $E_{gap,\ 0K} = E_{gap,\ 300K} + 67$ meV.

[103] M. Röppischer, R. Goldhahn, G. Rossbach, P. Schley, C. Cobet, N. Esser, T. Schupp, K. Lischka, and D.J. As, J.Appl. Phys. **106**, 076104 (2009)

[104] A. F. Wright, J. Appl. Phys. **82**, 2833 (1997)

[105] C. G. V. de Walle and J. Neugebauer, Appl. Phys. Lett. 70, 2577 (1997).

[106] M. Feneberg, M. F. Romero, M. Röppischer, C. Cobet, N. Esser, B. Neuschl, K. Thonke, M. Bickermann, and R. Goldhahn, Phys. Rev. B **87**, 235209 (2013)

[107] I. Vurgaftman and J.R. Meyer, J. Appl. Phys. **94**, 3675 (2003).

[108] P. Schley, R. Goldhahn, C. Napierala, G. Gobsch, J. Schörmann, D. J. As, K. Lischka, M. Feneberg and K. Thonke, Semicond. Sci. Technol. **23**, 055001 (2008)

7.3 Abbildungsverzeichnis

Figure 2.1 *Excitonic binding energies for excitons consisting of e-hh and e-lh. The dotted lines correspond to complex simulations and the straight lines are calculated by the fractal dimensional method. In the left side the Al content in the barriers is 15% and on the right 30% [21].* *11*

Figure 2.2 *For real QWs the wave functions of the carriers penetrate into the barrier. Furthermore the allowed transitions follow the selection rule* $\Delta n_{inter} = 0,2,4,6$ *13*

Figure 2.3 *Scheme of the conduction band of an ADQW. The important parameters for tunnelling are the barrier height V and the barrier thickness d.* *13*

Figure 2.4 *Band diagram of an ADQW with a thin barrier. The Fermi energy* E_F *is slightly above the first electron level caused by doping.* *16*

Figure 2.5 *Sketch of a waveguide used for absorption measurements. Multiple passes through the MQWs are achieved by total reflection. The layer thicknesses are not to scale.* *17*

Figure 2.6 *Trend of the band offsets for a GaN/*$Al_xGa_{1-x}N$ *interface partially strained on a c-GaN buffer layer for various Al concentrations in the* $Al_xGa_{1-x}N$ *barrier layers. (Provided by Marc Landman in University of Paderborn)* *19*

Figure 2.7 *Bandgap of relaxed cubic* $AlxGa1-xN$ *for different Al content. There is a change from direct* $\Gamma V - \Gamma C$ *(red) to indirect bandgap* $\Gamma V - XC$ *(blue) at* $x = 0.71$ *[77].* *20*

Figure 3.1 *Schematic picture of the used Riber 32 PA-MBE [32].* *21*

Figure 3.2 *Representation of the basic principle of the RHEED measurement. Also the geometries of the different beams in regard to the sample can be seen.* *22*

Figure 3.3 *Sketch of the UV PL setup. The excitation light is focused on the sample placed in a cryostat reaching 13 K. The detection is done by a monochromator with photomultiplier and CCD attached.* *23*

Figure 3.4 *Illustration of the complex optical setup. With this setup PL, PLE and TRPL measurements can be done. (AG Hoffmann TU Berlin)* *24*

Figure 3.5 *The important optical components in the HRXRD setup are the Cu source and a four crystal monochromator which filters the* $K_{\alpha 1}$ *line. The detection is accomplished with a CCD array.* *26*

Figure 3.6 *Schematic overview of the diffraction spots in reciprocal space. The excitation is done with an angle of ω and the detection angle is 2θ [37].* *26*

Figure 3.7 *Visualization of the (113) plain important for strain measurements.* *28*

Figure 3.8 *Sketch of the absorption setup used for the IR absorption measurements. (AG Betz TU Dortmund)* *29*

Figure 3.9 *Sketch of the μ-Raman setup. The sample is excited with a Nd:YAG CW laser (532 nm). The detection is done by a holographic grating spectrometer with an applied CCD camera. (AG Zrenner Paderborn)* *30*

Figure 3.10 *Sketch of the pump probe setup for measuring picosecond acoustics. (AG Bayer TU Dortmund)* *31*

Figure 3.11 *Sketch of the pump probe setup for measuring intraband non-linearity. (AG Betz TU Dortmund)* *32*

Figure 4.1 *Omega profile of the thickest sample GNW2345 (505 nm) and the thinnest sample GNW2350 (75 nm). A clear decrease of the FWHM for the 505 nm thick sample can be seen. 35*

Figure 4.2 *A comparison of Raman spectra of a 3C-SiC/Si substrate piece (dashed) and a thick c-GaN layer (red) reveals two additional peaks (marked in red). These peaks are attributed to the TO and LO mode of c-GaN. (Measured in University of Paderborn by Michael Rüsing) 36*

Figure 4.3 *Raman spectroscopy enables another way to measure the thickness of layers. A linear correlation between the integrated intensity, given by the area underneath the LO Raman line A, of the LO mode and the layer thickness of c-GaN bulk layers can be seen. (Evaluation done together with Michael Rüsing) 37*

Figure 4.4 *A linear correlation between the dislocation density D via HRXRD and Raman FWHM* $\boldsymbol{\Delta\nu}$ *is found. These data can be used as a calibration to determine the dislocation density with Raman only. (Evaluation done together with Michael Rüsing) 38*

Figure 4.5 *Single QW structure consisting of a 10 nm thick c-GaN QW and 35 nm thick c-* $Al_xGa_{1-x}N$ *barriers. Two samples are investigated with different Al content of 0.1 (GNW2446) and 0.8 (GNW2448).....40*

Figure 4.6 *PL spectra for the reference c-GaN sample (GNW2424) and the QW structure with* $Al_{0.8}Ga_{0.2}N$ *(GNW2448) at low temperature. The excitation was done with a Nd:YAG laser emitting at 266 nm with 5 mW. (Measured in University Paderborn by me) 40*

Figure 4.7 *Measured acoustic signal (dashed lines) and simulated signal (straight lines) for the sample with x = 0.8 (GNW2248) for three different probe wavelengths. The pump power was increased from* W_0 *(left) to* $4W_0$ *(right). The parameter β represents the ratio of the photo elastic coupling efficiency of the QW over the one of the bulk layer. (Measured in TU Dortmund by Thomas Czerniuk) [73].....42*

Figure 4.8 *Sample structure of the two ADQW series. The barrier thickness d was varied from 1 nm to 15 nm. In series 0.26 (left) the Al content is x = 0.26 ± 0.03 and for series 0.64 (right) the Al content is x = 0.64 ± 0.03. .....44*

Figure 4.9 *RSM of the (113) reflection of two cubic GaN/*$Al_xGa_{1-x}N$ *ADQW with d = 15 nm of the two different series. A partial strain of the barriers is visible in both measurements. (Left) An Al content of x = 0.25 ± 0.03 is determined. (Right) The Al content is x = 0.62 ± 0.03. 45*

Figure 4.10 *Low temperature PL spectrum of the cubic GaN/*$Al_{0.26}Ga_{0.74}N$ *ADQW with d = 15 nm excited with a Nd:YAG laser (266 nm). 46*

Figure 4.11 *Semi-logarithmic plot of the low temperature (7 K) PL spectra of the cubic GaN/* $Al_xGa_{1-x}N$ *ADQWs with x = 0.26 (left) and x = 0.64 (right). Three emission bands are visible for the wide QW (*QW_W*), the narrow QW (*QW_N*) and the* $Al_xGa_{1-x}N$ *barriers. The emission intensity of the narrow QW can be correlated to the barrier thickness d. (right: measured in TU Berlin together with Gordon Callsen) 47*

Figure 4.12 *Intensity ratio* I_N/I_W *as a function of barrier thickness d for series 0.26 (left) and series 0.64 (right). The calculated curves for electrons (e) (blue line) and heavy holes (hh) (red line) follow the same trend as the measured ratios (dots). (Evaluation done by me) 48*

Figure 4.13 *Simulated conduction band of the cubic GaN/*$Al_xGa_{1-x}N$ *ADQW with x = 0.26 and a barrier thickness d = 1 nm (left) and d = 5 nm (right) at 13 K.....50*

Figure 4.14 *Valence bands as simulated by nextnano³ of the heavy holes (hh, blue) and light holes (lh, red) in case of the cubic GaN/*$Al_xGa_{1-x}N$ *ADQW with x = 0.26 and a barrier thickness d = 1 nm (left) and d = 5 nm (right) at 13 K. For clarity only the probability distribution* $\boldsymbol{\Psi^2}$ *for the hh is plotted. 51*

Figure 4.15 *Simulated energy levels for electrons (e), heavy holes (hh) and light holes (lh) of a single c-GaN QW with $Al_xGa_{1-x}N$ barriers (x = 0.26) partly strained on c-GaN buffer at 13 K.* *52*

Figure 4.16 *Transition energies of the 3 electron levels with the 3 heavy hole levels for the SQW with c-GaN QW and $Al_xGa_{1-x}N$ barriers (x = 0.26).* *52*

Figure 4.17 *Simulated energy levels for electrons (e), heavy holes (hh) and light holes (lh) of a single c-GaN QW with $Al_xGa_{1-x}N$ barriers (x = 0.64) partly strained on c-GaN buffer at 13 K.* *53*

Figure 4.18 *Transition energies of the 3 electron levels with the 3 heavy hole levels for the SQW with c-GaN QW and $Al_xGa_{1-x}N$ barriers (x = 0.64).* *53*

Figure 4.19 *Time transients for the ADQW of series 0.64 with the thickest barrier d = 15 nm measured at the QW_W (2.5 nm) emission at 7 K. A bi-exponential fit was used with a convolution approach to match the data. (measured in TU Berlin together with Gordon Callsen)* *55*

Figure 4.20 *Time transients for the 3 ADQW samples of series 0.64 measured at the QW_W (2.5 nm, left) emission and at the QW_N (1.35 nm, right) emission for the three samples with different barrier thickness d. (measured in TU Berlin together with Gordon Callsen)* ... *56*

Figure 4.21 *Decay time τ_{fast} of the QW_N (black) and QW_W (blue) emission corresponding to the barrier thickness d for low temperatures (7 K). The decay time increases for the wide QW due to additional electrons of the narrow QW for thinner barriers. The opposite behaviour takes place for the narrow QW. (evaluation done by me)* *57*

Figure 4.22 *Sample structure of the cubic $GaN/Al_{0.25}Ga_{0.75}N$ ADQW. The barrier thickness between the two QWs is 15 nm, thus the wells are uncoupled.* *58*

Figure 4.25 *(a) Semi-logarithmic plot of the low temperature photoluminescence (PL) spectrum of the cubic $GaN/Al_{0.25}Ga_{0.75}N$ ADQW at a temperature (T) of 7 K. The depicted rectangles illustrate the applied spectral window for the detection of the PLE measurements. (b) Furthermore, photoluminescence excitation (PLE) data for three different detection wavelengths with T = 7 K are shown, which correspond to the emission maxima of the PL spectrum (red for the QW_W, green for the QW_N, blue for the $Al_{0.25}Ga_{0.75}N$ barrier). (measured in TU Berlin together with Gordon Callsen)* *59*

Figure 4.26 *Detailed, semi-logarithmic plot of the low temperature photoluminescence excitation (PLE) spectrum detected at the emission maximum of the wide quantum well (QW_W) at a temperature (T) of 7 K. The narrow peak at 3.38 eV originates from an overlay of the excitation light and resonant sample luminescence. Furthermore, two transitions can be verified (e1-hh3 and e2-hh2) by a careful fitting routine. (measured in TU Berlin together with Gordon Callsen)* *60*

Figure 4.23 *Nextnano³ simulation of the energy levels and the band edges for the wide QW (3.15 nm) at 7 K. Two bound energy levels exist for the electrons (e), whereas the holes have five bound states, three for the heavy holes (hh) and two for the light holes (lh). This leads to 5 allowed transition.* *62*

Figure 4.24 *Simulation results via nextnano³ of the energy levels and the band edges of the narrow QW (0.9 nm) for 7 K. There is one bound energy level for every charge carrier (electrons (e), heavy holes (hh) and light holes (lh)). Thus two allowed transitions are predicted.* *63*

Figure 4.27 *Sample structure of two different types of MQW with 80 periods (left) and 40 periods (right) of GaN QWs and 1 nm AlN barriers and a homogeneous Si doping in the c-GaN QWs in the order of $N_{Si} \sim 10^{19}$ cm^{-3}.* *66*

Figure 4.28 *RHEED diffraction pattern taken after the first MQW cycle of sample GNW2460.....67*

Figure 4.29 *RHEED intensity profile of the first QW and second AlN layer of the MQW structure (GNW2460) measured in the red area in Figure 4.28. .....67*

Figure 4.30 *RSM in (113) direction of GaN/AlN MQW structures with 80 periods (left) and 40 periods (right).....69*

Figure 4.31 *RSM in (002) direction of GaN/AlN MQW structures with 80 periods (left) and 40 periods (right).....69*

Figure 4.32 *Sample structure of a MQW with 20 periods of 1.35 nm GaN QWs and 5 nm AlN barriers and a homogeneous Si doping in the c-GaN QWs in the order of $N_{Si} \sim 10^{19}$ cm^{-3}.....70*

Figure 4.33 *High resolution TEM micrograph of a MQW sample with 20 periods of 1.35 nm c-GaN and 5 nm AlN oriented along the <110> direction of the MQWs (measured in FZ Jülich together with Torsten Rieger) 71*

Figure 4.34 *TEM intensity contrast profile averaged over the yellow area in Figure 4.33. The medial QW thickness is (1.2 ± 0.1) nm and the medial thickness for the AlN barriers is (4.77 ± 0.46) nm. (the evaluation done by me).....72*

Figure 4.35 *PL spectra of MQW with 80 periods (red) and 40 periods (green, blue) grown on different substrates. 73*

Figure 4.36 *PL spectra of MQW with 40 (green), 50 (black) and 60 (red) periods of GaN/AlN. The spectrum of GNW2675 shows a higher noise, because of a lower integration time during the measurement.....74*

Figure 4.37 *PL spectra of MQW with 40 periods and different doping. The spectrum of GNW2675 shows a higher noise, because of a lower integration time during the measurement....74*

Figure 4.38 *IR absorption spectra of the two MQW samples at room temperature. The FWHM of GNW2460 is with 370 meV much broader than for GNW2675 (250 meV), caused by higher doping. For GNW2460 e1-e2 and e2-e3 is absorbing, leading to a broader spectrum. (measured in TU Dortmund AG Betz).....75*

Figure 4.39 *Band diagram of the sample with 80 periods (d_{QW} = 2.25 nm, left) and with 40 periods (d_{QW} = 1.8 nm, right) at 300 K.....76*

Figure 4.40 *Calculated ISBT of a single QW with a degree of relaxation of 0.25 and AlN barriers at 300K.....77*

Figure 4.41 *Simulated energy levels for electrons (e), heavy holes (hh) and light holes (lh) of a single c-GaN QW with AlN barriers partly strained on c-GaN buffer at 300 K. 78*

Figure 4.42 *Electron energy levels for a c-GaN/AlN QW provided by nextnano³ with a degree of relaxation of 0.5 at 300 K.....79*

Figure 4.43 *Influence of the QW thickness on the electron energy levels for a c-GaN/AlN QW. 80*

Figure 4.44 *Calculated absorption between e1-e2 for a single QW of 2.025 nm for two material systems (GaAs/AlAs blue, GaN/AlN red) for the correlation length $\Lambda = 4.3\,nm$ and the mean height $\Delta = 0.45\,nm$ of the roughness.....82*

Figure 4.45 *Absorption measurement of GNW2675 together with the calculated absorption (green). The calculation was performed with a correlation length $\Lambda = 0.53\,nm$ and a mean height $\Delta = 0.45\,nm$ of the roughness.....83*

Figure 4.46 *TEM Image of an MQW GNC2206 (provided by Christian Mietze)..... 84*

Figure 4.47 *Calculated FWHM of the absorption for various correlation lengths. The value of 0.54 nm fits best with the experimental FWHM of 250 meV. 84*

Figure 4.48 *Pump induced change of the transmission of the MQW for a central photon energy of 0.82 eV. The blue curve corresponds to TE polarized light (angle of incidence 65°). The black and red curves belong to the TM polarisation with different angle of incidences, as can be seen in the inset. (measured in TU Dortmund by Thorben Jostmeier) 85*

Figure 4.49 *The peak pump-probe signal for various pump irradiances (central photon energy 0.81 eV, TM polarisation, 65° angle of incidence). The red line is a linear fit. (measured in TU Dortmund by Thorben Jostmeier)..... 86*

Figure 5.1 *Part of the input file necessary for the strain implementation. The $strain_{AlGaN}$ is measured by HRXRD, to provide a virtual buffer layer lattice constant. 89*

Figure 5.2 *Input window of MadMax for a c-GaN reference sample. The c- $Al_xGa_{1-x}N$ layer is used to achieve the lattice constant of c-GaN. The GaAsN layer matches the lattice constant of the Si in the substrate. 90*

Figure 5.3 *MadMax output profile (black) with the measured ω-2θ profile of a c-GaN reference sample (red) in (002). The three peaks are caused by the Si, c-GaN and 3C-SiC, respectively. 91*

Figure 5.4 *Comparison of two ω-2θ measurements in the (002) direction. The green curve corresponds to a MQW sample and the blue curve to a wafer piece without any grown layer..... 92*

Figure 5.5 *Input window of MadMax for a MQW sample with 80 periods of 2.025 nm GaN and 1 nm AlN on top of a c-GaN buffer layer. This buffer layer provides a partial strain, which was achieved inserting a virtual $Al_xGa_{1-x}N$ layer with x = 0.35. ..... 93*

Figure 5.6 *ω-2θ measurement and simulation data in the (002) direction for a MQW sample with 80 periods. Three Gaussian fit curves explain the experimental data very well corresponding to the first SL peak, the c-GaN buffer layer and the second SL peak.... 93*

7.4 List of Conferences

Nr.	Conference	Destination	Date	Contribution
1	DPG 2013	Regensburg	10.03-15.03.2013	Talk
2	SFB 2014	Bad Sassendorf	27.11.-28.11.2014	Talk
3	DPG 2014	Dresden	30.03-04.04.2014	Talk
4	DMBE 2014	Darmstadt	15.09.-16.09.2014	Talk
5	IWN 2014	Poland, Breslau	23.08.-29.08.2014	Talk
6	SFB 1-2015	Bad Sassendorf	28.05.-29.05.2015	Poster
7	DMBE 2015	Paderborn	21.09.-22.09.2014	-
8	SFB 2-2015	Dortmund	26.11.-27.11.2015	Talk
9	ISGN6 2015	Japan, Hamamatsu	06.11.-08.11.2015	Talk + Poster
10	DPG 2016	Regensburg	06.03.-11.03.2016	Talk
11	SFB 2016	Dortmund	13.10.-14.10.2016	-
12	MBE 2016	France, Montpellier	03.09.-09.09.2016	Talk
13	DPG 2017	Dresden	19.03-24.03.2017	Poster
14	SFB 2017	Paderborn	14.02.-15.02.2017	Poster

7.5 List of Publications

Nr.	Publication	Ref. in this thesis
1	D.J. As, R.M. Kemper, C. Mietze, **T. Wecker**, J.K.N. Lindner, P. Veit, A. Dempewolf, F. Bertram, J. Christen, MRS Symp. Proc. Vol. **1736 E**, T3.03 (2014)	
2	R. M. Kemper, P. Veit, C. Mietze, A. Dempewolf, **T. Wecker**, F. Bertram, J. Christen, J. K. N. Lindner, and D. J. As, Phys. Status Solidi C **12**, No. 4–5, 469–472 (2015)	
3	**T. Wecker**, F. Hörich, M. Feneberg, R. Goldhahn, D. Reuter, and D. J. As, Phys. Status Solidi B **252**, 873 (2015).	[109]
4	T. Jostmeier, **T. Wecker**, D. Reuter, D. J. As, and M. Betz, Appl. Phys. Lett. **107**, 211101 (2015)	[110]
5	D. Bouguenma, **T. Wecker**, D.J. As, N. Kermas, A. Beloufa, J. of Computational Electronics, **15** 1 (2016)	
6	**T. Wecker**, T. Jostmeier, T. Rieger, E. Neumannn, A. Pawlis, M. Betz, D. Reuter, D.J. As, J. Crystal Growth (2016) in press	[111]
7	**T. Wecker**, G. Callsen, A. Hoffmann, D. Reuter and D. J. As, Jpn. J. Appl. Phys. **55**, 05FG01 (2016)	[112]
8	M. Rüsing, **T. Wecker**, G. Berth, D.J. As, and A. Zrenner, Phys. Stat. Sol. (b) **253**, 778 (2016)	[113]
9	T. Czerniuk, T. Ehrlich, **T. Wecker**, D.J. As, D.R. Yakovlev, A.V. Akimov, M. Bayer: Phys. Rev. Appl. **7**, 014006 (2017)	[114]
10	**T. Wecker**, G. Callsen, A. Hoffmann, D. Reuter, and D. J. As, submitted	[115]

7.6 Parameters

Parameter	c-GaN	c-AlN	c-InN
$E_{gap,\ 0K}$ [eV]	3.293[22]	5.997[102]	-
$E_{gap,\ 300K}$ [eV]	3.23[22]	5.93[103]	0.595[108]
$E_{exciton}$ [meV]	24[22]	-	-
a [Å]	4.503[35]	4.373[100]	5.01[108]
m_e^*/m_0	0.19[96]	0.3[96]	0.052[96]
m_{hh}^*/m_0	0.83[96]	1.32[96]	0.91[96]
m_{lh}^*/m_0	0.28[96]	0.44[96]	0.079[96]
m_{so}^*/m_0	0.34[96]	0.55[96]	0.11[96]
Δ_{so} [meV]	15[22]	19[96]	5[96]
ϵ_r	9.44[22]	8.07[103]	12.3[108]
ϵ_∞	5.31[22]	4.25[103]	7.84[108]
c_{11} [GPa]	293[104]	304[104]	187[104]
c_{12} [GPa]	159[104]	160[104]	125[104]
c_{44} [GPa]	155[104]	193[104]	86[104]
a_g [eV]	-8.0[105]	-9.1[105]	-5.0[105]
$a_c=a_g+a_v$ [eV]	-6.0	-6.8	-3.3
a_v [eV]	2.0[105]	2.3[105]	1.7[105]
b_{uniax} [eV]	-1.7[105]	-1.5[105]	-1.2[105]
b_{Bowing}^{direct} [eV]	0.85[77]		
$b_{Bowing}^{indirect}$ [eV]	0.01[77]		

Background n-type doping of around $5x10^{17}$ cm^{-3} in $Al_xGa_{1-x}N$ and of around $1x10^{17}$ cm^{-3} in GaN [75].

Lattice constant 3C-SiC: 4.3596 Å [99]

7.7 Nextnano³ Source Code

Here the Nextnano³ source code for a MQW c-GaN/c-AlN structure with 1.8 nm thick QWs is shown.

```
!%&CBO angepasst für Al=1%&
!****** OVERALL SIMULATION PARAMETERS ************************************!
!&macro filename = 'macro.in'
!Einschalten der Makrofunktion
%FunctionParser = yes

!Die Dicken der einzelnen Schichten des ADQW
%Barrier1 = 3 !%&Barrier1%&
%QW = 1.8    !%&QWw%&

%piezo_AlGaN = 0E0
%piezo = 0E0

!Automatisierung für die Erstellung der Simulationsbereiche
%region1 = %Barrier1 + %QW
%domain  = %Barrier1 + %QW + %Barrier1

%AlGehalt = 1 !%&AlGehalt%&

%Temperatur = 300E0
%Strain_status = 0.25E0 ! 1= pseudomorph
%Strain_qw = 1-%Strain_status

%g_AlN = 0.4373E0
%g_GaN = 0.4503E0

%dop_AlGaN = 0.5E0          ! 150 * 10^18 cm^-3 = 1.5 * 10^20 cm^-3
%dop_GaN   = 0.1E0

%g_rel_AlGaN = %g_AlN*%AlGehalt +%g_GaN*(1-%AlGehalt)       !Gitterkonstante [nm]
!%g_AlGaN = (1-%Strain_status) * %g_GaN+ %Strain_status* %g_rel_AlGaN
%g_AlGaN = %g_rel_AlGaN
%g_Buffer = (1-%Strain_qw) * %g_GaN+ (%Strain_qw)* %g_rel_AlGaN

!Vorgaben für die Energien der Bänder
%CBO = 78 !%&CBO%&
%VBO = 100-%CBO
!%E_GaN = 3.293+0.0057 !13K %&Temperatur GaN 13K %&
!%E_AlN = 5.997 +0.0063 !13K %&Temperatur AlN 13K %&
%E_GaN = 3.24+0.006 !300K %&Temperatur GaN 300K %&
%E_AlN = 5.93 !300K %&Temperatur AlN 300K %&
!%E_AlN = 5.3 !300K indirekt %&Temperatur AlN 300K %&
%b = -0.85 !Bowing Parameter

%GaN_VB = -0.726
%GaN_LB = %E_GaN+%GaN_VB

%E_AlGaN = %E_GaN*(1-%AlGehalt) + %E_AlN*%AlGehalt + %b*%AlGehalt *(1-%AlGehalt)
%DeltaE = %E_AlGaN - %E_GaN
%Leitunsgband_AlGaN = %DeltaE *%CBO/100 +%GaN_LB
%Valenzband_AlGaN = -%DeltaE *%VBO/100+%GaN_VB

!Effektive Massen der beteiligten Binären Halbleiter
%mass_eGaN = 0.19E0 !Carvalho Phys Rev B 84, 195105 (2011)
%mass_eAlN = 0.30E0 !Carvalho Phys Rev B 84, 195105 (2011)
```

```
%mass_hhGaN = 0.83E0 !Carvalho Phys Rev B 84, 195105 (2011)
%mass_hhAlN = 1.32E0 !Carvalho Phys Rev B 84, 195105 (2011)
%mass_lhGaN = 0.28E0 !Carvalho Phys Rev B 84, 195105 (2011)
%mass_lhAlN = 0.44E0 !Carvalho Phys Rev B 84, 195105 (2011)
%mass_SOGaN = 0.34E0 !Carvalho Phys Rev B 84, 195105 (2011)
%mass_SOAlN = 0.55E0 !Carvalho Phys Rev B 84, 195105 (2011)

!GaN Parameters
%c11_GaN = 293E0 !Elastizitätskoeffizienten
%c12_GaN = 159E0
%c44_GaN = 155E0
%GaN_splitt_off = 0.015E0
%av_GaN = 2E0
%ac_GaN = -6E0
%uniaxial_GaN = -1.7E0

!Die wesentlichen Paramter werden linear zwischen AlN und GaN interpoliert
%lb_mass1 = %mass_eAlN*%AlGehalt + %mass_eGaN*(1 - %AlGehalt)          !Elektronenmasse
%vb_mass1 = %mass_hhAlN*%AlGehalt + %mass_hhGaN*(1 - %AlGehalt)          !hh Masse
%vb_mass2 = %mass_lhAlN*%AlGehalt + %mass_lhGaN *(1 - %AlGehalt)          !lh Masse
%vb_mass3 = %mass_SOAlN*%AlGehalt + %mass_SOGaN*(1 - %AlGehalt)          !Splitt Off Masse
%c11_AlGaN = 304*%AlGehalt +%c11_GaN*(1-%AlGehalt)              !Elastizitätskoeffizienten
%c12_AlGaN = 160*%AlGehalt +%c12_GaN*(1-%AlGehalt)
%c44_AlGaN = 193*%AlGehalt +%c44_GaN*(1-%AlGehalt)
%splitt_off = 0.019*%AlGehalt +%GaN_splitt_off*(1-%AlGehalt)         !Splitt Off Energie [eV]
%av_AlGaN = 2.3*%AlGehalt +%av_GaN*(1-%AlGehalt)              !Deformationspotential Valenzband [eV]
%ac_AlGaN = -6.8*%AlGehalt +%ac_GaN*(1-%AlGehalt)           !Deformationspotential Leitungsband [eV]
%uniaxial_AlGaN = -1.5 *%AlGehalt -%uniaxial_GaN*(1-%AlGehalt)       !Deformationspotential Uniaxiale Verspannung
Valenzband [eV]

$numeric-control
 simulation-dimension         = 1               ! only simulate directions in which charge carriers are bound, therefore 1D
simulation for a quantum well
 zero-potential               = no              ! don't consider charge redistribution
 varshni-parameters-on        = no              ! don't consider temperature dependence of band gap
 lattice-constants-temp-coeff-on      = no        ! temperature dependent lattice constants
 nonlinear-poisson-cg-lin-eq-solv     = lapack-full  !??

! 1) => effective-mass, finite-differences, lapack                    !
 schroedinger-1band-ev-solv          = lapack                        ! 'lapack', 'laband', 'arpack', 'davids', 'it_jam', 'chearn' ??
!schroedinger-masses-anisotropic      = no                            ! 'yes', 'no', 'box'

 8x8kp-params-from-6x6kp-params      = yes                            !
 8x8kp-params-rescale-S-to          = no                            ! NO, ONE, ZERO ???????????
 varshni-parameters-on = no                                         ! Temperature dependent energy gaps.
! 1D/2D/3D  ! Band gaps independent of temperature. Absolute values from database are taken.
 lattice-constants-temp-coeff-on = no                               ! Lattice constants independent of temperature. Absolute
values from database are taken.
$end_numeric-control
$simulation-dimension
 dimension   = 1                                                    ! 1D simulation
 orientation = 0 0 1                                                ! along z axis (as defined below)
$end_simulation-dimension                                           !

$global-parameters                                                  !
 lattice-temperature = %Temperatur                                          ! 300 Kelvin
$end_global-parameters                                              !

$simulation-flow-control
 flow-scheme        = 2                                             !2 = self-consistent Schroedinger-Poisson
 !flow-scheme       = 3                                             ! solve Schroedinger equation only
```

```
!(because no charge redistribution here) raw-strain-in  or  homogeneous-strain  or  strain-minimization  or  zero-strain-
amorphous
!raw-directory-in    = raw_data1/
!raw-potential-in    = no                                    !
 strain-calculation  = homogeneous-strain! homogeneous-strain  or  strain-minimization  or  zero-strain-amorphous
$end_simulation-flow-control                                  !

$domain-coordinates                                           !
 domain-type          = 0 0 1                                 ! again: along z axis
 z-coordinates        = 0d0 %domain ! beginning and end of simulated region in nm
 !z-coordinates       = 0d0 8d0
 growth-coordinate-axis = 0 0 1                                ! needed if pseudomorphic strain is to be calculated
 pseudomorphic-on     = GaN(zb)! needed if pseudomorphic strain is to be calculated
 lattice-constants          = %g_Buffer %g_Buffer %g_Buffer
lattice-constants-temp-coeff       = 5.59d-6    5.59d-6     5.59d-6   ! [nm/K] http://www.ioffe.ru/SVA/NSM/
$end_domain-coordinates                                       !
!****** REGIONS AND CLUSTERS ************************************************!
$regions                                                      !
region-number = 1    base-geometry = line    region-priority = 2    z-coordinates = 0d0       %Barrier1       !Material: Barri-
ere
region-number = 2    base-geometry = line    region-priority = 2    z-coordinates = %Barrier1  %region1        !Material: QW
region-number = 3    base-geometry = line    region-priority = 2    z-coordinates = %region1   %domain         !Material:
Barrier
$end_regions                                                  !

$grid-specification                                           ! for every boundary between regions, there has to exist a grid line
grid-type       =    0 0 1                                    ! again: along z axis
z-grid-lines    =    0d0    %Barrier1   %region1   %domain ! explicity specified grid lines
z-nodes         =    300    300         300                    ! number of additional grid lines between those
z-grid-factors  =    1d0    1d0         1d0                    ! can be used for inhomogeneous grids
$end_grid-specification
! You specified n regions in the simulation area. If they do not          !
! completely fill the simulation area, the resulting rest area is         !
! automatically assigned as region number n+1.                            !

$region-cluster                          ! regions can be grouped into clusters
 cluster-number = 1    region-numbers = 1 3 4 ! Barrieren
 cluster-number = 2    region-numbers = 2     ! Quantentopf
$end_region-cluster
!****** MATERIALS AND ALLOY PROFILES ****************************************
$material
 material-number = 1
 material-name   = AlN(zb)                    ! AlGaN
 cluster-numbers = 1
 crystal-type    = zincblende

 material-number = 2
 material-name   = GaN(zb)         ! QW
 cluster-numbers = 2
$end_material

!****** DOPING AND IMPURITIES ************************************************!
$doping-function                                              !
 doping-function-number     = 1                                !
 impurity-number          = 1                                 ! properties of this impurity type have to be specified below
 doping-concentration       = 0d0                               ! 150 * 10^18 cm^-3 = 1.5 * 10^20 cm^-3
 only-region              = 0d0 %region1
 !only-region             = 0d0 2.5d0
$end_doping-function                                          !

$impurity-parameters                                          !
```

```
! n-Si in GaAs              = 0.0058d0                    !
! n-Si in AlAs              = 0.007d0                     ! 300 K, Landolt-Boernstein
! p-C in GaAs               = 0.027d0

 impurity-number            = 1                           ! impurity numbers labelled in doping-function
 impurity-type              = n-type                      ! n-type, p-type
 number-of-energy-levels    = 1                           ! number of energy levels of this impurity (only 1 is currently allowed)
 energy-levels-relative     = 0.02d0                      ! energy relative to 'nearest' band edge (n-type -> conduction
band, p-type -> valence band)
!energy-levels-relative     = -1000d0  ! = all ionized    ! energy relative to 'nearest' band edge (n-type -> conduc-
tion band, p-type -> valence band)
 degeneracy-of-energy-levels  = 2                         ! degeneracy of energy levels, 2 for n-type, 4 for p-type

! impurity-number            = 2                           ! impurity numbers labelled in doping-function
! impurity-type              = n-type                      ! n-type, p-type
! number-of-energy-levels    = 1                           ! number of energy levels of this impurity (only 1 is currently allowed)
! energy-levels-relative     = 0.006d0                     ! energy relative to 'nearest' band edge (n-type -> conduction
band, p-type -> valence band)
!energy-levels-relative     = -1000d0  ! = all ionized    ! energy relative to 'nearest' band edge (n-type -> conduc-
tion band, p-type -> valence band)
! degeneracy-of-energy-levels  = 2                         ! degeneracy of energy levels, 2 for n-type, 4 for p-type
$end_impurity-parameters
!****** QUANTUM *************************************************************!
$quantum-regions                                          ! Schroedinger equation is only solved inside this region(s)
 region-number          = 1                               ! usually only one simulation region
 base-geometry          = line                            !
 region-priority        = 3                               !
 z-coordinates          = 0d0 %domain                     ! can also be smaller than total simulation region
$end_quantum-regions                                      !
$quantum-cluster                                          ! again: regions can be grouped into clusters
 cluster-number         = 1
 region-numbers         = 1
 deactivate-cluster     = no
$end_quantum-cluster                                      !
$quantum-model-electrons                                  ! how to solve Schroedinger equation for electrons
 model-number                   = 1                       !
 model-name                     = effective-mass          ! quantum model, here: single band effective mass approximation
 cluster-numbers                = 1                       ! quantum cluster numbers to which this model applies
 conduction-band-numbers        = 1                       ! select conductions bands (minima), here: only gamma point
 number-of-eigenvalues-per-band = 4                       ! how many eigenenergies are calculated for each band
 separation-model               = eigenvalue              ! to determine separation between classic and quantum density
 maximum-energy-for-eigenstates = 1d0                     ! has to be present but is ignored in separation model
"eigenvalue"
 quantization-along-axes        = 0 0 1                   ! directions in which charge carriers are quantized, here: same
as simulation direction
 boundary-condition-100         = Neumann                 ! mixed, Neumann or (Dirichlet|dirichlet|DIRICHLET).
Nonsens input means Neumann (default).
 boundary-condition-010         = Neumann                 ! mixed, Neumann or (Dirichlet|dirichlet|DIRICHLET).
Nonsens input means Neumann (default)
 boundary-condition-001         = Neumann                 ! periodic boundary conditions are necessary for superlattices
$end_quantum-model-electrons
$quantum-model-holes
 model-number                   = 1                       !
 model-name                     = effective-mass          ! quantum model, here: single band effective mass approximation
 cluster-numbers                = 1                       ! quantum cluster numbers to which this model applies
 valence-band-numbers           = 1 2 3                   ! select valence bands (maxima), 1 = heavy holes, 2 = light
holes, 3 = split-off holes
 number-of-eigenvalues-per-band = 3 3 3                   ! how many eigenenergies are calculated for each band
 separation-model               = eigenvalue              ! to determine separation between classic and quantum density
 maximum-energy-for-eigenstates = 1d0 1d0 1d0             ! has to be present but is ignored in separation model
"eigenvalue"
```

```
 quantization-along-axes              =  0 0 1                    ! directions in which charge carriers are quantized, here: same
as simulation direction
 boundary-condition-001               =  Neumann                  ! finite barrier .... infinite => Dirichlet
$end_quantum-model-holes
$binary-zb-default
  binary-type                    =AlN(zb)-zb-default!
 apply-to-material-numbers          =1
 conduction-band-masses             =%lb_mass1   %lb_mass1   %lb_mass1   ! [m0] ml,mt1,mt2 for each band. Ordering of
numbers corresponds to band no. 1, 2, ... (Gamma, L, X)
                                 0.200000D+00   0.200000D+00   0.200000D+00    ! [m0]
                                 0.530000D+00   0.310000D+00   0.310000D+00    ! [m0]

!conduction-band-energies           = 4.624d0  7.721d0  3.321d0                 ! direct gap Eg=5.9 eV (Goldhahn)
!conduction-band-energies           = 3.979d0  7.780d0  3.380d0    !   indirect gap for SL calculations CBO 1.4 eV
Eg=5.255 eV (Goldhahn)
 conduction-band-energies           = %Leitunsgband_AlGaN   7.78d0  3.38d0  !0K
!conduction-band-energies           = 4.480d0  7.780d0  3.380d0    !   0K  Vurgaftman1  conduction band edge energies
relative to valence band number 1 (number corresponds
!conduction-band-energies           = 4.421d0  7.721d0  3.321d0    ! 300K  Vurgaftman1  conduction band edge energies
relative to valence band number 1 (number corr

 absolute-deformation-potentials-cbs   =%ac_AlGaN  -4.95d0  3.81d0
 !absolute-deformation-potentials-cbs   =-6.8d0 -4.95d0  3.81d0     !AlN
 !absolute-deformation-potentials-cbs = -5.22d0  -4.95d0  3.81d0      ! Zunger
 lattice-constants                 = %g_AlGaN %g_AlGaN %g_AlGaN
 lattice-constants-temp-coeff       = 5.59d-6    5.59d-6     5.59d-6   ! [nm/K]

 !lattice-constants                 = 0.4373d0     0.4373d0    0.4373d0 !AlN
 elastic-constants                  = %c11_AlGaN %c12_AlGaN %c44_AlGaN
 !elastic-constants                 = 304d0  152d0  193D0   !elastic-constants ALN        = c11  c12  c44
 valence-band-masses                = %vb_mass1   %vb_mass1   %vb_mass1  %vb_mass2   %vb_mass2   %vb_mass2
%vb_mass3   %vb_mass3   %vb_mass3  !  [m0] ml,mt1,mt2 for each band. Ordering of numbers corresponds to band no.
1, 2, ... (hh, lh, so)
  6x6kp-parameters                 =    -0.480000D+01   -0.198000D+01   -0.510000D+01    ! [hbar^2/2m] [hbar^2/2m]
[hbar^2/2m]
                                %splitt_off!Splitt-off [eV]
 !valence-band-energies             = -1.321d0
  valence-band-energies             = %Valenzband_AlGaN! A. Zunger, average valence band energy E_v,av [eV]
  varshni-parameters                = 0.593d-3 0.593d-3 0.593d-3     ! alpha [eV/K](Gamma, L, X) Vurgaftman1/Vurgaftman2
                              600d0    600d0    600d0       ! beta  [K]   (Gamma, L, X) Vurgaftman1/Vurgaftman2
!absolute-deformation-potential-vb   = 4.94d0                    ! a_v [eV] Zunger
  !absolute-deformation-potential-vb   = 4.9d0                    ! a_v [eV] Vurgaftman2 has different sign convention -> -4.9
  absolute-deformation-potential-vb   = %av_AlGaN ! a_v [eV] Vurgaftman1 has different sign convention -> -3.4
  !absolute-deformation-potentials-cbs = -6.0d0   -4.95d0  3.81d0      ! Vurgaftman1 (Gamma) / Zunger - absolute defor-
mation potentials of conduction band minima a_cd , a_ci's
  !absolute-deformation-potentials-cbs = -4.5d0   -4.95d0  3.81d0      ! Vurgaftman2 (Gamma) / Zunger - absolute defor-
mation potentials of conduction band minima a_cd , a_ci's
! absolute-deformation-potentials-cbs = -5.22d0  -4.95d0  3.81d0      ! Zunger                    - absolute deformation poten-
tials of conduction band minima a_cd , a_ci's
  ! a_c(Gamma) = a_v + a_gap(Gamma) = 4.94 - 10.16 = -5.22           ! [eV] Zunger
  ! a_c(L)     = a_v + a_gap(L)     = 4.94 -  9.89 = -4.95           ! [eV] Zunger
  ! a_c(X)     = a_v + a_gap(X)     = 4.94 -  1.13 = -3.81           ! [eV] Zunger
  !uniax-vb-deformation-potentials     = -1.9d0   -10d0             ! b,d [eV]  Vurgaftman1
 uniax-vb-deformation-potentials     = %uniaxial_AlGaN -5.5d0             ! b,d [eV]  Vurgaftman2
! uniax-cb-deformation-potentials     = 0d0      14.26d0  8.61d0      ! [eV] ? no idea, I took GaAs values, Xi_u(at minimum)
$end_binary-zb-default
!_____
_____
!_____
_____
$binary-zb-default
```

```
binary-type                    =GaN(zb)-zb-default!
 apply-to-material-numbers          =2
 conduction-band-masses             =%mass_eGaN %mass_eGaN %mass_eGaN ! [m0] ml,mt1,mt2 for each band. Order-
ing of numbers corresponds to band no. 1, 2, ... (Gamma, L, X)
                                0.200000D+00    0.200000D+00    0.200000D+00    ! [m0]
                                0.500000D+00    0.300000D+00    0.300000D+00    ! [m0]

 conduction-band-energies           = %GaN_LB 4.870d0  3.800d0                 !  Eigen
 !conduction-band-energies          = 2.579d0  4.870d0  3.800d0     !  0K  Vurgaftman1/Vurgaftman2  conduction band
edge energies relative to valence band number 1 (number corresponds
 !conduction-band-energies          = 2.520d0  4.811d0  3.741d0     ! 300K  Vurgaftman1/Vurgaftman2  conduction band
edge energies relative to valence band number 1 (number corresponds
 absolute-deformation-potentials-cbs = %ac_GaN  -7.46d0  -0.52d0
  lattice-constants                 = %g_GaN %g_GaN %g_GaN ! [nm]  including 'lattice-constants-temp-coeff'
 lattice-constants-temp-coeff       = 5.59d-6    5.59d-6     5.59d-6   ! [nm/K]
http://www.ioffe.ru/SVA/NSM/Semicond/GaN/basic.html
!a_lc = a_lc(300 K) + b * (T - 300K)

 elastic-constants                  = %c11_GaN  %c12_GaN  %c44_GaN
 valence-band-masses                = %mass_hhGaN   %mass_hhGaN   %mass_hhGaN  %mass_lhGaN   %mass_lhGaN
%mass_lhGaN  0.29d0    0.29d0    0.29d0

6x6kp-parameters                    = -6.74d0   -2.18d0   -6.66d0    ! Vurgaftman2  L,M,N   [hbar^2/2m] (--> divide by
hbar^2/2m)
                               0.015d0                  ! Vurgaftman1/Vurgaftman2 delta_(split-off) in [eV]

 valence-band-energies              = %GaN_VB ! A. Zunger, average valence band energy E_v,av [eV]
 varshni-parameters                 = 0.593d-3 0.593d-3 0.593d-3     ! alpha [eV/K](Gamma, L, X) Vurgaftman1/Vurgaftman2
                               600d0    600d0    600d0       ! beta  [K]   (Gamma, L, X) Vurgaftman1/Vurgaftman2

 !absolute-deformation-potential-vb   = 0.69d0                    ! a_v [eV] Zunger
  !absolute-deformation-potential-vb   = 0.69d0                   ! a_v [eV] Vurgaftman2 has different sign convention -> -0.69
  absolute-deformation-potential-vb   = %av_GaN                   ! a_v [eV] Vurgaftman1 has different sign convention -> -5.2

!absolute-deformation-potentials-cbs = -2.2d0   -7.46d0  -0.52d0     ! Vurgaftman1 (Gamma) / Zunger - absolute defor-
mation potentials of conduction band minima a_cd , a_ci's
  !absolute-deformation-potentials-cbs = -6.71d0  -7.46d0  -0.52d0     ! Vurgaftman2 (Gamma) / Zunger - absolute defor-
mation potentials of conduction band minima a_cd , a_ci's
! absolute-deformation-potentials-cbs = -6.68d0  -7.46d0  -0.52d0     ! Zunger                    - absolute deformation poten-
tials of conduction band minima a_cd , a_ci's
  ! a_c(Gamma) = a_v + a_gap(Gamma) = 0.69 - 7.37 = -6.68             ! [eV] Zunger
  ! a_c(L)     = a_v + a_gap(L)     = 0.69 - 8.15 = -7.46             ! [eV] Zunger
  ! a_c(X)     = a_v + a_gap(X)     = 0.69 - 1.21 = -0.52             ! [eV] Zunger
  !uniax-vb-deformation-potentials    = -2.2d0   -3.4d0              ! b,d [eV]  Vurgaftman1
 uniax-vb-deformation-potentials    = %uniaxial_GaN   -3.7d0             ! b,d [eV]  Vurgaftman2
 !uniax-cb-deformation-potentials   = 0d0      14.26d0    8.61d0      ! [eV] ? no idea, I took GaAs values, Xi_u(at minimum)
$end_binary-zb-default
!_____________________________________________________________________________________

!****** OUTPUT ***************************************************************!
$global-settings                                        !
output-directory          = output/
!output-directory          = ./               ! This setting is currently needed for nextnanomat. Will be obsolet in the future.
 !debug-level              = 0
 number-of-parallel-threads = 4                                 ! 1 = for single-core CPU
$end_global-settings                                     !
$output-raw-data                                        !
 destination-directory              = raw_data1/
 potential                          = yes                       !
 fermi-levels                        = yes                       !
```

```
 strain                          = yes                       !
 kp-eigenstates                    = no                        !
$end_output-raw-data                                          !
$output-1-band-schroedinger                                   !
!Note: We apply an overall band-shift to all bands in order to align the topmost valence bands (heavy hole/light hole) to
zero (0 eV).
 !-----------------------------------------------
 ! Shift all bands, so that GaAs (hh/lh) = 0 eV.
 !-----------------------------------------------
 destination-directory           = Schroedinger_1band/
 !band-shift = 2,5401! [eV]                 !
 shift-wavefunction-by-eigenvalue  = yes
 sg-structure                    = yes                       ! ??
 conduction-band-numbers           = 1                         ! only gamma point (as specified above)
 cb-min-ev                       = 1                       !
 cb-max-ev                        = 4                        ! four eigenvalues per band (as specified above)
 valence-band-numbers            = 1 2 3                     ! heavy hole, light hole and split-off hole (as specified above)
 vb-min-ev                       = 1                       !
 vb-max-ev                        = 4                        ! four eigenvalues per band (as specified above)
 complex-wave-functions            = no                        !
 scale                         = 2d0                      ! for psi_squared, no physical relevance
 interband-matrix-elements         = yes
 intraband-matrix-elements         = yes                       ! electron-hole transition energies and wave function overlaps
$end_output-1-band-schroedinger                               !
$output-bandstructure                                       ! output for the band structure and the potential
 destination-directory           = band_structure/           !
 conduction-band-numbers           = 1                       ! conduction band edge at gamma point=1,L=2,X=3
 valence-band-numbers            = 1 2 3                     ! valence band edge for heavy, light and split-off holes
 potential                     = yes                     !
$end_output-bandstructure                                     !
!***** END BAND STRUCTURE AND DENSITIES ************************************!
!***** OUTPUT STRAIN ********************************************************!
! This is the output for the densities.                       !
$output-densities                                           !
 destination-directory           = densities1/               !
 electrons                      = yes                     !
 holes                         = no                    !
 charge-density                    = no
 intrinsic-density                = yes                     !
 ionized-dopant-density              = yes                     !
 piezo-electricity                = yes                     !
 pyro-electricity                 = no                    !
 interface-density                 = yes
 effective-density-of-states-Nc-Nv      = yes
 subband-density                  = yes                                   !
$end_output-densities                                       !

!Biaxial strain (in plane of interface)  e_xx = e_yy = ( a_substrate - a_layer ) / a_layer = 0.0155   (1.55 % lattice mismatch)
!Uniaxial strain (perpendicular to interface)      ezz = - 2 (c12/c11) exx = - 0.014

$output-strain      ! This is the output for the strain.
 destination-directory           = strain1/                !
 strain                         = yes                     !
 strain-simulation-system           = yes                     !
$end_output-strain                                          !

!***** END OUTPUT STRAIN ***************************************************!
$output-current-data                                        !
 destination-directory           = current1/
 current                        = no                      !
 fermi-levels                     = yes                     !
```

```
 mobility-out                  = yes                    !
 IV-curve-out                   = no
 recombination                   = no
$end_output-current-data                                  !

$output-material                                          !
 destination-directory          = material/
 doping-concentration            = doping_concentration1D.dat
$end_output-material                                      !
```

7.8 Matlab Source Code

This is the Matlab source code used for the simulation of the FWHM of the IR absorption.

```
%clc
clearvars

F0011 = -0.5;
F01 = 0.3;
Ef = 0.52;
E10 = 0.82;
rough = 0.45;

m1 = 0.19;
m2 = m1*9.109*10^-31;
hbar = 1.05457*10^-34;
hbar2 = 6.58212*10^-16;
e = 1.602*10^-19;

start1 = 0.1;
ende1 = 0.9;
schritt = 0.1;
range = (ende1-start1)/schritt;
data(uint8(range),2)= 0;
l = 1;

for i=start1:schritt:ende1
   format long
   corr = i*10^-9;
   eq = m2.*e.*(corr.^2)./(hbar.^2);
   eq0 = @(E,t) eq.*E.*(1-cos(t));
   eq1 = @(E,t) exp(-eq0(E,t));
   G1 = m2.*corr.^2.*rough.^2./(hbar2.^2.*e);
   GIntra = @(E)G1.*F0011.^2.*integral(@(t)eq1(E,t),0, pi);

   eq2 = @(E,t) eq.*(E+E10./2-sqrt(E.*(E+E10)).*cos(t));
   eq3 = @(E,t) exp(-eq2(E,t));
   GInter = @(E)G1.*F01.^2.*integral(@(t)eq3(E,t),0, pi);
   GOpt = @(E) (GIntra(E)+GInter(E));
   Fermi = @(E)(1./(exp((E-Ef)./0.025)+1));

   Resigma = @(x, E10) integral(@(E) Fermi(E).*GOpt(E)./((x-E10).^2+GOpt(E).^2),0,1,'ArrayValued',true);
   start = E10-5;
   ende = E10+5;
   g = fplot(@(x) Resigma(x, E10), [start ende], 'MeshDensity', 50);
   %grid on

   x = g.XData;
   y= g.YData;
   maxy = max(y);
   f = find(y==maxy);
   cp = x(f);% ignore Matlabs suggestion to fix!!!
   y1= y./maxy;
   ydatawr(:,1) = y1;
   ydatawr(:,2) = x;
   newFit1=find(x>= cp);
   newFit2=find(x < cp);
```

```
    ydatawr2 = ydatawr(min(newFit1):max(newFit1),:);
    ydatawr3 = ydatawr(min(newFit2):max(newFit2),:);
    sp1 = spline(ydatawr2(:,1),ydatawr2(:,2),0.5);
    sp2 = spline(ydatawr3(:,1),ydatawr3(:,2),0.5);
    Fullw = (sp1-sp2)*1000;
    data(l,1) = i;
    data(l,2) = Fullw;
    i;
    l=l+1;
    clearvars -except data l m1 m2 hbar hbar2 rough e Ef E10 F0011 F01
end
format short
data
```

7.9 Acknowledgements

Zuletzt möchte ich mich bei allen bedanken, die mir bei meiner Masterarbeit geholfen haben. Als erstes gilt mein Dank apl. Prof. Dr. Donat As, der mir diese Arbeit angeboten und mir mit hilfreichen Vorschlägen zur Seite gestanden hat. Ich danke auch Prof. Dr. Dirk Reuter der mich mit vielen Anregungen und Diskussionen unterstützt hat.

Außerdem danke ich Prof. Dr. Cedrik Meier für die Übernahme des Gutachtens meiner Arbeit. Als letztes möchte ich noch den übrigen Mitgliedern meiner Arbeitsgruppe für ihre Unterstützung und Motivation danken.

7.10 Eidesstattliche Erklärung

Hiermit versichere ich, dass ich die vorliegende Arbeit selbständig verfasst und keine anderen Quellen und Hilfsmittel als die angegeben benutzt habe.

Paderborn, 15.09.2017

_____

Tobias Wecker